

Application of Electrical Impedance Tomography to Robotic Tactile Sensing

by

Ahmed Elsanadedy

A Thesis submitted to The Faculty of Graduate Studies and
Research in partial fulfillment of the degree requirements of

Master of Applied Science

in

Mechanical Engineering

Carleton University

Ottawa, Ontario, Canada

July 2012

© 2012

Ahmed Elsanadedy

Abstract

Tactile sensors for artificial skin applications, based on sensing arrays, suffer from fragility, complex fabrication techniques and stiff characteristics. These critical limitations hinder their integration for artificial skin purposes. Eliminating the presence of wires within the active sensing area leads to improved robustness and reduced wiring. Electrical Impedance Tomography (EIT) was investigated for use as a pressure sensor with electrodes limited only to the boundary of the active sensor area for enhanced artificial skin implementation. A one-step regularized solver using the Difference Imaging method was used for pressure measurement and profile depiction. Firstly, EIT sensor applicability is tested through static planar compression experiments of a conductive polymer as well as woven and non-woven conductive fabric via a stacked contact resistance transducer approach. Corresponding 2D FEM's with complete electrode boundary conditions for solving the EIT problem are developed in Electrical Impedance and Diffuse Optical Reconstruction software and the system configuration is highlighted. Secondly, covering a non-planar complex geometric part using a single stretchable element was achieved using a stretchable woven fabric and a novel surface meshed EIT model to more effectively solve the image reconstruction problem. The method is simulated and validated via experimental trials where multi-touch capability for up to 3 points of contact is achieved under constant stretch. Furthermore, objective quantification of the effect electrode proximity has on stimulated regions is demonstrated through several performance metrics. Reduced position accuracy was found to be mainly attributed to the presence of image artifacts and increased shape deformations were found with close proximity to electrodes. Following system benchmarking, this study found the highest hysteresis value attributed to the conductive polymer sample at 34.5% and woven fabric displaying poor repeatability for pressure measurement but demonstrating potential as a touch sensor. It is recommended that the non-woven conductive fabric be used for pressure sensing applications with a demonstrated range of 65 kPa. Pressure profile tests showed complex shape recognition competence where edges and gaps are displayed with reduced blurring.

Acknowledgements

To my parents, for their never ending support and encouragement.

I wish to express my sincere gratitude to my thesis supervisors Professor Mojtaba Ahmadi and Professor Andy Adler for their ideas, guidance and assistance. I would also like to thank Dr. Mamatjan for his patience and advice and the ABL team, for their spirited good company and friendship. Finally, words are inadequate for offering my gratitude to Mostafa Omar, for his life lessons and for always being there throughout the course of this work.

Table of Contents

Abstract.....	2
Acknowledgements	3
Table of Contents	4
List of Tables	8
List of Figures.....	9
Nomenclature	14
Chapter 1 Introduction.....	1
1.1 Thesis Objectives.....	3
1.2 Thesis Contributions.....	3
1.3 Thesis Overview.....	5
Chapter 2 Literature Review	7
2.1 Tactile Sensing Solutions	8
2.1.1 Piezoresistive Tactile Sensors	11
2.1.2 Capacitive Tactile Sensing	15
2.1.3 Piezoelectric Sensing	16
2.1.4 Optical.....	16
2.2 Electrical Impedance Tomography.....	19
2.2.1 Mathematical Setting	20

2.2.2	Forward Problem.....	22
2.2.3	Reconstruction.....	25
2.2.4	EIT Data Collection and Instrumentation	27
Chapter 3 Experimental Setup, Methodology and Preliminary Results		30
3.1	Transduction Method.....	31
3.2	Contact Resistance Material Characterization.....	33
3.2.1	Method	34
3.2.2	Results	36
3.2.3	Discussion	38
3.3	Fixture Design	40
3.4	Raw Data Acquisition.....	42
3.5	Reconstruction.....	44
3.5.1	Inverse Solver.....	45
3.6	Performance Evaluation Parameters.....	47
Chapter 4 Pressure Distribution Sensor		51
4.1	EIT System Performance Evaluation	51
4.1.1	Method	52
4.1.2	Results	55
4.1.3	Discussion	60

4.2	Sensor Performance Evaluation.....	62
4.2.1	Method	62
4.2.2	Results	64
4.2.3	Discussion and Summary	71
Chapter 5	Stretchable EIT based Tactile Sensor	75
5.1	Surface Modeling and Linear Interpolator Derivation for Direct FEM Formulation ...	76
5.2	Simulated Pressure Distribution	80
5.3	Stretchable EIT Sensor Development.....	84
5.3.1	Stretchable Transducer	84
5.3.2	Apparatus	86
5.3.3	Procedure and Configuration	87
5.4	Results	90
5.4.1	Planar Case: Static Loading Experiment.....	90
5.4.2	Planar Case: Feature Recognition Experiment.....	93
5.4.3	Planar Case: Point Contact Tracking Experiment	94
5.4.4	Complex Geometric Surface Case Experiment.....	95
5.5	Discussion	99
5.5.1	Pressure Sensing Limitation.....	99
5.5.2	Touch Sensing Capability	100

5.5.3	Complex Geometric Surface Coverage.....	100
Chapter 6	Conclusions and Future Work.....	102
6.1	Conclusion.....	102
6.2	Recommendations and Future Works.....	104
Appendix.....	106
Bibliography	116

List of Tables

Table 3.1: Stacked material samples as transducer elements.	32
Table 3.2: Transducer element characteristics.....	38
Table 3.3: Electrodes used with fixture.	42
Table 3.4: SigmaTom II configuration parameters.....	44
Table 4.1: EIT configurable parameter settings.....	63
Table 4.2: Sample characteristic based on static loading trials.	66
Table 5.1: Materials tested with SMP bus material	85
Table 5.2: Sample #3 properties	86
Table 5.3: Sensor characterization parameters.	93
Table 5.4: Position Error for woven fabric on planar surface at 4 different locations.	95
Table 5.5: EIT system parameters for stretchable fabric.	97
Table 6.1: Summary of planar pressure sensor static assessment results.	104

List of Figures

Figure 2.1: 3-axis protrusion based force sensor design via conductive rubber (a) Sensor taxel with 4 cells and typical impact at tip of hemisphere shaped protrusion, (b) Side view x -direction with force decomposition, (c) Side view y -direction and (d) Top view of taxels with inner circles representing electrode contacts [14].	10
Figure 2.2:(a) Micro-machined strain gauges on silicon substrate on Kevlar [6], (b) PDMS encapsulated strain gauge array [8], (c-f) Tri-axial prototype using beam and cantilever design [9]......	12
Figure 2.3: (a) Array of conductive elastomer [15], (b) Integral temperature detection [11], (c-d) Coplanar and opposite electrode mount [10], (e) Stitched wire on conductive polymer [12]......	14
Figure 2.4: Array based tactile sensor on flexible substrate [35]	17
Figure 2.5: FEM resistor network [53].	22
Figure 2.6: Local to global admittance matrix assembly example [53].....	24
Figure 2.7: Overview of EIT hardware architecture.	28
Figure 2.8: Adjacent drive pattern and the sequence of consecutive voltage measurements	29

Figure 3.1: (a) Sample#1 demonstrating high pliability,(b) Stacked Sample #2 attached using electrodes.....	33
Figure 3.2: Schematic of DAQ circuit used for resistance measurement.	34
Figure 3.3: (a) Sample #1 measuring 5x5 cm, placed on copper electrodes with a 3 cm gap.(b) Sample #2 with same dimensions and pierced electrodes mounted with a 3 cm gap inbetween.	35
Figure 3.4: Loading apparatus for contact resistance investigation.....	36
Figure 3.5: Sample#1 Hysteresis curve.	37
Figure 3.6: Sample#2 Hysteresis curve.	38
Figure 3.7: Creasing in Sample #2.....	40
Figure 3.8: Fixture for Sample #1.....	41
Figure 3.9: EIT instrumentation.....	43
Figure 3.10: FEM discretization of the domain with 4078 elements and 2075 nodes with electrode placement.	45
Figure 3.11: Procedure for EIT analysis.....	47
Figure 4.1: Nonconductive cube placed in Saline solution, in semi-enclosed container..	53
Figure 4.2: (a) Displaced saline volume by varying insulator depth. (b) Changing insulator cube volume.	54

Figure 4.3: (a) left to right, images for volume of displaced saline (b) Associated change in conductivity for 3 different volumes (c) Relative change in raw voltage data.	56
Figure 4.4: (a) left to right, images for volume of displaced saline by changing cube depth (b) Associated change in conductivity for 3 different volumes (c) Relative change in raw voltage data.	57
Figure 4.5: Sensor images for different (x,y) cube CoG positions in cm.	58
Figure 4.6: Position Error (PE), Resolution (Res) and Ringing (RNG) for different CoG positions in regard to boundary electrodes.	59
Figure 4.7: Drift in fractional change in voltage for three trials.	60
Figure 4.8: (a) Sample #1 sensor calibration and hysteresis curve (b) Top, Sensor image for variable loading with fixated contact location (b) Middle and bottom, the variations of the CoP in the x and y directions for constant location at the centre of the phantom and under variable normal load.	64
Figure 4.9: (a) Sample #2 sensor calibration and hysteresis curve (b) Top, Sensor image for variable loading with fixated contact location (b) Middle and bottom, the variations of the CoP in the x and y directions for constant location at the centre of the phantom and under variable normal load.	65
Figure 4.10: Sample #1 in fixture with connected electrodes.	66
Figure 4.11: Position 1 to 15: from left to right, top to bottom (cm). Applied pressure at the specified location depicted on the left with square shaped contact scaled to size and the actual corresponding sensor image to the right for Sample #1.	67

Figure 4.12: Performance metrics established for Sample #1.	68
Figure 4.13: Sample #2 with both layers of non-woven fabric in stacked arrangement with circular pierced button electrodes mounted at the boundary.	69
Figure 4.14: Pressure map for 15 stimulated locations conducted on Sample #2 where red regions depict positive increase in conductivity change and blue regions show a negative conductivity change	70
Figure 4.15: Performance metrics conducted on Sample #2.	71
Figure 5.1: Projecting element from 3D to 2D space while preserving dimensions.	78
Figure 5.2: Mesh composed of 624 elements and 337 nodes used for complex geomtry modelling with point electrodes equidistantly placed along the boundary.....	81
Figure 5.3: (Top) Stimulated elements, (Bottom) Reconstructed images where red regions depict an increase in conductivity corresponding to pressure.	83
Figure 5.4. Two point and three point contact using surface mesh (top view) where red regions depict positive changes in conductivity.	84
Figure 5.5: (left) Sample 3 on a planar surface, (right) stretched over hemisphere shaped part matching the mesh found in the forward model.	87
Figure 5.6: Forward model mesh composed of 2304 elements and 1201nodes with electrode nodes highlighted in green for stretchable EIT sensor planar case.	89
Figure 5.7: Hysteresis curve based on 25% ROI (left) and corresponding raw data (right) for single layer of conductive fabric.	91

Figure 5.8: Hysteresis curve based on 25% ROI threshold (left) and corresponding raw data (right) for dual layer stacked setup of conductive fabric. 92

Figure 5.9: (a) Actual pressed shapes (b) Pressure profile for single layer and (b) dual layer setup for two different shapes in (mS/sq). 94

Figure 5.10: Single point contact with sensor stretched over hemisphere shaped part with red regions depicting positive increase in admittance 96

Figure 5.11: (a) Actual two and three point contact admittance change with sensor stretched over hemisphere (b) Reconstructed images using surface model in (mS/sq) (c) Reconstructed images using 2D planar model in (mS/sq)..... 98

Nomenclature

ABS	Acrylonitrile butadiene styrene
CCD	Charge Coupled Device
CoG	Centre of Gravity
CoP	Centre of Pressure
EIDORS	Electrical Impedance Tomography and Diffuse Optical Reconstruction Software
EIT	Electrical Impedance Tomography
FET	Field Effect Transistor
LCR	Inductive Capacitance Resistance meter
MEMS	MicroElectroMechanical Systems
NOSER	Newton's One Step Error Reconstruction
PDMS	Polydimethylsiloxane
PE	Position Error
POF	Plastic Optical Fiber
PSCR	Pressure Sensitive Conductive Rubber
PVDF	Polyvinylidene Difluoride
PZT	Lead Zirconate Titanate
RES	Resolution
STL	STereoLithography
VCCS	Voltage Controlled Current Source

Chapter 1

Introduction

The ever evolving field of robotics has seen rapid growth over recent years. With an environment that is leaping with technological advancements robots must adapt to their surroundings as do we in a more connected and demanding world. With automated robotic tasks proving successful in a variety of industrial sectors, the reliance on their contribution has propelled advancements and overcome limitations that as humans we are not physically capable of. Despite their widespread integration in the manufacturing and industrial sector, their presence has been confined to specific working envelopes. Strict safety standards are dictated in terms of their operation, and the associated presence of people around them, where only trained professionals are expected to control and run them. Thus the concept of a true anthropomorphic robot that is capable of detecting and safely responding to its environment without being contained and isolated is the aim of much of the robotic research today.

The complex problem of humanoid robotics can be engaged by dissecting this feat into four main categories; (1) Detection (2) Control (3) Actuation and (4) Mechanical platform design, of which we are only interested in the first. Detection which is attributed to the five senses of touch, smell, hearing, taste and vision has a considerable array of sensing solutions currently available for each category. Focusing on the sense of touch or pressure detection, leads to the concept of an artificial pressure sensitive skin. By having a skin like sensing ability that is capable of distinguishing multi-touch stimuli

in addition to detecting the magnitude of the pressure will allow for more sophisticated human-robotic interactions.

Tactile sensor technology based on resistive elements which include: micro-machined strain gauges, conductive elastomers, conductive polymers and conductive fluids are common solutions applied to humanoids today. Capacitive sensors as well as optical sensors are also very effective alternatives. Despite the large variety of sensors that are currently available, their adoption in the field of humanoid robotics is restricted by their stiff nature and minimal stretch ability caused by the physical structure of the sensor. This limitation is typically caused by the presence of a wire mesh in the contact area of the sensor and the complex construction of the sensing element.

Electrical Impedance Tomography (EIT) was initially introduced as a medical imaging technique that can detect the conductivity distribution within a body by having electrodes confined to the boundary of the conductive mediums surface. As such, numerous industrial applications ranging from image reconstruction of gas/solid fluid flow within piping to geophysics [1] have adopted this technology. Therefore, by implementing this technology in the field of pressure detection we eliminate the need for a matrix of sensing cells and an array of electrodes that need to withstand pressure from within the sensing area. Hence, EIT-based pressure sensing has the potential to cover complex geometries such as joints in addition to ground reaction force measurement for foot sensing providing a more complete pressure sensing solution.

In this thesis, pressure detection using EIT was investigated. The challenge of implementing an EIT pressure sensing solution was in the selection of the materials for

the sensing medium, configuring the hardware platform used for raw data acquisition and the model used for image reconstruction. Moreover, it was necessary to systematically establish a means to quantify the sensors image output and characterize its ability to depict the pressure profile.

1.1 Thesis Objectives

The overall aim of this thesis is to assess the accuracy and reliability of two-dimensional EIT for pressure sensing applications. This overall aim is subdivided into the following specific objectives:

- Develop a functional EIT model and experimental platform for identifying compatible materials which are suitable for pressure and touch sensing applications.
- Experimentally validate the approach used using different piezoresistive media suitable for integration on robotic platforms and to perform EIT system benchmarking. Calibrate, characterize, and analyze the image-based output of the sensor using typical sensor performance metrics.
- Verify multi-touch capabilities and to test true pressure profile depiction.
- Develop an alternative or modified EIT approach specifically designed for the application of pressure and touch sensing.

1.2 Thesis Contributions

The research contributions of this thesis are as follows:

- Effective 2D EIT Distributed Pressure Sensing: Implementation of a SigmaTom II EIT pressure sensor based on a single step solver using a difference imaging reconstruction method was achieved.
- EIT System Benchmarking: The EIT algorithm based on the difference imaging approach was tested using a reference setup involving an optimal homogenous medium (saline solution) and electrode contact. Image quality dependence on stimulated areas proximity to electrodes was also identified based on experimental trials.
- Material Testing: Conductive polymer and both woven and non-woven conductive fabrics were tested for use as a contact resistance based transduction method for integration in the EIT sensor platform. A fixture was also designed for implementing press fit electrodes on any type of sample. Pressure sensitive conductive rubber sample was verified to be sensitive only based on contact resistance theory. Pressure sensing was achieved using both the conductive polymer and non-woven fabric while woven fabric proved effective only as a touch sensor. It was identified that high hysteresis is the main bottleneck in sensor performance
- EIT Complex Geometry Surface Model: Development of a novel EIT forward model based on a surface mesh that corresponds to a complex geometric feature over which stretchable transducer elements can be implemented. The simulation of the integrated model was successfully verified and experimentally validated using a hemispherical shape, through a stretched woven fabric sensing medium.

- Feature Recognition and Multi-touch: EIT setup and parameter selection that allow for complex feature recognition capabilities are achieved where different shapes were reconstructed, demonstrating the EIT tactile pressure sensors capability of reconstructing a true pressure profile. Multi-touch, up to 3 points of contact, was verified using a stretched woven fabric. The novel surface-based forward model was experimentally validated over a hemisphere-shaped part as a demonstration of complex geometry base case.
- Publications and EIDOR's Integration: The conductive polymer based EIT pressure sensor results were published in the *ASET 2012 International Conference on Electrical and Computer Systems, Ottawa, Ontario, Canada* [2] . The source code used in this thesis will be integrated in the following release of the Electrical Impedance and Diffuse Optical Reconstruction Software (EIDORS) [3] version under the GNU General Public license.

1.3 Thesis Overview

The rest of this thesis is organized in the following manner:

Chapter 2: A brief overview of related literature on tactile sensing prototypes for artificial skin applications classified based on their transducer type is presented. This is followed by a background section on EIT which introduces the forward and reconstruction problem as well as the current state of this technology in the pressure sensing theme.

Chapter 3: A through explanation of the overall experimental methodology is presented. This involves the EIT hardware system, data acquisition, fixture design and the transduction method approach used. Preliminary results for sample selection are also

included. Furthermore, EIT difference imaging used for image reconstruction and the pressure calculation method is introduced.

Chapter 4: The methodology introduced is evaluated using a saline water setup to perform EIT system evaluation and to demonstrate whether the algorithm introduces any undesirable effects on pressure calculation that contradict the raw data. The conductive polymer and non-woven flexible fabrics are tested and characterized for used as pressure sensors.

Chapter 5: The derivation for the modified linear interpolator function used for Direct Finite Element Model (FEM) to allow for surface modeling in the EIT reconstruction process is introduced. The novel EIT approach is then simulated. A stretchable woven fabric is experimentally tested for EIT sensing capabilities in a planar case and complex geometric feature case. The setup is then used to validate the feasibility of the novel surface modeling approach and a visual comparison between outputs of a planar 2D model and the surface model is demonstrated.

Chapter 6: A conclusion of the aforementioned experiments is presented. Design bottlenecks are highlighted and key finds are summarized. In addition, several possible directions for further EIT sensor improvements are mentioned under the future work section.

Chapter 2

Literature Review

The general design requirements for robotic tactile sensors are mostly based on mimicking the human skin which gives an outline of the fundamental goals that need to be met. Section 2.1 will be on the current state of the art developments of such extrinsic tactile sensor for both uni-axial and tri-axial loads, and the main challenges in their design. The discussion then focuses on the motivation as to why EIT can positively contribute to this field and a survey of EIT based pressure sensing developments is covered starting from the original concepts to current achievements. A brief overview of the mathematical setting and the practical means of EIT's execution, aimed specifically for this thesis, are then presented in section 2.2.

As the pursuit of more intelligent robotic platforms continues, the need for more sophisticated tactile solutions that will aid in the perception of a changing environment has become vital. Classified as extrinsic sensors, [4] they only contribute to the overall cognitive capabilities of the humanoid which lead to an interpretation of the surroundings. This is opposed to providing information on other proprioceptive-based functions relating to the physical parts of the robots provided by instruments such as encoders and torque sensors. Tactile extrinsic sensors are further subdivided as distributed pressure sensors that are either high or low density based on their spatial resolution performance [4]. Section 2.1 covers the most current prototypes developed specifically for use on autonomous robots.

2.1 Tactile Sensing Solutions

Typically, tactile sensing solutions are based on a matrix of sensing cells or taxels corresponding to a particular transduction method. According to recent comprehensive reviews [4],[5], as well as recent wearable sensing fabric developments in [6], two major requirements are flexibility and enhanced stretch capabilities. Flexible tactile sensors are currently available based on different transduction methods but stretch capability is far less common. Other requirements include:

- minimal wiring;
- low cost and well established fabrication techniques;
- thermal management and temperature detection;
- simple mounting or adhesion mechanism.

The reduction in wiring complexity is of major importance in the robotics field and needs to be integrated in the design. Not only will increased wiring limit the scalability of distributed tactile sensors but it may also negatively impact the dexterity of a robotic platform. Low cost is also necessary due to the integration of these sensors over large areas such as the torso of autonomous robotic platforms. In addition, the incorporation of tactile sensors that allow for thermal management or breathability, on parts under which electronic components generate heat, could benefit overall system cooling. Simple mounting and easy removal will allow larger areas to be accessible such that enclosed parts or electronics can be replaced via more efficient and simpler maintenance procedures. Moreover, UV protection as described in [7] can be a factor in improved lifecycle performance.

The ability to detect shear as well as normal forces is of great importance for grippers, foot soles as well as the rest of the bipedal or humanoid surfaces. Tactile sensors are not known for their shear measurement capability, a field dominated by 6 Degree Of Freedom (DOF) force sensors. Commercially available 6 DOF force sensors have been integrated particularly in the foot and ankle area for robots such as the Wabian 2 [8][9], Lola [10] and Johnnie [11]. However, their limitations lie in their size and weight which may physically impede interactions. Their common application, effective ground reaction force measurement, is questionable due to their impact on the actual gait hence their lack of integration in modern actuated prosthetic prototypes [12],[13] where cost is an added deterrent. Despite their superior force and moment measurement performance they cannot provide point of contact detection. Adding a multitude of these sensors in an array like form to cover large areas is not economical due to their high cost. Therefore, such flexure and strain gauge designs with onboard electronics are not the optimal choice for versatile, compact humanoid platforms with a need for artificial skin integration.

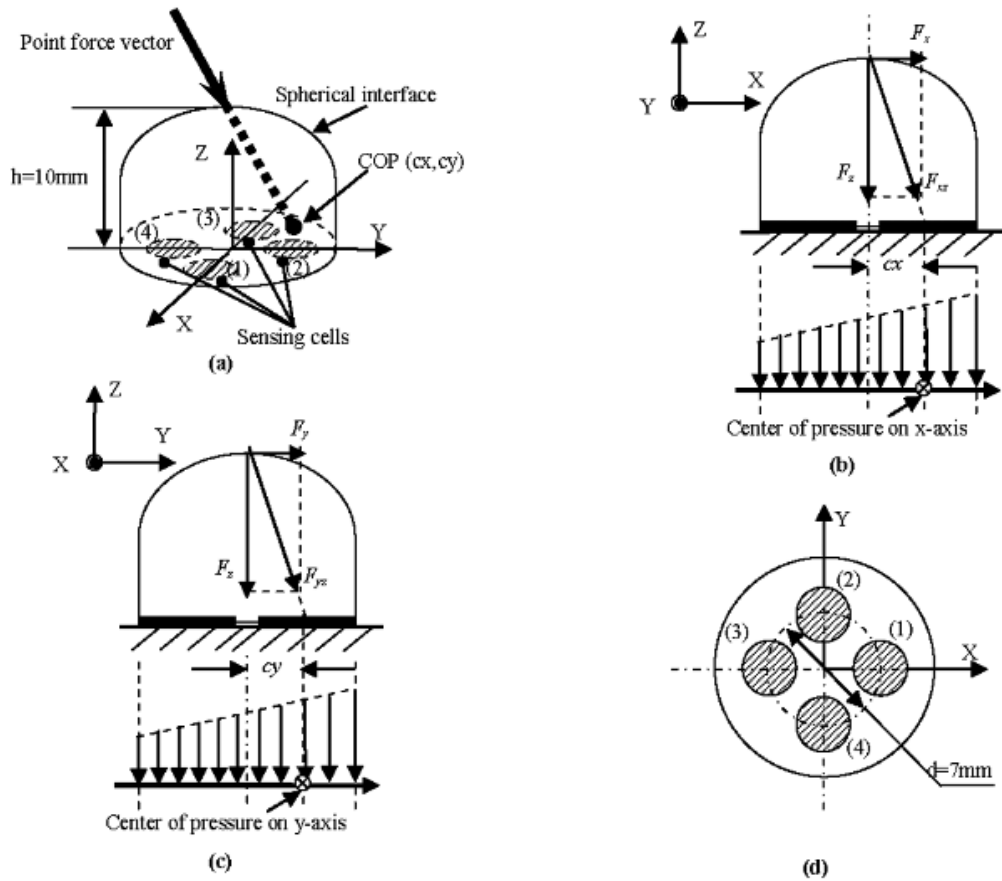


Figure 2.1: 3-axis protrusion based force sensor design via conductive rubber (a) Sensor taxel with 4 cells and typical impact at tip of hemisphere shaped protrusion, (b) Side view x -direction with force decomposition, (c) Side view y -direction and (d) Top view of taxels with inner circles representing electrode contacts [14].

The ability to detect tri-axial forces using a compliant structure has proved to be a challenging task. There have been several prototypes mostly using conductive polymer or so called Pressure Sensitive Conductive Rubber (PSCR) found in [14][15][16] as well as capacitive-based [17]. The main design concept is to have a protruding element as the contact point such as the one shown in Figure 2.1., that usually covers a segmented electrode base. This allows for measuring resistance or capacitive changes to capture

shifts in the Centre of Pressure (CoP) for shear force measurement as demonstrated in Figure 2.1(a). Such designs introduce significant compliance in tactile sensing and sacrifice sensor performance mainly due to reduced hysteresis and accuracy. However, studies for optimal grasping ability [18] show that based on measures of conformability and strain energy dissipation, increased compliance improved traction in robotic grippers. Therefore a balance must be struck between functionality and tactile pressure sensing integration.

There is a wide variety of recent developments in the tactile field sensing aimed at robotic applications. They are presented according to their transducer type in the following sections.

2.1.1 Piezoresistive Tactile Sensors

Micro-machined strain gauges based on arrays of silicon etched islands with metal wire interconnects mounted on a flexible printed circuit board and encapsulated in a polymer are presented in [19]. The lightweight design which is then stitched on textiles allows for enhanced flexibility but suffers from metal wire failure when overloaded Figure 2.2(a). A similar design for a shear stress sensor using on-chip signal conditioning via a Micro Electro Mechanical System (MEMS) approach is achieved in [20]. The sensor is embedded in Parylene due to its compatible bonding temperature and to improve its flexibility. A micro-cantilever design with no diaphragm structure encapsulated in Polydimethylsiloxane (PDMS) is established in [17] where the polymer is an integral part of the design and is not considered an impediment to sensor performance. Four strain gauges are found per cell to allow for tri-axial force measurement. It is also claimed that

20N load can be measured for a 1 cm² cell with significant robustness for ground reaction force measurement in robotic foot sole (Figure 2.2(b)). An alternative cantilever and beam design for tri-axial tactile sensing measurement is implemented in [21] that achieves good linear characteristics, where the sensor is depicted in Figure 2.2(c). Overall, the sensing approach involving encapsulation of MEMS in a polymer suffers from high fragility and high cost, but benefit from well established fabrication techniques.

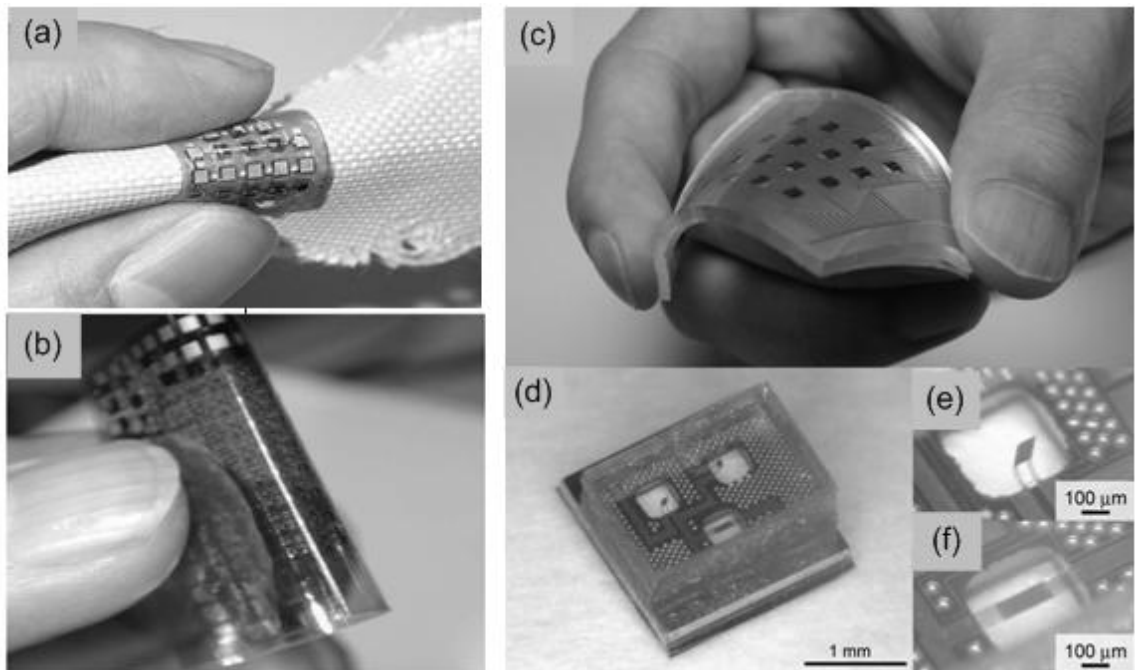


Figure 2.2: (a) Micro-machined strain gauges on silicon substrate on Kevlar [6], (b) PDMS encapsulated strain gauge array [8], (c-f) Tri-axial prototype using beam and cantilever design [9].

Conductive polymers and Conductive fabrics have flexible and stretchable qualities as well as significant robustness to overloading. Their chemical inertness adds to their applicability towards tactile sensing. The working principle is highlighted in [22]

demonstrating that such pre-polymers filled with conductive filler are not really pressure sensitive. The contact resistance change exhibited in a co-planar configuration or with electrodes on both sides of the element, as shown in Figure 2.3 (b,e), is caused by increasing the contact area between the polymer and the electrode. It has also been demonstrated that the 50 phr carbon black filled polymers exhibited superior compression performance and high conductivity where the excitation frequency was found to affect conductance and capacitance through LCR meter experiments as validated by Thongruang *et al* [23]. In [24] , an 8 x 8 array of taxels is fabricated with individual conductive polymers dispensed directly on copper film electrodes with integral temperature detection. The design achieves reduced cross talk as opposed to more common methods with a single conductive sheet with an array of electrodes. Alternative approaches include stitching wires on conductive polymer sheets for simplified fabrication [25] (Figure 2.3(c)). The ability to use conductive stretchable fabric manufactured by coating or screen printing conductive polymers on them is investigated in [26], [27] following the same contact resistance analogy. The two major drawbacks of these sensors are significant hysteresis and the presence of creep.

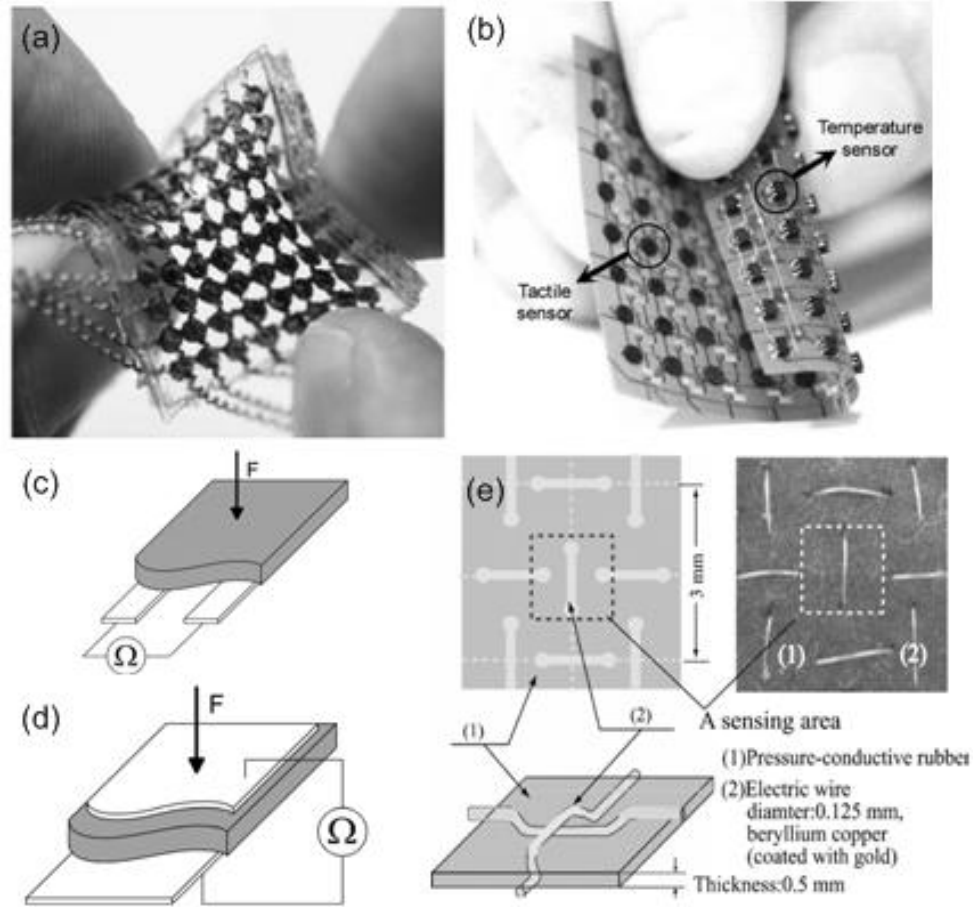


Figure 2.3: (a) Array of conductive elastomer [15], (b) Integral temperature detection [11], (c-d) Coplanar and opposite electrode mount [10], (e) Stitched wire on conductive polymer [12].

Conductive elastomeric composites impregnated with conductive filler are characterized with piezoresistive properties. The volume percentage of the filler and the material stiffness dictate sensor output. Achieving improved robustness via cyclical copper wire as electrodes wound on nylon wires is demonstrated in [15] with a range of up to 600kPa (Figure 2.3(a)). These materials are durable as well as capable of withstanding repeated stretch; however, as with conductive polymers, the hysteresis is a limiting factor in their performance. Quantum tunneling composites have been reported

in [16] where the material can change from a complete insulator to a conductor with resistance based on the amount of deformation. Here, the impregnated metal particles never touch and quantum tunneling is experienced. This technology, investigated in [17], is currently patented by Peratech.

2.1.2 Capacitive Tactile Sensing

Capacitive tactile sensors are considered one of the most sensitive in the field. They seem to exhibit no direct temperature dependence and are available commercially. Several designs have emerged specifically for the robotic skin application. A capacitive sensor on flexible substrate manufactured using flexible circuit and photolithography is presented in [28]. The sensor composed of gold plates and Parylene dielectric layer is characterized with an impressive range of up to 700 kPa with a linear response exhibited from 0.02 to 0.04 pF. It is also highlighted that the main obstacle with this design is with trace breakage when flexed. A more robust setup is demonstrated in [29] where triangular units encompassing 12 capacitive taxels are mounted in a scalable honeycomb arrangement. Silicon rubber foam is used as a dielectric with the outer layer coated with a conductive polymer that is grounded, where capacitive to digital converter IC are an integral part of the sensing array establishing a more distributed approach to data acquisition. The deposition of gold film underneath an insulator on a hollow elastic fiber is presented in [30] as an alternative capacitive design allowing for inclusion on stretchable fabric. Using MEMS fabrication methods and then weaving the coated fiber yields a tactile sensor where the range and sensitivity are functions of the hollow fibers diameter, thickness and Young's modulus. Of course one significant issue with capacitive sensors is with stray capacitance that degrades sensor performance and is present in all the above designs.

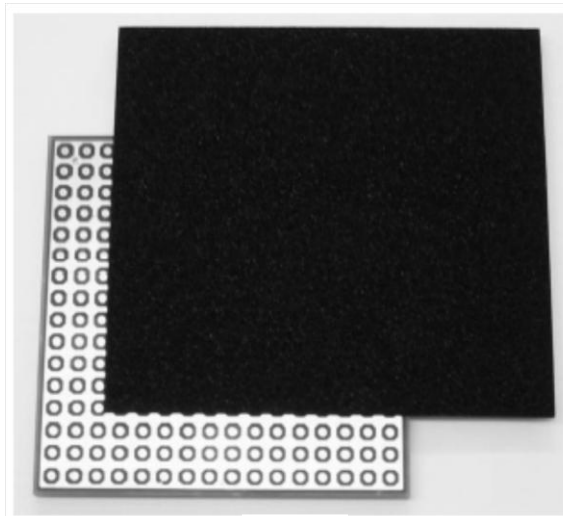
2.1.3 Piezoelectric Sensing

Sensors based on piezoelectric transducers convert applied stress into voltage. Eliminating the need for an excitation circuit, their integration on fully autonomous robots will minimize power consumption resulting in prolonged battery life. Both Polyvinylidene difluoride (PVDF) and Lead zirconate titanate (PZT) materials are most common. PZT ceramic is known to have superior piezoelectric properties but is inferior to PVDF in terms of flexibility and chemical inertness. In [6] and [31] the applications of piezoelectric transducers for foot soles and robotic skin are demonstrated. In [31], a 32-element microelectrode array is fabricated with FET device on the silicone die. The frequency response observed varied according to the type of material that came into contact with the sensor. Therefore, the feasibility for distinguishing material hardness is demonstrated. Despite the good dynamic response of these sensors, they tend to display considerable drift. Their pyroelectric effect is another drawback which requires continuous compensation based on the temperature.

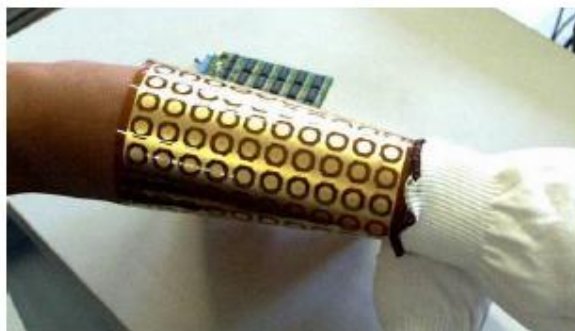
2.1.4 Optical

Designed prototypes of optical sensors are often composed of glass or Plastic Optical Fibers (POF's) in conjunction with an LED and a Charge Coupled Device (CCD) camera where forces are detected based on a change in the reflective wavelength. Typically, micro-bending and fragility are the main disadvantages incurred when using optoelectronics. However, light dissipation due to micro-bending is used as a sensing platform in [32]. POF's are arranged in a cross haired fashion and covered in silicon rubber for each taxel. The sensor has excellent linearity but with a limited range of up to

15N. A somewhat different approach is conceived in [33] where self contained modules with on-chip electronics allow for scalability. Photo-reflectors are covered in urethane foam acting as a uni-axial force transducer. Optical transmission does provide immunity to electromagnetic interference therefore tackling the cross talk problem associated with the majority of the tactile sensors introduced. The approach presented in [34] focuses on establishing an optoelectronic sensing system that allows for integration of a wide variety of sensors using a programmable converter to preprocess data on site prior to transmission to the central control unit.



(a)



(b)

Figure 2.4: Array based tactile sensor on flexible substrate [35].

In summary, the challenge of pressure measurement and tri-axial force measurement for robotic applications is still evolving. The pliability and stretch ability of the majority of the sensors is usually limited to the passive areas where there is no detection. Furthermore, the encapsulation with silicon rubber and PDMS has introduced a compliant layer that usually degrades MEMS performance with few exceptions. Fragility also remains an issue, where mechanically withstanding repeated twisting and flexion is rarely achievable. Conductive polymer and fabrics are of great interest due to their simple construction, but their implementation with electrodes undergoing loading significantly reduces their lifetime and reliability when under varying loads. Hysteresis and nonlinearity are two unavoidable obstacles, when dealing with compliant sensing structures. In addition, array type sensors, using any of the above transducers, have their spatial resolution dictated by the density of the matrix array. An example of this array structure is shown in Figure 2.4. Serial data acquisition techniques using multiplexers to minimize the wiring complexity tend to cause bandwidth limitations when larger arrays are implemented. Parallel schemes are simply not scalable for tactile sensing when covering larger areas. As a result, the overall use of taxels in an array type sensing platform suffers from a few critical limitations. Electrical Impedance Tomography based pressure sensing addresses some of these critical limitations by introducing a new sensing platform based only on measurements acquired from the boundary. The array structure is avoided, eliminating the need for electrodes withstanding repeated loading. The complexity is shifted onto the software side with the aim of reducing wiring complexity and simplifying transducer construction. The following section covers the current state of

this technology and the theory behind this primarily medical imaging technique in the tactile sensing perspective for robotic applications.

2.2 Electrical Impedance Tomography

This tomography method presents the conductivity distribution within a medium by having electrodes only at the boundary. Typically low frequency current is injected into the conductive domain and voltages are acquired from electrodes placed at the boundary of the medium under investigation. The spatial distribution of the impedance change is not strictly speaking measured, but calculated and is depicted on a 2-D or 3-D FEM model of the physical domain. Thus EIT has considerable potential due to its portable and cheap characteristics. Numerous applications such as medical imaging [36],[37] and geophysics [38],[39] have employed EIT. Industrial applications such as multiphase fluid flow [40] as well as batch process and mixing process monitoring have also benefited from this technology and are comprehensively reviewed by York in [41] .

Focusing on EIT based pressure sensing, Fulton and Lipczynski [42] as well as Booth and Basarab-Horwath [43] pioneered the introduction of the concept of EIT for planar pressure measurement in the early 1990's. Preliminary work in [44], attempted to utilize this method as a body support interface pressure measurement system for the clinical application of reducing patient bed sores. Investigating three different electrode placement configurations using a saline setup it was identified that having additional electrodes within the medium, which countered the non-invasive medical theme, enhanced image quality. Further work using a conductive polymer established the feasibility of the approach as presented in [45] but with no success in identifying suitable

materials for an effective sensor. In addition, taking advantage of the enhanced flexibility and stretch potential of the EIT sensor was not considered. Further work has been conducted recently by Alirezaei *et al* [46], [47] where emphasis was on the flexibility and stretch potential of these sensors and their integration in robotics as an artificial skin interface. Promising repeatable results were depicted but no performance measures were established to analyze the capability of the sensor to detect pressure and how accurately it can reconstruct the pressure profile. Tawil *et al* [48] focused on comparing alternative algorithms in order to enhance image reconstruction for the EIT pressure sensing application. With resolution acting as the only performance measure, Tawil *et al* concluded that drive patterns with internal electrodes and the Newton's One Step Error Reconstruction (NOSER) [49] proved most effective. Their forward model used for image reconstruction did not include a complete electrode model and there was no thorough investigation of the pressure and conductivity change relationship.

The following sections will give a brief explanation of the EIT algorithm starting with an explanation of the mathematical problem followed by the practical means of solving it which is decomposed into the forward and image reconstruction/inverse problems. EIT data collection and general instrumentation are also briefly highlighted.

2.2.1 Mathematical Setting

Finding the impedance distribution of a continuous conductive medium Ω with a boundary $d\Omega$ given a set of associated current and electric potential values is the essence of EIT. The associated mathematical formulation of the problem is very intensive but has

been thoroughly covered in the literature [1] [50][51]. The theoretical introduction of EIT commonly starts with the manipulation of Maxwell's equations to this form:

$$\nabla \cdot (\sigma \nabla V) = 0. \quad (2.1)$$

This Laplacian elliptical partial differential equation where σ is the conductivity which is equivalent to conductance in the one and two dimensional case and V is the scalar electric potential where the electric field $\mathbf{E} = -\nabla V$ is solved with the boundary condition given by

$$J_n = \sigma \nabla V \cdot \mathbf{n}, \quad (2.2)$$

where \mathbf{n} is a unit vector normal to the boundary. The boundary condition is based on the conservation of charge theorem where J_n is the current density on the boundary. In addition, a smoothness constraint is also added to solve the problem.

The numerical solution of the problem is achieved through FEM. The approach is analytically performed by solving the forward problem and then the inverse or so called reconstruction problem. For the Difference Imaging method, the forward problem finds the nodal electric potential distribution given a pre-specified conductivity distribution and electrical current data set. The inverse/reconstruction problem involves finding the conductivity distribution of the medium given a vector of measured electric potentials and applied excitation current vector via a Jacobian calculation. The EIT solution is depicted as change in relative conductivity. Both problems are discussed in the next sections.

2.2.2 Forward Problem

The forward problem is described as finding the spatial potential distribution of the discretized FEM of the domain given a known preset conductivity σ and constant applied current at the electrodes, found usually at the boundary of the medium. Solving the forward problem yields the simulated output voltage given for each node in the FEM including those attributed to the electrodes as a vector \mathbf{V} . The FEM here is considered as resistors connecting nodes together in a network to create a discrete domain under investigation, an approach established in [52]. The Direct Method, assuming linear shape functions and a constant conductivity distribution within elements is chosen here. The resistor network FEM is derived in detail by Graham [53] and Murai *et al* [54] based on which the following equations and derivation is acquired. The sheet conductivity is discretized in element form such that each edge of the triangular based elements has a conductance value of $\sigma \cot \theta_j$ as depicted in Figure 2.5.

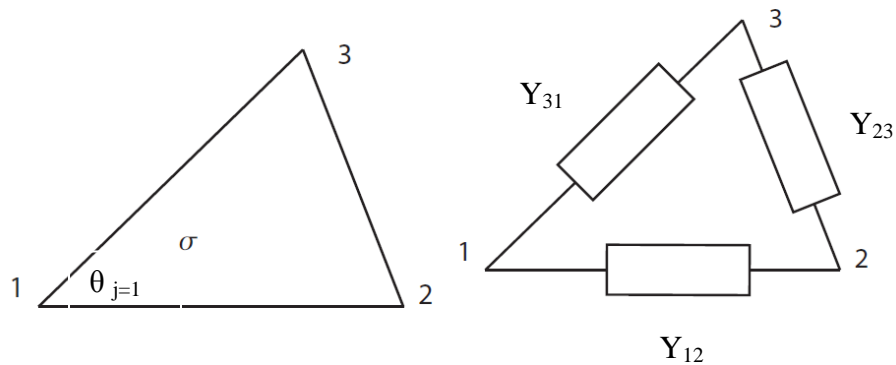


Figure 2.5: FEM resistor network [53].

This is presented in nodal coordinate form by

$$Y_{ij} = \frac{\sigma}{2A_e} (b_i b_j + c_i c_j), (i \neq j), \quad (2.3)$$

$$b_1 = y_2 - y_3, b_2 = y_3 - y_1, b_3 = y_1 - y_2,$$

$$c_1 = x_3 - x_2, c_2 = x_1 - x_3, c_3 = x_2 - x_1,$$

such that the specific numbering convention is followed. The element vertices are given by (i, j) , (x, y) are the Cartesian coordinates of the nodes and A_e is the element area. The local matrix is then generated to resemble Kirchhoff's current law, presented in matrix form as follows:

$$\begin{bmatrix} Y_{11} & Y_{12} & Y_{13} \\ Y_{21} & Y_{22} & Y_{23} \\ Y_{31} & Y_{32} & Y_{33} \end{bmatrix} \begin{bmatrix} v_1 \\ v_2 \\ v_3 \end{bmatrix} = \begin{bmatrix} q_1 \\ q_2 \\ q_3 \end{bmatrix}, \mathbf{Y}_e \mathbf{V}_e = \mathbf{I}_e. \quad (2.4)$$

where, $v_i (i=1,2,3)$ and q_i are the electric potentials and electric currents at the nodes respectively. \mathbf{Y}_e is the local admittance matrix, \mathbf{V}_e is the element voltage vector and \mathbf{I}_e is the element current vector. The remaining elements are found to be $Y_{11} = -Y_{12} - Y_{13}$, $Y_{22} = -Y_{21} - Y_{23}$, $Y_{33} = -Y_{31} - Y_{32}$. A transformation is then performed to generate the global admittance matrix for solving the FEM via the Direct approach. A visual demonstration is provided in Figure 2.6 for a two element case with four nodes 1 to 4.

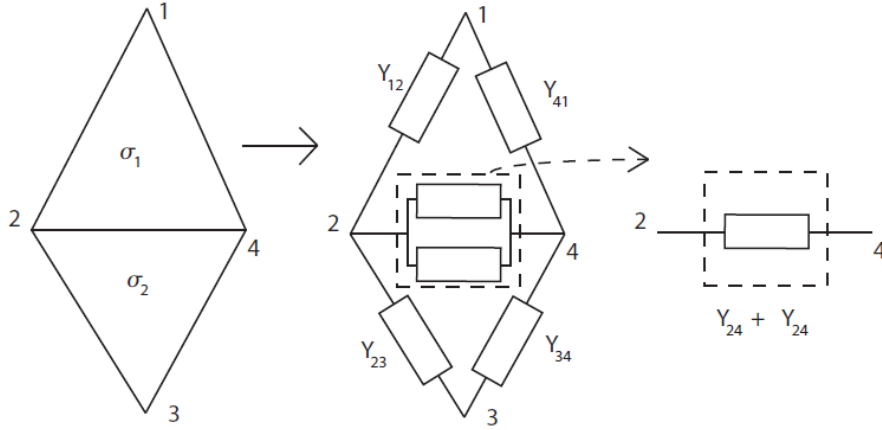


Figure 2.6: Local to global admittance matrix assembly example [53]

Here, the global admittance matrix \mathbf{Y} and global voltage and current vectors \mathbf{V} and \mathbf{I} are established as follows:

$$\mathbf{Y} = \begin{bmatrix} Y_{11} & Y_{12} & Y_{13} & Y_{14} \\ Y_{21} & Y_{22} + Y_{22} & Y_{23} & Y_{42} + Y_{42} \\ Y_{31} & Y_{32} & Y_{33} & Y_{34} \\ Y_{41} & Y_{42} + Y_{42} & Y_{43} & Y_{44} + Y_{44} \end{bmatrix} \quad i, j \in [1:4] \quad (2.5)$$

$$\mathbf{YV} = \mathbf{I}.$$

The forward problem algorithm steps used, as derived from [53] and [55], are summarized below to give the approach followed in the remainder of this thesis for EIT implementation.

1. Establish discrete model of continuum Ω using triangular elements in a 2-D mesh.
2. Assuming a homogenous domain, specify admittance value $\gamma = \sigma + j\omega\epsilon$, where ω is the frequency and ϵ is the permittivity.
3. Specify the current excitation pattern used by specifying \mathbf{I} .

4. Establish the local matrices of the element properties and then perform a local to global transformation to derive the system matrix \mathbf{Y} .
5. Implement the boundary conditions using a Point Electrode Model (PEM) or Complete Electrode Model (CEM) by selecting nodes on the mesh to be used as electrodes.
6. Specify grounding electrode node to make \mathbf{Y} nonsingular.
7. Solve the system of equations where $\mathbf{Y}\mathbf{V} = \mathbf{I}$ for \mathbf{V} (Kirchhoff's current law).

The forward problem is necessary for simulation purposes to find \mathbf{V} (spatial electric potential distribution) prior to the inverse reconstruction problem. It also establishes the FEM admittance matrix \mathbf{Y} which is used to generate the Jacobian for impedance calculation in the inverse/reconstruction problem. Solving the inverse problem requires the derivation of Jacobian matrix which is based on \mathbf{Y} as explained below.

2.2.3 Reconstruction

Since we are only considering difference imaging we will approach the formulation through that context. The derivation below borrows heavily from [53], [56–58]. The aim is to calculate the spatial conductivity distribution within the medium given a vector of voltage measurements from the boundary electrodes. The acquired signal is interpreted as a change in voltage measurements $\mathbf{z} = \mathbf{v}(t) - \mathbf{v}(t_{initial})$ where $\mathbf{v}(t)$ is a vector of collected voltages as a function of time.

$$\mathbf{z} = \mathbf{H}\mathbf{x} + \mathbf{n} \tag{2.6}$$

$$\mathbf{H} = \mathbf{T} \left[\mathbf{Y}^{-1}(\sigma) \frac{\partial}{\partial \sigma} \mathbf{Y}(\sigma) \mathbf{Y}^{-1}(\sigma) \mathbf{I} \right] \quad (2.7)$$

To find a linear operator that will calculate the change in conductivity $\mathbf{x} = \Delta\sigma$, where \mathbf{n} is the added noise, the derivation of the Jacobian matrix \mathbf{H} is necessary. For the sake of brevity a thorough derivation of the Jacobian is not provided in this work but as shown in (2.7) the Jacobian matrix is found using the admittance matrix where \mathbf{T} is an extraction operator that establishes nodal voltages between electrodes [53]. Assuming that the noise is negligible this allows us to implement a one-step solver that requires the inclusion of a regularization method.

2.2.3.1 Regularization

The reconstruction problem is classified as an ill-posed inverse problem [35]. The Jacobian matrix is ill conditioned meaning that small errors in measurement due to noise will result in large error amplification causing instability. The change in conductivity based on the Moore-Penrose pseudo inverse used to find \mathbf{x}_{MP} that minimizes the 2-Norm, fails in this case:

$$\mathbf{x}_{\text{MP}} = \operatorname{argmin}_{\mathbf{x}} \|\mathbf{H}\mathbf{x} - \mathbf{z}\|^2, \quad (2.8)$$

$$\mathbf{x}_{\text{MP}} = \mathbf{H}^\dagger \mathbf{z} = (\mathbf{H}^* \mathbf{H})^{-1} \mathbf{H}^* \mathbf{z}. \quad (2.9)$$

Consequently, the Tikhonov regularization method is adopted to address this problem and to ensure uniqueness of the solution:

$$\hat{\mathbf{x}} = \operatorname{argmin}_{\mathbf{x}} \{\|\mathbf{H}\mathbf{x} - \mathbf{z}\|^2 + \lambda^2 \|\mathbf{R}\mathbf{x}\|^2\}, \quad (2.10)$$

$$\hat{\mathbf{x}} = (\mathbf{H}^T\mathbf{H} + \lambda^2\mathbf{R}^T\mathbf{R})^{-1}\mathbf{H}^T\mathbf{z}. \quad (2.11)$$

The change in conductivity $\hat{\mathbf{x}}$ is achieved by adding an extra regularization term \mathbf{R} that provides apriori information that acts as a smoothness side constraint (2.10). \mathbf{R} is weighted by a scalar factor λ known as the hyperparameter. If $\lambda=0$ the result is what you would expect from the least square approach. The remaining variables are as described in section 2.2.3. Studying the ill conditioning with Singular Value Decomposition (SVD) is also present in the literature [1] but is not considered here.

The numerical implementation of the forward and inverse problem is carried out using EIDORS ver.3.5 [3] which runs over MATLAB.

2.2.4 EIT Data Collection and Instrumentation

There is a general architecture associated with EIT hardware platforms. This section relies heavily on the discussion by Holder in [1]. The goal is to excite the so called phantom using single or multiple current sources. Systems are classified as single or multi-frequency based, with low frequency ranges typically from 10 kHz up to 10MHz. Multi-frequency based systems are used to investigate the impedance dependence on frequency. Typically there are 16 or 32 electrodes allocated for phantoms used in 2D EIT that are positioned equidistantly along the boundary.

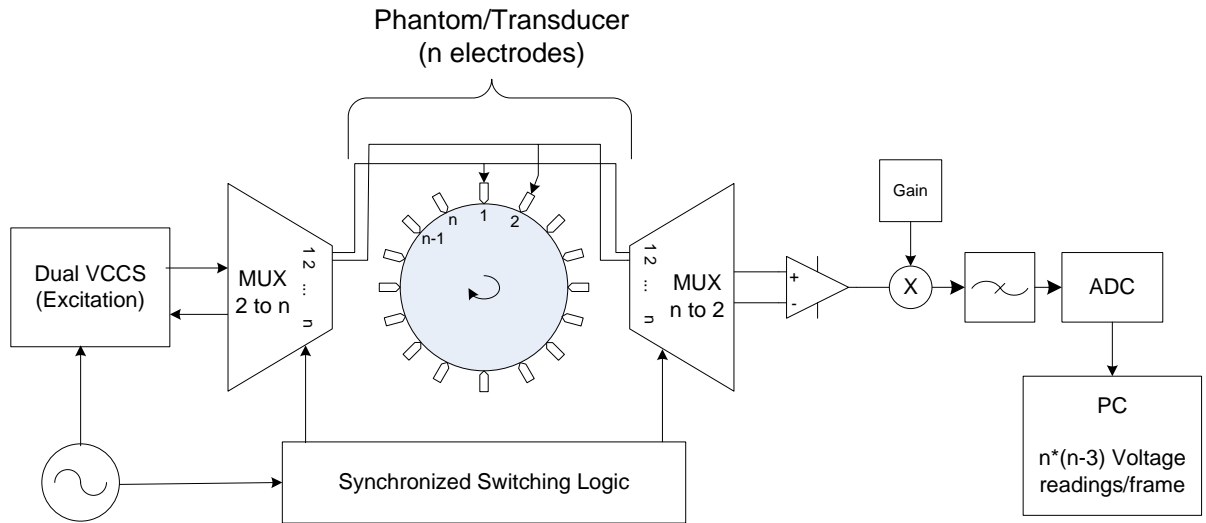


Figure 2.7: Overview of EIT hardware architecture.

A schematic of the general hardware platform is shown in Figure 2.7. A sinusoidal waveform generator is connected to a Voltage to Current Converter which is designed with an expected load impedance range while introducing a constant phase shift that can be compensated. The dual current source is necessary for excitation and is switched between electrode pairs according to the excitation pattern selected. Multiplexers are used for the switching process but they must be selected with minimal resistance and capacitive characteristics. In addition, differential or single ended voltage measurement is performed in a synchronized manner with the excitation circuit. Multiplexers are used to allow for adjacent, opposite or custom measurement and excitation patterns. Filtering is then performed and an adjustable gain is applied before analogue to digital conversion. Analog circuitry is the norm for most of the well

established systems but there have been studies using microcontroller based EIT systems [36] where the enhanced portability is beneficial for robotic integration.

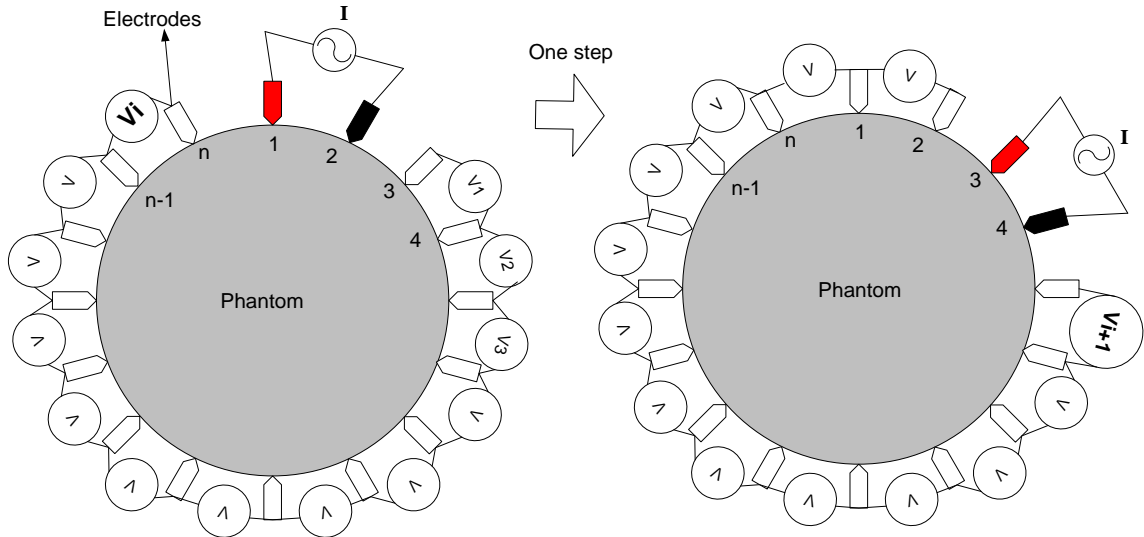


Figure 2.8: Adjacent drive pattern and the sequence of consecutive voltage measurements.

The excitation and measurement patterns used can be custom configured. However, the well accepted adjacent pattern as seen in Figure 2.8 is used throughout the experiments conducted. The bipolar current injection occurs between two adjacent electrodes. Voltage is then probed between all adjacent electrodes in a consecutive manner shifting by one electrode after each reading. Thus for one pair of excited electrodes, given a total of n electrodes; there are $n-3$ measurements. Therefore there are a total number of measurements equal to $n \times (n-3)$ which is referred to as a frame. Hence, for a 16 electrode configuration there are 208 measurements per frame. Current injecting electrodes are not used for taking measurements to avoid error due to any contact impedance mismatch.

Chapter 3

Experimental Setup, Methodology and Preliminary Results

The overall sensing technology and EIT method used for image reconstruction is discussed in this chapter. Sample classification is presented in Section 3.1. This is followed by preliminary testing of the piezoresistive materials responsiveness to pressure using a voltage divider circuit in Section 3.2. In addition, the hardware used and the EIT configuration is explained in Sections 3.3 and 3.4, on which the EIT sensor developments are based. Finally, the performance metrics used to analyze sensor performance are highlighted in Section 3.6.

The foundation of the EIT based distributed pressure sensor is to combine the ability to relate the pressure with the conductivity change, and to visualize the location of the stimulated area by only having the electrodes at the boundary of the conductive volume. Assuming an EIT hardware system is present, the implementation of a setup to investigate EIT based distributed pressure sensing is decomposed into three main stages:

1. Establishing a pressure sensitive resistive based sample with sheet resistance compatible with the EIT hardware platform;
2. Implementing a hardware setup to constrain sample, mount electrodes and to configure the excitation method to acquire raw data;

3. Data processing raw data to reconstruct pressure profile images based on developed model.

The output of the sensor is an image based on the FEM in the forward model. Each element of mesh has a conductivity value which in turn is associated with a pressure reading via calibration. Each of the above stages contributes significantly to the overall performance of the pressure sensor. It is required that the forward model used for image reconstruction matches the actual physical setup, involving the pressure sensitive medium used, and the mounted electrode positions to minimize errors. Medium material selection is important as its resistance change under loading will dictate the range and the pressure-conductivity relationship.

3.1 Transduction Method

Despite the vast amount of resistive tactile sensors found in the literature, the investigation of the actual cause of the load dependent resistance change that is exhibited has been limited. Typically, the resistive sensing elements that are constructed in a matrix have electrodes placed in the active sensing area. It has been indicated via experimental trials in [22] that the conductive polymer sheets used no longer demonstrate changes in resistance when glued using silver coated epoxy to identical electrode setups. The range is recognized according to the load value reached when 80% of the nominal interface area of the electrode has come into contact with the conductive sheet [22]. This lead to the conclusion that the sensor characteristics and range can be modeled extensively based on the surface roughness of the sensing element sheet. For our purpose the interpretation is

such that, a single layer of a conductive polymer material will not generate resistance changes under compression unless it is in contact with a second less conductive surface.

Based on the aforementioned analogy of contact impedance, a resistance change is detected when pressure is applied directly on a dual layer stacked arrangement. The approach used in our samples, is to select two conductive sheets so that the secondary sheet, which is mounted on top of the primary sheet, has a significantly lower surface resistance value. Electrodes are eliminated from within the sensing area and confined to the boundary allowing for improved flexibility and a more robust design. Electrode fatigue and degradation due to repeated loading is eliminated, which is expected to improve overall life cycle performance of the transducer. Two samples, as described in Table 3.1, are constructed using the stacked arrangement for use as flexible piezoresistive transducers.

Table 3.1: Stacked material samples as transducer elements.

	Mfg	Primary Element			Secondary Element		
		Material	Surface Resistance kΩ/sq	Thickness (mm)	Material	Surface Resistance kΩ/sq	Thickness (mm)
Sample #1	PCR Technical	CS57-7RSC Conductive Polymer	~100	0.5	Copper	Negligible	0.127
Sample #2	Eeoynx	NW-SL-PA Non-woven microfiber	2.0	0.8	NWSLPA Non- woven microfiber	1	0.8

- Sample #1: CS57-7RSC (PCR Technical) often referred to in the literature as Pressure Sensitive and Conductive Rubber (PSCR) is to be compressed on copper

sheet. It is essentially composed of silicon rubber impregnated with carbon filler supplied in 0.5 mm sheets (Figure 3.1(a)). The conductive polymer is very pliable and can withstand a repeated overload pressure of up to 6MPa.

- Sample #2: NW-SL-PA (Eeoynx) composed of a polyester/nylon filament blend is used. Both sheets of the non-woven microfiber fabric are flexible. They are coated with a conductive polymer by the manufacturer such that the surface resistance can be pre-specified. Two layers with different surface resistance properties are stacked for transducer implementation as shown in Figure 3.1(b).

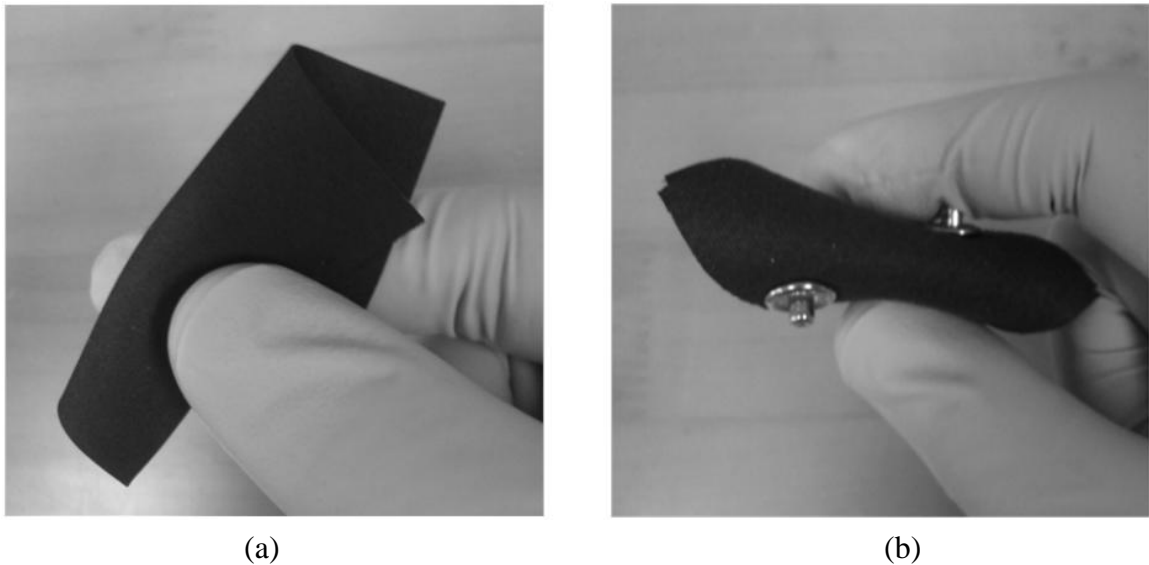


Figure 3.1: (a) Sample#1 demonstrating high pliability,(b) Stacked Sample #2 attached using electrodes.

3.2 Contact Resistance Material Characterization

The relationship between pressure and resistance of Sample #1 and #2 was characterized experimentally. A normal load was applied on the samples with coplanar electrodes to ensure the feasibility of the transducers via the stacked material specimen.

3.2.1 Method

A static compression test was performed with the resistance change being the only measurement of interest. A DC powered voltage divider circuit using a 12 bit ADC was used for resistance measurement, as shown in Figure 3.2. This approach is used as an initial simple testing method to inspect the functionality of the transducer. Data was acquired using Simulink through a function block based program. A low pass filter was added in the Simulink model for noise cancelation with a cutoff frequency of 10 rad/s and a unity pass-band gain.

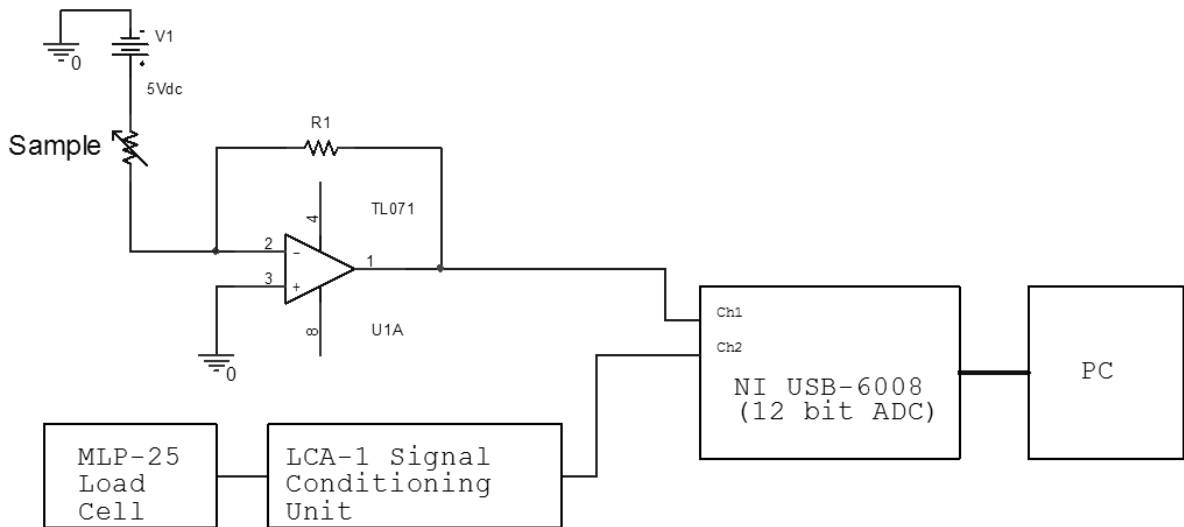


Figure 3.2: Schematic of DAQ circuit used for resistance measurement.

Copper sheet was used as electrodes for Sample #1 while Sample #2 had Stainless Steel circular button electrodes pierced into the sample as depicted in Figure 3.3. There was a fixed gap between the coplanar electrodes of 3 cm. The samples used here were square shaped measuring 5 cm by 5 cm.

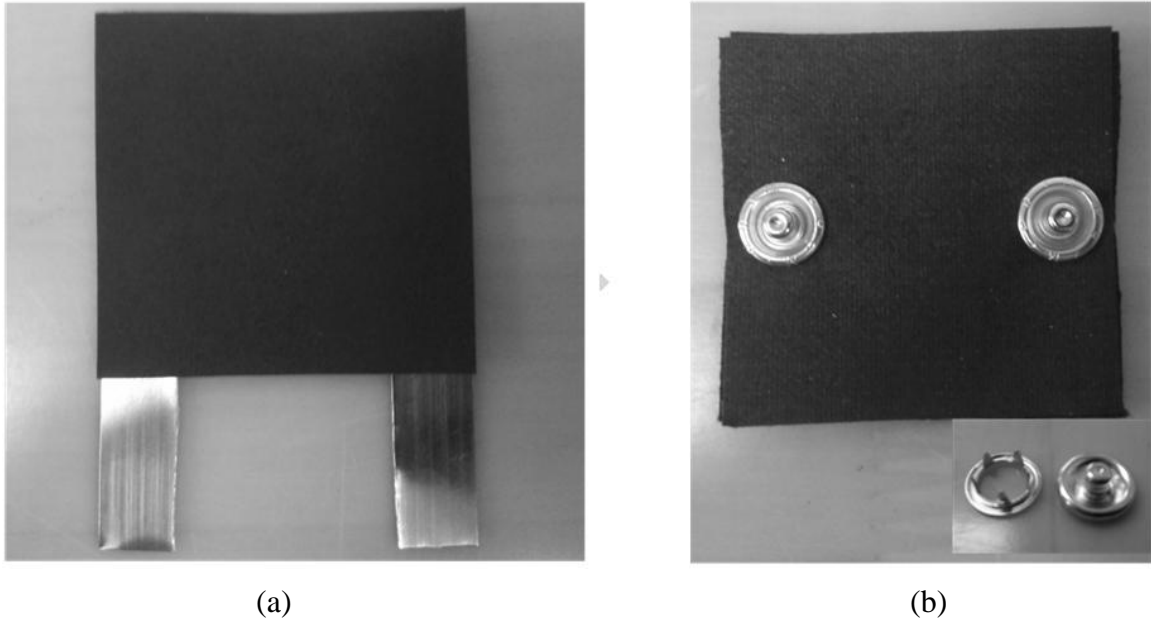


Figure 3.3: (a) Sample #1 measuring 5x5 cm, placed on copper electrodes with a 3 cm gap.(b) Sample #2 with same dimensions and pierced electrodes mounted with a 3 cm gap in between.

Simultaneous force measurement was recorded using a load cell mounted between two aluminum plates. Contact with the material was conducted through an insulator cut to size as seen in Figure 3.4. Furthermore, the mass of the load cell mount and insulated contact were recorded and accounted for during loading trials. Trials were repeated 3 times per sample. The maximum load applied was 100 N, limited by the load cell range. The load was incremented to the maximum loading state and then decremented to the initial no load state to establish a set of hysteresis curves where data was collected at a sampling rate of 100 Hz.

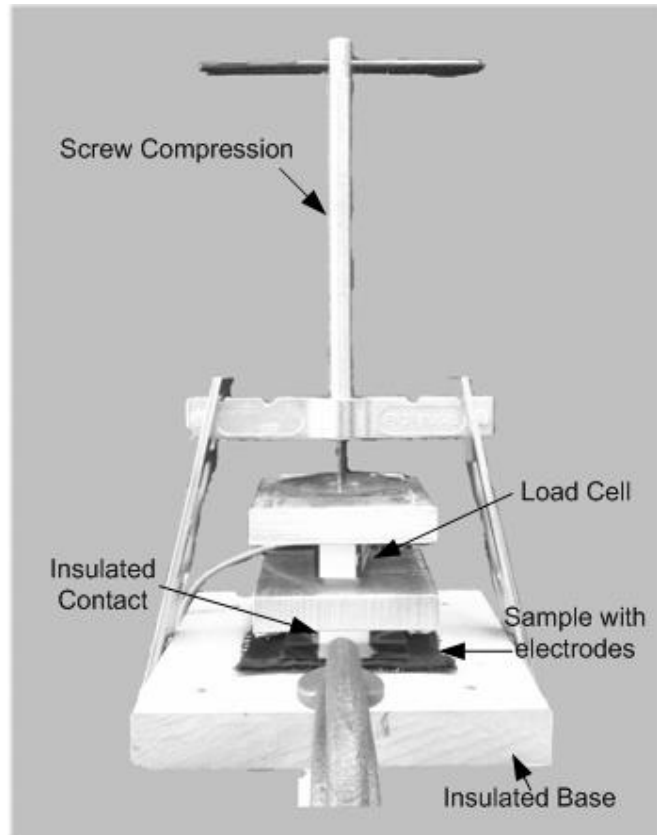


Figure 3.4: Loading apparatus for contact resistance investigation.

3.2.2 Results

The conductive polymer in Sample #1 exhibited a nonlinear decrease in resistance with an increase in pressure. With a 3 cm gap between electrodes the initial resistance was found to be 13.4 k Ω , recorded at 2.69 N, given the weight of the loading apparatus. The relationship is shown in Figure 3.5 for one of the 3 repeated trials.

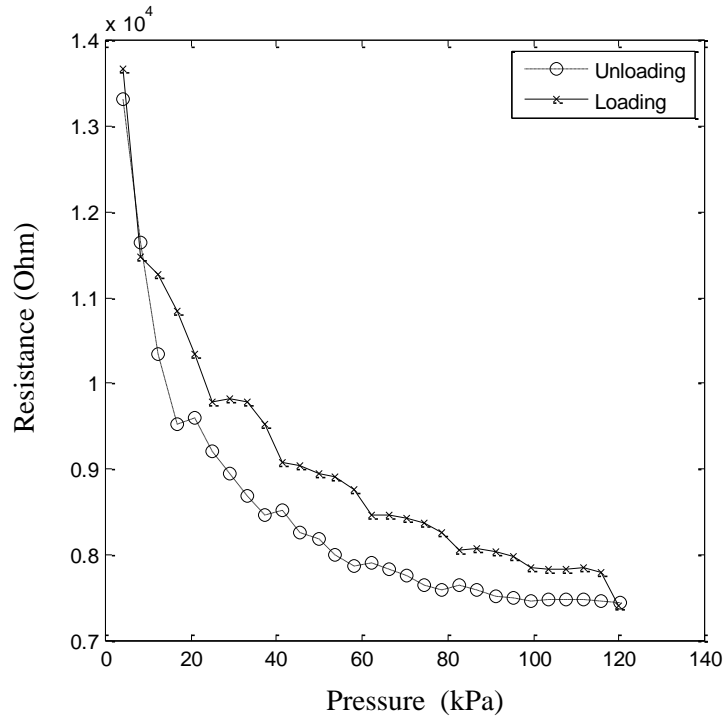


Figure 3.5: Sample #1 hysteresis curve.

A nonlinear relationship was also observed in the results collected for Sample #2 involving the stacked conductive polymer coated microfiber fabric. A steeper fall in resistance is exhibited up to 150 kPa range. The resistance declines with increasing pressure and saturates at 225kPa. The hysteresis curve is more pronounced compared to Sample #1 in all the repeated trials with a mean value of 28% of rated output. However, Sample #2 does not exceed a resistance of 2075 Ω (Figure 3.6).

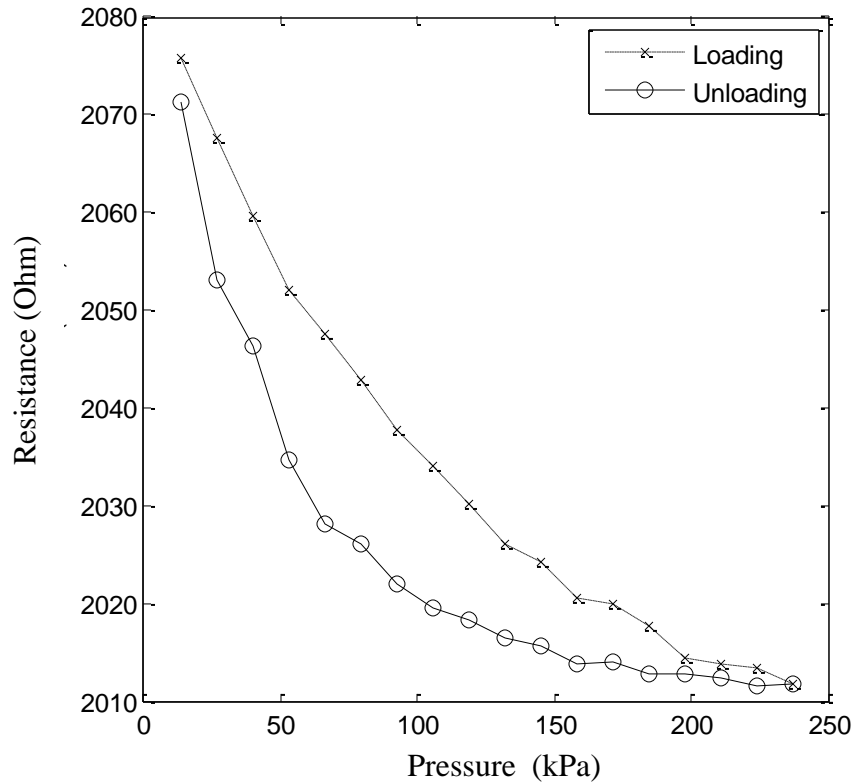


Figure 3.6: Sample#2 hysteresis curve.

Table 3.2: Transducer element characteristics.

	Anticipated Range (kPa)	Mean Hysteresis (% of Rated Output)
Sample # 1	100	20.2
Sample # 2	225	28.0

3.2.3 Discussion

Based on the contact resistance approach a nonlinear inverse relationship between pressure and resistance is concluded. The differences are pronounced in terms of the effective range. Both samples exhibited sensitivity to pressure with only Sample #1

requiring initial preloading due to its high no load resistance state. Sample # 2 is recorded as having the highest functional range of 225kPa. This pressure limit was also applied to Sample #1 but Figure 3.5 only depicts the effective range after which a change in resistance no longer exhibited a detectable decrease. The SigmaTom EIT system is typically used with impedance values of approximately 1 k Ω between electrodes thus it is anticipated that Sample #2 has more suitable impedance matching qualities based on these experimental trials. Conversely, Sample #2 experienced a resistance change of 63 Ω as opposed to the 5.9 k Ω change found in Sample #1. This indicates that Sample #2 has lower resolution in terms of pressure detection.

Secondly, the hysteresis specification of the specimen was another concerning factor. All the samples experienced high hysteresis values calculated as a percentage of the rated output. Sample #1 had a lower mean hysteresis value of 20%, while Sample #2 had a mean hysteresis value of 28% (Table 3.2). However, given the smaller relative change in resistance for Sample #2, a smaller voltage range is achieved over the pressure range, which is acquired with reduced accuracy due to limitations of the DAQ card used. Therefore, these values are only considered as initial estimates. The high hysteresis found in all the samples can be related to the stacked method in which the transducer elements were constructed. Since the samples were mounted with the electrodes as the only attaching mechanism, there is an air gap between the two layers. This contributes to a certain degree of looseness in the stack which can be related to the profound hysteresis. Sample #2, having the coarsest material texture, exhibited more creasing during testing due to electrode mounting method at these small dimensions (Figure 3.7). Therefore,

minimizing creasing of the pliable samples in the active area of the sensor might alter the hysteresis values significantly if larger dimensions are used.

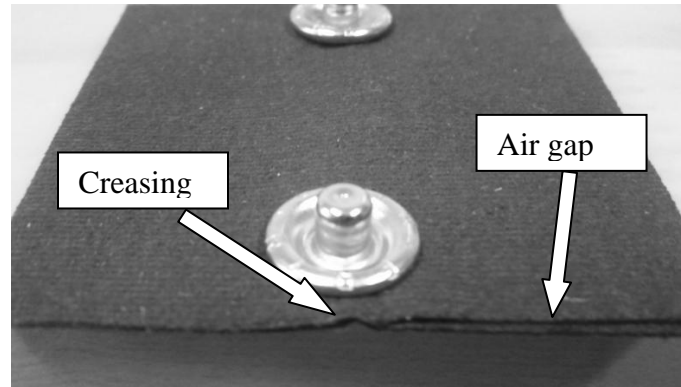


Figure 3.7: Creasing in Sample #2.

Alternative fabrication techniques for constraining the samples could also be beneficial, but they are not investigated further here. In addition, the inclusion of noise from the power supply also contributed negatively towards acquired data as visualized in Figure 3.5, given the coarse behavior of the loading curve.

3.3 Fixture Design

The aim of the fixture setup is to mount boundary electrodes on a sample while maintaining a fixed flat surface area in order to objectively evaluate the materials performance in EIT sensing. It also allows for replacing samples without the need to mount permanent electrodes for each sample. This fixture was only used with Sample #1 since the electrode mounts used for Sample #2 involved a different pierced mounting method.

The high flexibility of the conductive polymer dictated the fixture design with the primary aim of constraining the motion of the sample and fix the location of the electrodes within the conductive medium while loading. Motion artifacts are a major concern in EIT image reconstruction resulting from the undesirable movement of the electrodes during data collection [37]. These artifacts are found on the final image depicted by the EIT reconstruction algorithm, which lead to inaccurate depictions of the true pressure profile.

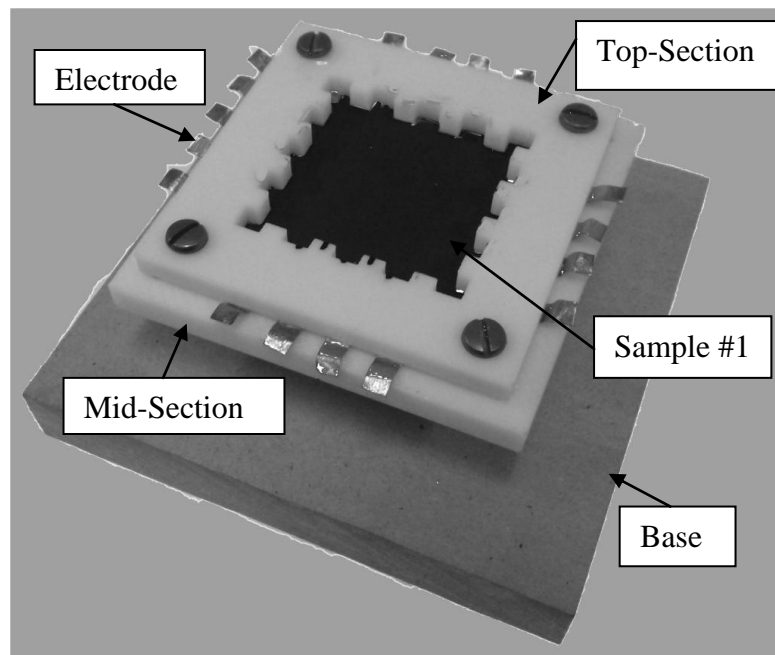


Figure 3.8: Fixture for Sample #1.

The fixture is composed of 3 parts; a base, midsection and electrode mount top section. All the parts were designed using CAD software (ProE ver.4). The functionality

of the base is to allow for stability during loading via clamping and is manufactured from Medium Density Fiberboard (MDF). The midsection is completely flat and is where the sample is placed. Both the mid and top sections were manufactured separately using a 3D printer and made of insulating ABS. Copper electrodes are cut to size from sheets and glued using epoxy cement on the bottom side of the top section where they fit under the teeth and extend beyond the edge to allow for clip on connections. The top section is then mounted on the midsection using 4 screws. A total of 16 electrodes in addition to a grounding electrode were used to conform to the scan-head used for data acquisition.

Table 3.3: Electrodes used with fixture.

Type	Press mount
Electrode Material	Copper
Thickness (mm)	0.127
Electrode penetration depth (mm)	3
Width (mm)	5
Centre to Centre Gap (mm)	10
Quantity	16 +1

3.4 Raw Data Acquisition

The SigmaTom II EIT system along with the Memtade software suite (Ecole Polytechnique of Montreal, Canada) was used for data acquisition as seen in

Figure 3.9. AC current at a preselected frequency, where the amplitude did not exceed 4 mA peak-to-peak, is used for excitation. This allows the signal recovered to have a real and imaginary component attributed to both resistance and capacitance changes in the sensing medium. The current amplitude and input signal gains are selected to enhance signal quality. The configurable parameters are listed in Table 3.4. The scan-head was also configured for an adjacent stimulation and measurement pattern. This method was selected due to its well established use in EIT literature. For all the conducted trials, voltage measurements were not acquired from the drive electrodes.

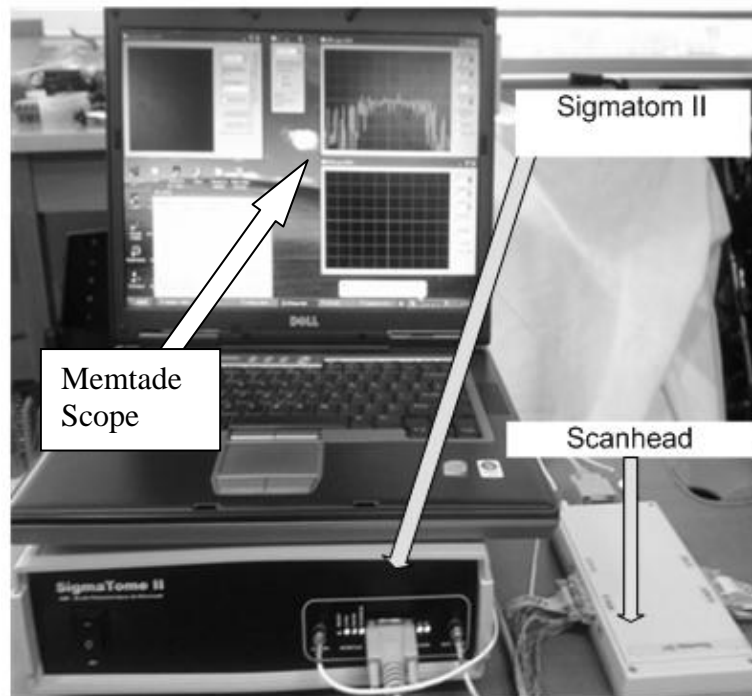


Figure 3.9: EIT instrumentation.

It is important to visually inspect the signal amplitude on the Memtade scope prior to data collection to ensure that voltage saturation is not taking place. If however, this is the case this means that the impedance between adjacent electrodes is too large and the addition of attenuators on the signal output coaxial cable line will be necessary.

Table 3.4: SigmaTom II configuration parameters.

Excitation Amplitude (%)	0-100
Excitation Frequency (kHz)	12.5, 20, 50
Frame Rate (fps)	1-50
Phase	0-360
Gain	1-10

3.5 Reconstruction

The physical modeling of the resistive element was achieved using EIDORS software [3]. This software platform available under a General Public License contains a multitude of algorithms for forward and inverse modeling for EIT. The 2-D Finite Element Mesh (FEM) of Figure 3.10 is constructed using triangular elements with normalized dimensions corresponding to the physical sample as shown earlier in Figure 3.8. It was generated using Distmesh which is integrated into the EIDORS package. It will be used as part of the forward model which is then used for image reconstruction. A uniform mesh density function was chosen for the mesh edge length. Sixteen rectangular shaped electrodes were selected to coincide with physical setup. A Complete Electrode Model (CEM) was chosen as opposed to a point electrode model where only one node per

electrode is possible. This allowed us to more accurately model the electrodes by defining the electrode shape, size and impedance. Four equidistant nodes were placed at each of the rectangular shaped electrode contact locations; however, current injecting electrodes were not used for taking measurements to avoid errors due to contact impedance mismatch.

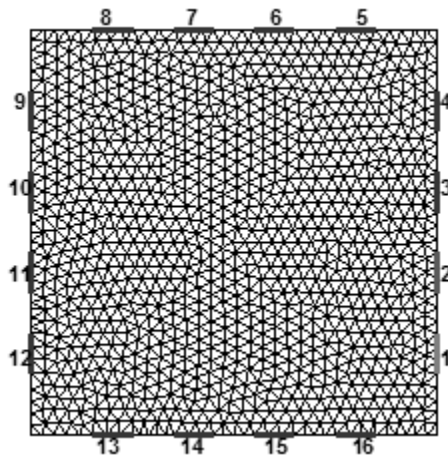


Figure 3.10: FEM discretization of the domain with 4078 elements and 2075 nodes with electrode placement.

3.5.1 Inverse Solver

A non-iterative solver is selected and is the only means of EIT evaluation being considered. A one-step solver is a requirement for the development of a feasible real-time EIT based pressure sensor, where iterative based solvers will only add to the undesired increase in the computational cost of the problem. The overall computational time given a one step solver will still depend on the forward model used for reconstruction, the switching speed of the multiplexers as well as the overall number of boundary electrodes from which data is acquired. The SigmaTom II system has managed image output at 50

frames per second for a 16 electrode configuration, but a thorough analysis of the computational speed can only be conducted once a complete real time sensor is achieved.

To carry out the calculation, the regularization matrix \mathbf{R} as described earlier in Equation (2.11) of Section 2.2.3, is specified. The Laplacian image prior is selected for this purpose as described in [3]:

$$\mathbf{R}_{m,n} \begin{cases} d + 1, & \text{if } m = n. \\ -1, & \text{if element } m \text{ is adjacent to } n. \\ 0, & \text{otherwise.} \end{cases} \quad (3.1)$$

All bordering elements indexed by m are weighted to -1 while the currently selected element n is weighted at $d+1$ where d is 2 in our case corresponding to the two-dimensional model. The inclusion of the Laplacian image regularization method produces smooth transitions between elements. This counters the coarse nature of the mesh and results in smoother images that distributes the ROI more evenly. This may reduce position errors due to the discretized model. However, it may also make it more difficult to distinguish sharp edges during pressure profile depiction.

Initially, a reference frame $v(t_0)$ is acquired at a no load state at time $t=t_0$ in order to realize a time difference imaging scheme. All consecutive data frames $v(t_0+\Delta t)$, after the application of pressure P , are collected and input to the solver on a frame by frame basis. The solver calculates the change in the conductivity distribution of the medium under investigation. The output is demonstrated in image form as depicted in Figure 3.11. The intensity of the image represents the pressure profile. The difference images may contain artifacts that are misleading additions to the pressure profile. The cause of these artifacts can be attributed to noise, electrode movement and the EIT reconstruction method. To minimize the inclusion of image artifacts in our analysis a Region of Interest (ROI) is

established. A maximum amplitude threshold is selected and a ROI data set composed of elements with values that are greater than quarter of the threshold are chosen. The mean value of the ROI is used to calculate the pressure value in terms of the conductivity change. The ROI is also used to calculate the centroid of the image for position error calculations as described in Section 3.6. A script was developed in EIDORS for implementing this sensor and for analyzing the reconstructed images.

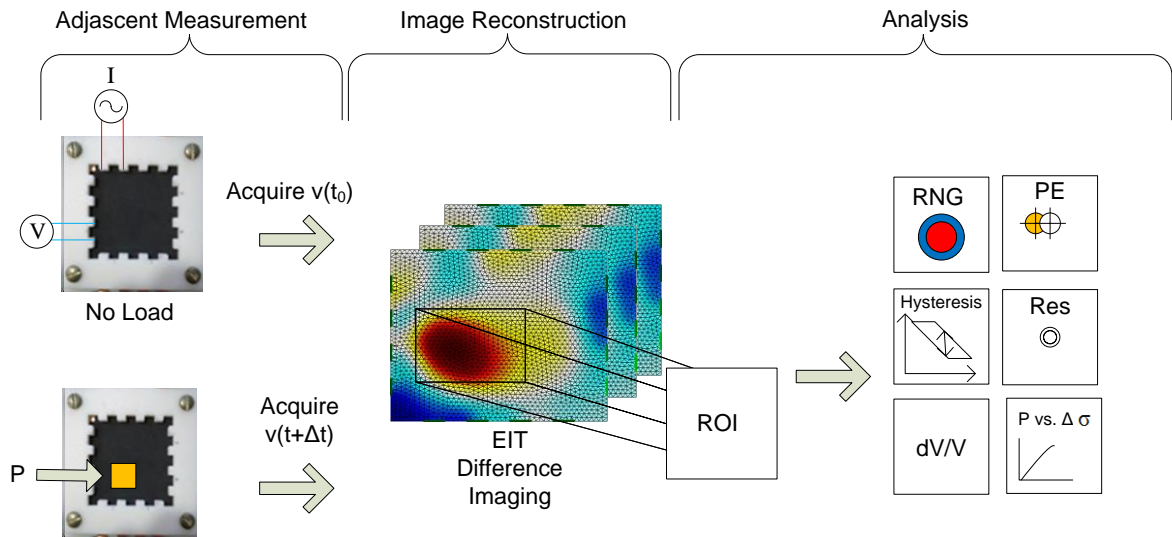


Figure 3.11: Procedure for EIT analysis.

3.6 Performance Evaluation Parameters

Based on the ROI, several performance parameters motivated by [59], [57] are used to evaluate the output image for the given EIT setup and configuration. They are as follows:

Relative Voltage Change is a performance measure that relies on the raw voltage data. It gives a preliminary means to evaluate the transducer elements sensitivity to applied pressure prior to the image processing stage:

$$\frac{dV}{V} = \frac{1}{N} \sum_{i=1}^N \frac{(V_i - Vu_i)}{(Vu_i)}, \quad (3.2)$$

V is a voltage measured for a frame consisting of N readings and Vu is the corresponding voltage reading for the reference frame collected at a no load state. Larger Relative Voltage Changes for an applied pressure corresponds to a more sensitive sensor.

Resolution is a unitless parameter not to be confused with the more common point to point spatial resolution specified in units of distance. As described in [57], it is the radius ratio of the reconstructed pressure profile as a fraction of the entire image:

$$RES = \sqrt{\frac{A_{ROI}}{A_o}}, \quad (3.3)$$

A_{ROI} and A_o are the sum of the number of elements within the ROI and the entire image respectively. Low and unvarying values, for an actual pressure distribution, repeated at different locations are desired. A non-uniform Res indicates errors in pressure profile depiction caused by variable shape distortion adding to the position error. Low values for a specific pressure profile indicate the desired capability of distinguishing multi-point contact.

Position Error is based on the centroid position of the reconstructed image pressure profile. It is calculated based on the ROI, where each element is weighed based on its conductivity value:

$$PE = p_t - p_c, \quad (3.4)$$

where negative values represent errors in the position away from the centre of the image. The target position p_t is the actual Centre of Pressure distance from the centre of the phantom and p_c is the distance of the centroid from the centre, of the ROI acquired from the sensor image. These positions are found from the normalized forward model and are therefore unitless. Desired values should be low and experience limited variability at different locations.

Ringing quantifies the image area outside the selected ROI that has an opposite change in conductivity:

$$RNG = \frac{X_{inv}}{X_{ROI}}, \quad (3.5)$$

where X_{inv} is the sum of the magnitude of all the elements outside the ROI with an opposite conductivity change and X_{ROI} is the sum of the element magnitudes within the ROI. It is expected that there only be a positive change in conductivity when the phantom exhibits a compressive load. Desired values should be low and uniform. However, high ringing will have no impact on the pressure calculation since the ROI will only have positive values.

Hysteresis is a typical sensor characterization parameter that is a critical factor when using conductive polymers and fabrics. The percentage value gives the widest deviation in conductivity readings for the same load after a loading and unloading cycle is completed over the entire range. It is calculated as follows:

$$\text{Hysteresis} = \left| \frac{\max\{\bar{X}_{\text{ROI}}(\text{loading}) - \bar{X}_{\text{ROI}}(\text{unloading})\}}{\text{Range}} \right| \times 100 \quad (3.6)$$

\bar{X}_{ROI} is the mean value of the elements found within the ROI which is also used to give a scalar conductivity reading for the applied pressure and is always positive.

Chapter 4

Pressure Distribution Sensor

Prior to sensor realization using different material samples, an evaluation of the EIT algorithm to be used is necessary. The analysis in Section 4.1 tests the impact the EIT data processing aspect has on raw voltage data. The EIT system benchmarking process is established through a reference saline solution setup which is considered reliable. By avoiding variability caused by material samples, via the saline setup, the extent of the errors introduced by the data processing aspect and the SigmaTom II system can be inspected more thoroughly. Secondly, a performance evaluation of pressure sensors using Sample #1 and #2 is presented in Section 4.2 where the sensors response to static loading and its ability to depict pressure profiles are investigated.

4.1 EIT System Performance Evaluation

Initial tests were required to ensure that no significant errors are caused by the implemented EIT reconstruction algorithm or the SigmaTom II hardware platform. Saline solution was suggested as a conductive medium to ensure a reliable homogenous medium that establishes consistent electrode contacts, with minimal noise interference. A series of experiments were conducted where the saline solution concentration was fixed. The volume of displaced solution was varied in addition to the position in relation to the boundary electrodes.

4.1.1 Method

Three experiments were conducted. The purpose of which is to identify the behavior of the system using a homogenous saline medium. Testing the ability to reproduce the same voltage change for a repeated stimulus is performed using nonconductive cubes. The position error, resolution and ringing metrics described in Section 3.6 are then used for quantifying the quality of the reconstructed images based on 2D EIT forward model. This is conducted for different stimulated positions in regard to the boundary electrodes to highlight the overall system capabilities.

A square shaped, semi enclosed Plexiglas container where the top surface is accessible is used for all three experiments. The bath dimensions were 21.5 by 21.5 cm with a depth of 6 cm as seen in Figure 4.1. Sixteen copper electrodes were mounted equidistantly on the edges to cover the entire depth of the container. The conductivity of the solution was set to 0.8 mS, as recommended for the SigmaTom II system, which was measured using a conductivity meter (EC TesTr). This conductivity is selected such that it is not too low such that the impedance between neighbouring electrodes is not large enough to saturate the acquired raw voltage data. Furthermore, it is not set too high to allow for sufficient time for experiments while minimizing electrode corrosion. The SigmaTom system was configured with a current excitation frequency of 50 kHz and a gain of 3. The plateau shaped signal was visually inspected prior to data collection to ensure that all electrodes were connected. Twenty frames were collected per load and the mean value was used to display the results to further reduce the impact of noise. The mean value of the change in conductivity based on a $\frac{1}{4}$ amplitude threshold ROI is also found and used to present the hysteresis curve.

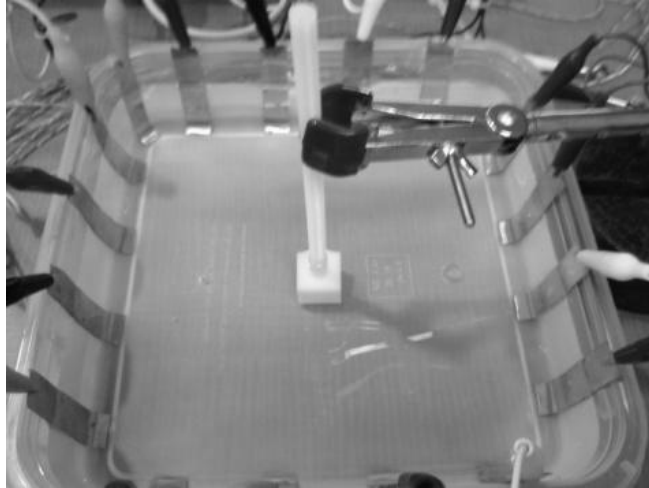


Figure 4.1: Nonconductive cube placed in saline solution, in semi-enclosed container.

The apparatus and reconstruction method described above are used for the following three experiments:

- *Experiment 1:* (Figure 4.2(a)) was carried out by varying the depth of a fixed volume, nonconductive cube, at the centre of the saline solution starting at the surface. This causes voltage changes to be acquired by the boundary electrodes. This resembles the voltage change acquired when pressure is applied to material samples but with anticipated negative conductivity change.
- *Experiment 2:* Three nonconductive cubes with different volumes ranging from 5 to 21 cm³ were submerged at the centre of the container as depicted in (Figure 4.2(b)). The cubes COG is set at a constant depth while ensuring complete submersion. This serves as an alternative stimulation mechanism compared to Experiment 1. This was conducted in an ascending then descending manner at the centre of the saline solution. The solution was left to settle for a period of 30

seconds in between data points. This procedure is followed to avoid water ripples that cause variability in the contact impedance of the electrodes. Such inconsistency can negatively impact the reconstruction problem where all electrodes in the model are assumed to be identical.

- *Experiment 3:* The ability to detect the location of the stimulus over half of the symmetric area was tested by shifting the location of the nonconductive cube measuring 2 cm x 2 cm x 2 cm in 3 cm increments in the x and y direction. Thirty second intervals were left between measurements to accommodate for water ripples. The drift experienced with a stagnant saline solution setup was then inspected with no cubes present. The drift measurements were recorded with 30 second intervals for a total of 120 seconds to investigate the presence of drift noticed on the raw voltage data.

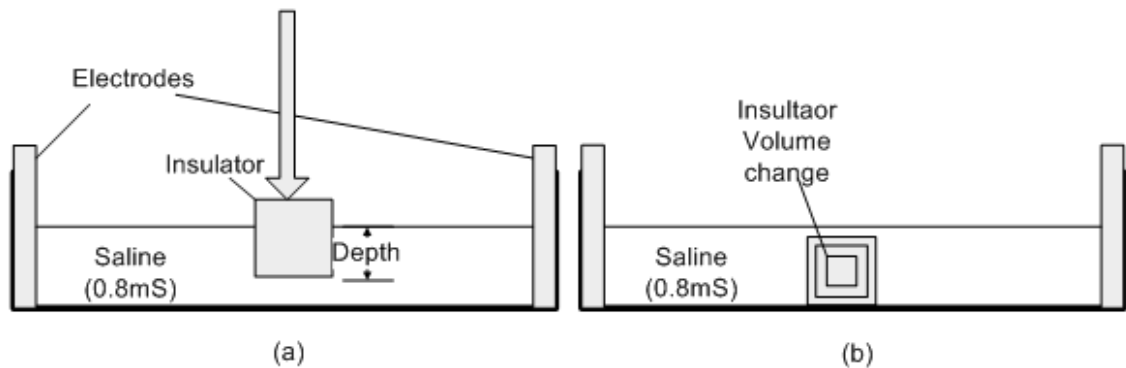
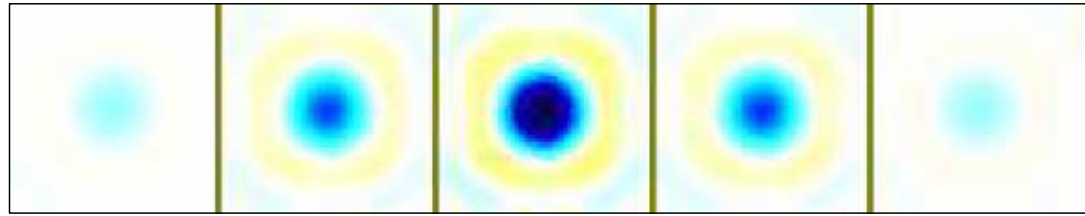


Figure 4.2: (a) Displaced saline volume by varying insulator depth. (b) Changing insulator cube volume.

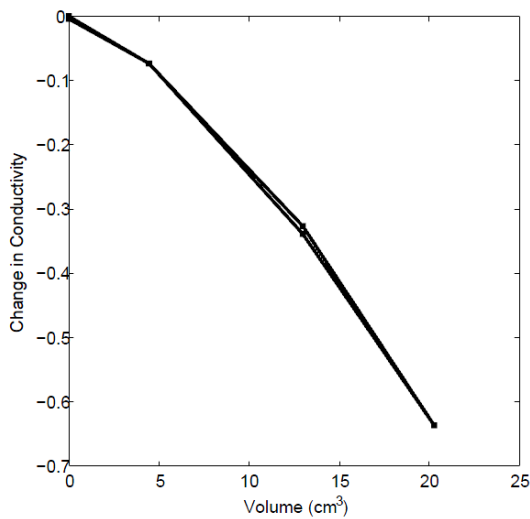
4.1.2 Results

4.1.2.1 *Experiment 1*

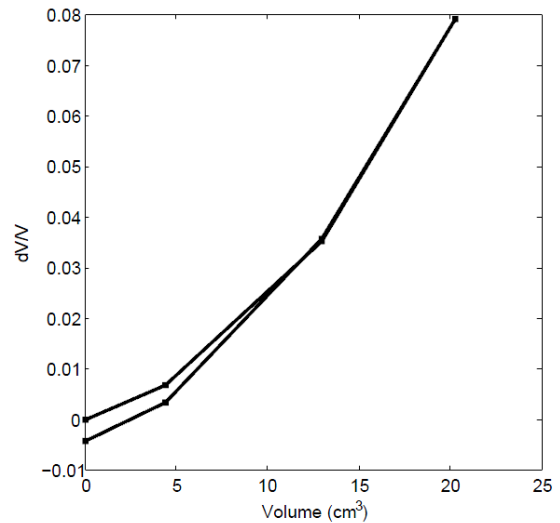
The image based conductivity change is depicted as a function of volume in Figure 4.3(b). Since the volume of displaced saline is replaced by a nonconductive medium, the change is a negative one, depicted by blue regions in the images in Figure 4.3(a) as opposed to positive red regions. The blue regions intensity corresponds to the magnitude of the conductivity change. The yellow regions found beyond the edges of the stimulated area are a display of the ringing effect. It is found that there is a minor difference in the conductivity, based on the image output, when returning to the same volume of displaced solution. Furthermore, the relative change in voltage shown in Figure 4.3(c) displays the raw signal data that has a minute error, which has no effect on the image output, when using a quarter amplitude threshold based ROI for the conductivity calculation.



(a)



(b)

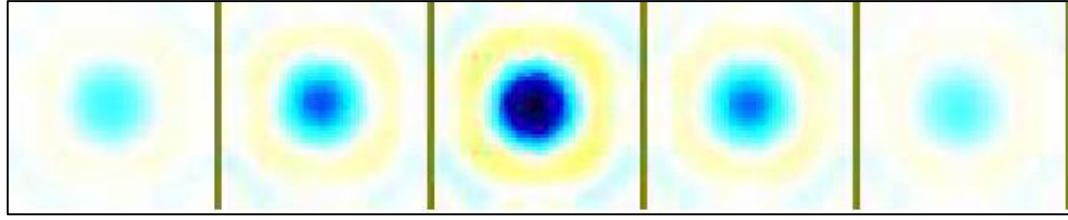


(c)

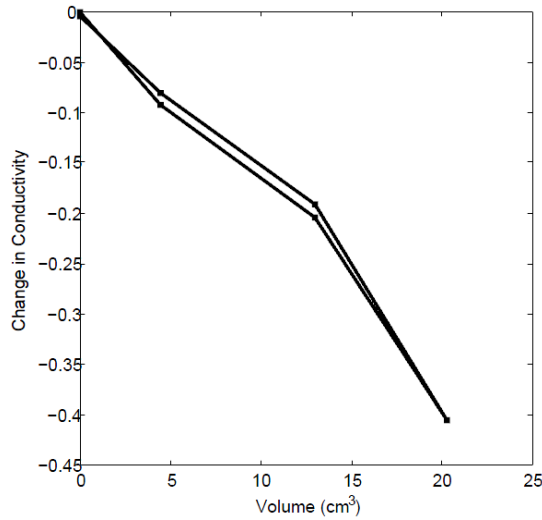
Figure 4.3: (a) Left to right, images for volume of displaced saline (b) Associated change in conductivity for 3 different volumes (c) Relative change in raw voltage data.

4.1.2.2 Experiment 2

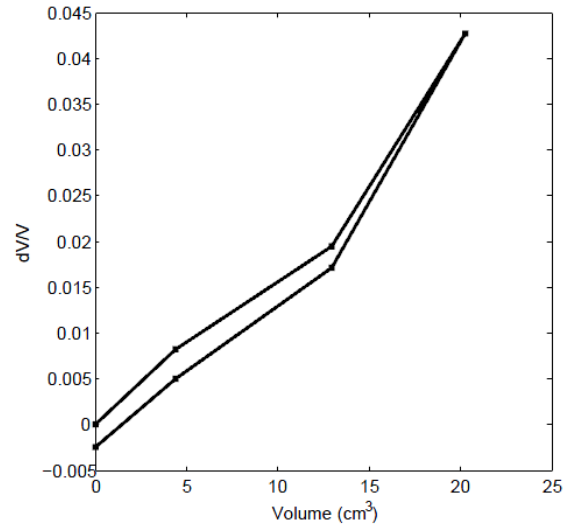
The approach follows the same overall scheme as the first experiment but with a minor alteration of the stimulation method. The nonconductive cube was lowered using a clamp while its x and y coordinate positions were fixed at the centre of the container. Figure 4.4 shows how the change in conductivity is consistent among different volumes of displaced saline as well. The hysteresis due to the EIT method used is found to be 1.06 %.



(a)



(b)



(c)

Figure 4.4: (a) Left to right, images for volume of displaced saline by changing cube depth (b) Associated change in conductivity for 3 different volumes (c) Relative change in raw voltage data.

4.1.2.3 Experiment 3

The Centre of Gravity (CoG) position of the non conductive cube of fixed volume was varied in order to investigate the performance of the EIT system as a function of distance from the boundary electrodes. Figure 4.5 shows the images associated with Experiment 3 for each position. A maximum position error of 4% was found for all the readings as seen in Figure 4.6. It is also evident that the position error is higher when the stimulated area is along the edge line at $x = 6$ cm from the centre. The resolution was also found to

improve with the x coordinate being closer to edge of the medium. In addition, the further towards the centre, in terms of y coordinate movement, the poorer the achieved resolution. The largest deviation in RES was found to be 10% of the total surface area, between the centre and the corner of the conductive medium. Ringing was mostly constant for the same y locations of the CoG but was found to be more significant the closer the phantom was to the electrodes.

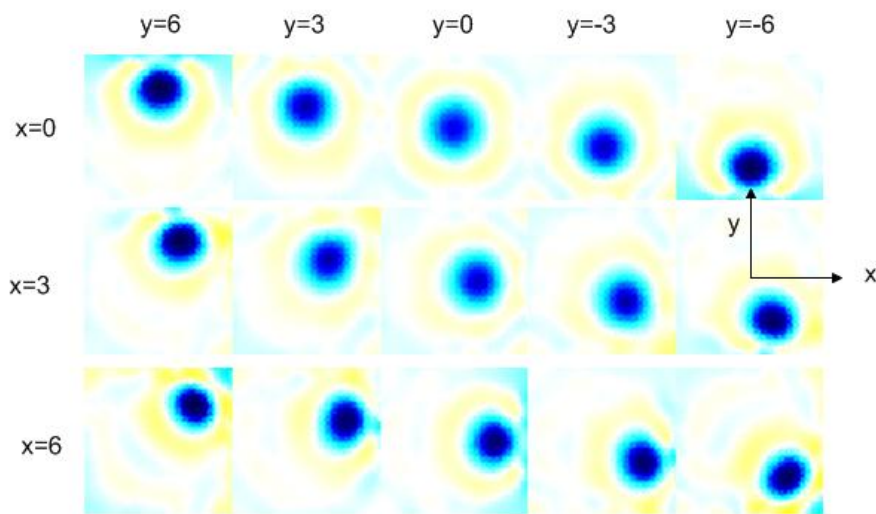


Figure 4.5: Sensor images for different (x,y) cube CoG positions in cm.

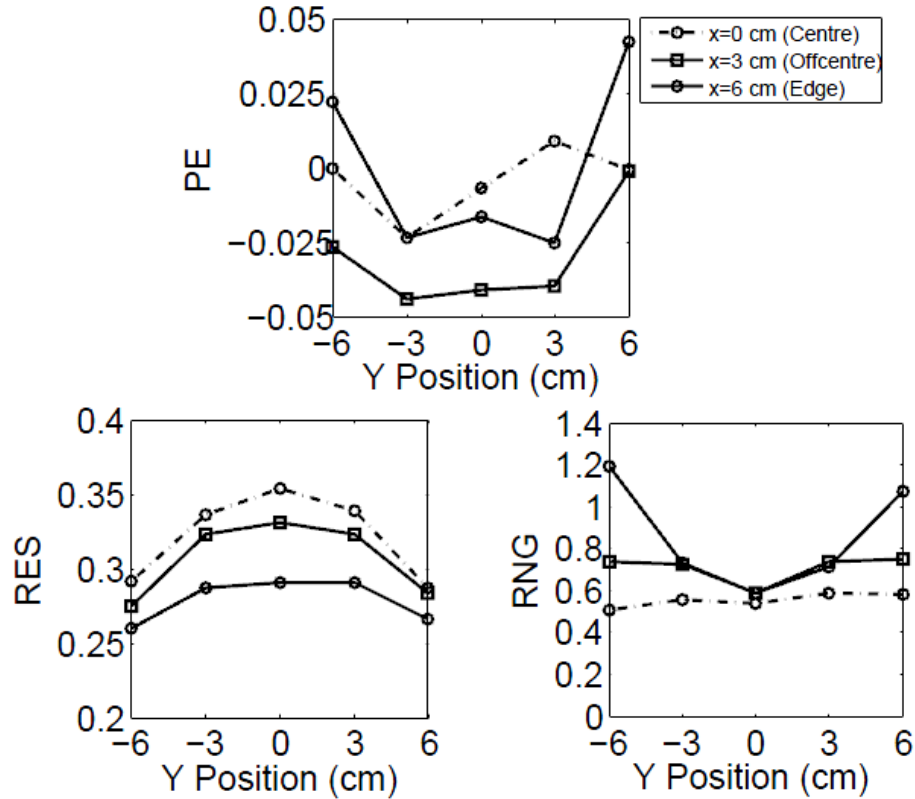


Figure 4.6: Position Error (PE), Resolution (RES) and Ringing (RNG) for different CoG positions in regard to boundary electrodes.

The fractional change in boundary voltage data, calculated as per equation (3.2) in section 3.6, of the undisturbed saline solution are depicted in Figure 4.7. The drift curves for three consecutive trials are 1 order of magnitude smaller than any change in boundary voltage data detected during the displaced saline volume experiments. The rate of increase is drastically reduced after the 60 second mark for two trials while the third exhibited minimal drift for the two minute period.

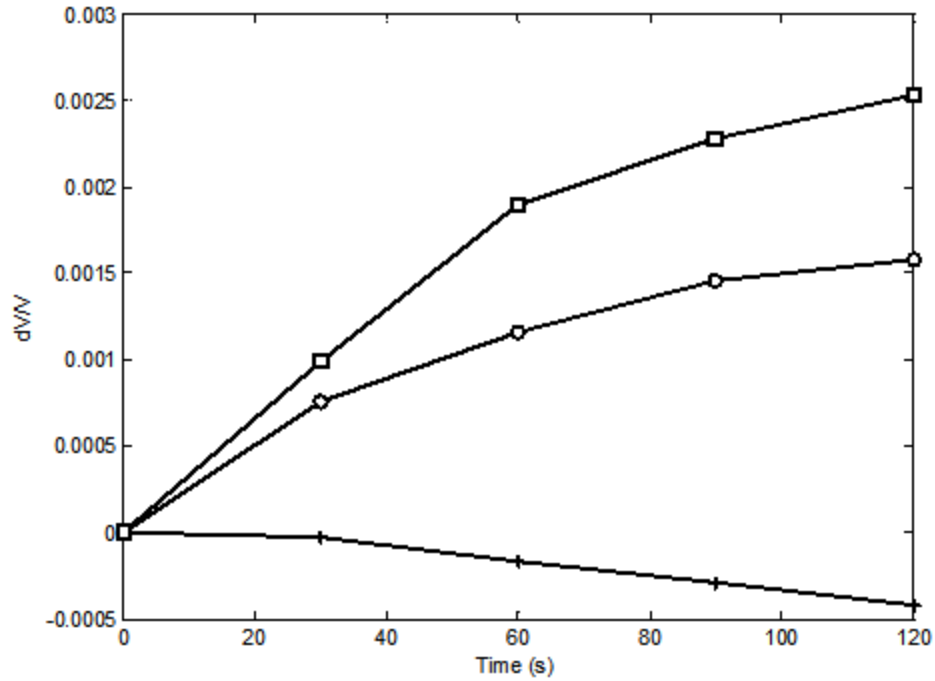


Figure 4.7: Drift in fractional change in voltage for three trials.

4.1.3 Discussion

The SigmaTom II along with the rest of the EIT system was analyzed to establish a reference performance level using a 0.8 mS saline solution. The reconstruction configuration was validated via both stimulating methods conducted in Experiment 1 and 2 respectively. The reproducibility of the results was confirmed when identical conductivity readings were found for the same saline volume displacement. This highlighted that the impact the data processing aspect had on the final sensor output did not in any way add errors that may contribute to exaggerated hysteresis values. This entails that given a consistent electrode-medium interface and a homogenous phantom

that matches the input impedance range of the EIT system, the sensors reconstruction and image processing aspects are effective and reliable.

Several phenomena have also been highlighted by the results. The dependence of the position error on the stimulation location was recognized. These can be attributed to shape deformations as seen in the sensor images (Figure 4.5) which are amplified with closer proximity to the boundary electrodes. The higher position errors found in the off-centre line can also be attributed to additional blurring as seen by the higher RES values in Figure 4.6 compared to the edge line. Overall, the position errors were found to have low magnitudes mainly due to the lack of artifacts in the images. Furthermore, the discretization of the medium via the FEM adds to the position error. Increasing the number of elements will reduce numerical error, but will add to the computational cost of the sensor; therefore, a tradeoff is necessary between resolution and speed. The data also indicates a correlation between resolution degradation and distance from the boundary electrode arrangement. This is shown in Figure 4.6, where the Res value increases for each of the centre, off-centre and edge lines as $y=0$ cm is approached. The resolution is also consistently improving as the x coordinate shifts from $x=0$ to $x=0.4$ cm; demonstrated by the increase in Res values in Figure 4.6 between the centre, off-centre and edge paths. Despite the presence of ringing in the reconstructed images, their impact is isolated via the presence of the ROI selection approach. As such their inclusion in finding the conductivity change is completely eliminated despite their visual presence. In addition, the drift was also found to be minute in comparison to the changes in conductivity and is not considered a major concern.

4.2 Sensor Performance Evaluation

The material presented in the following section regarding experiments on the conductive polymer was partially published in the *ASET 2012 International Conference on Electrical and Computer Systems, Ottawa, Ontario, Canada*. [2]. Following the EIT benchmarking process in the previous section it was necessary to implement the EIT based pressure distribution sensor using both conductive samples described in section 3.1. A detailed description of the methodology used and the results are presented here.

4.2.1 Method

To characterize the performance of the EIT pressure sensor, two main experiments were performed. The objective is to quantify the sensor's ability to detect pressure and its effectiveness in producing a pressure profile over a planar sensing area. The conductive polymer in Sample #1 and the polymer coated microfiber used in Sample #2 were tested respectively. The sensor functioned by first acquiring no load reference voltage data given an adjacent current stimulation and measurement pattern. Data are then compared to this reference state that is only set once at the beginning of both experiments. Each experiment was repeated 3 times to ensure the repeatability of the results. In addition, the mean value of 20 frames was taken for each static load for improved noise averaging.

Table 4.1: EIT configurable parameter settings.

	Sample #1	Sample#2
Frequency (kHz)	12.5	50
Gain	5	3
Amplitude (%)	100	7.82
Attenuators	1*20dB	None
Frame Rate	4.73	4.73
Regularization Method	Laplacian	Laplacian
Data Type	Real	Absolute
Hyperparameter	0.032	0.150
Active Area Dimensions	50mm*50mm	210mm*210mm

- *Static Loading Experiment:* In this experiment pressure was varied at a fixed location in order to establish the relationship between pressure and conductivity change. A 4 cm² square shaped insulated contact was placed at the centre of the phantom where pressure was applied. Fixed weights were added on top of the contact area for loading. Pressure readings used for calibration were calculated based on the force measurements from a precision weight scale (AND EJ-4100).
- *Pressure Map Experiment:* Contrary to the first experiment, here the load applied was fixed and the location of the stimulated region was varied over the sensing surface for one specific pattern. An identical square shaped insulated contact with the same dimensions of 4 cm² was used. A fixed weight of 1kg was applied with 10 second intervals between measurements. The EIT sensor's reconstructed images depict the relative conductivity change which is directly attributed to the pressure profile of the stimulus.

4.2.2 Results

The acquired data for both experiments are discussed, investigating the pressure response and image quality of the EIT sensor.

4.2.2.1 Static Loading Experiment

The pressure was incremented up to the maximum applicable range then decremented to the original no load state to create the first order hysteresis curve. The calibration curves for Sample #1 presents an evident nonlinear relationship between pressure and the change in conductivity relative to the no load state of the sensor. The hysteresis is calculated to be 34.5 % of the rated output span where the deviation seems highest when returning to about a third of the maximum load (Figure 4.8). Furthermore, changes in conductivity are undetected beyond 35 kPa; hence, establishing the range of the sensor.

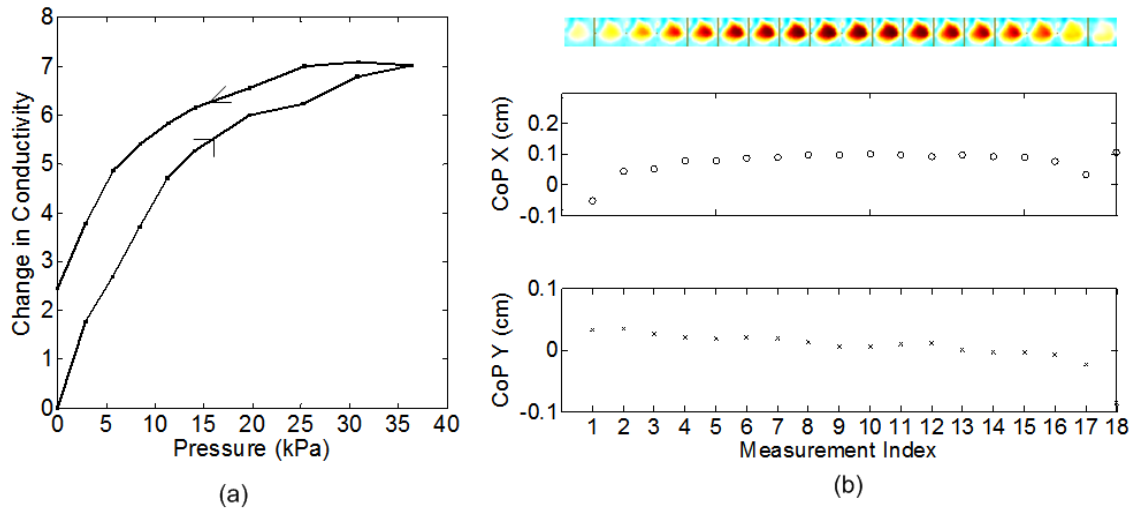


Figure 4.8: (a) Sample 1 sensor calibration and hysteresis curve, (b) Top, Sensor image for variable loading with fixated contact location, (b) Middle and bottom, the variations of the CoP in the x and y directions for constant location at the centre of the phantom and under variable normal load.

Given the fixed location of the load there are recorded position errors. The centroid of the ROI varied in the x and y axis from the centre of the phantom as shown in Figure 4.8(b) for each normal load measurement. The position errors are minor with a mean value of 4.6% of the normalized length of the Sample dimensions which corresponds to 2.3 mm for Sample #1.

Sample #2 was successful in terms of sensitivity to normal pressure. It was characterized with a larger range with detectable responsiveness of up to 65 kPa as shown in Figure 4.9(a). A nonlinear behavior was also present. The images from the sensor indicated far less blurring around the stimulated area. The hysteresis value was found to be 20.03 % which is lower in comparison to Sample #1, but still a significant impediment to sensor performance. Position errors were also considered low with a maximum mean value of 3.2 % in the y direction based on this experiment as shown in Table 4.2.

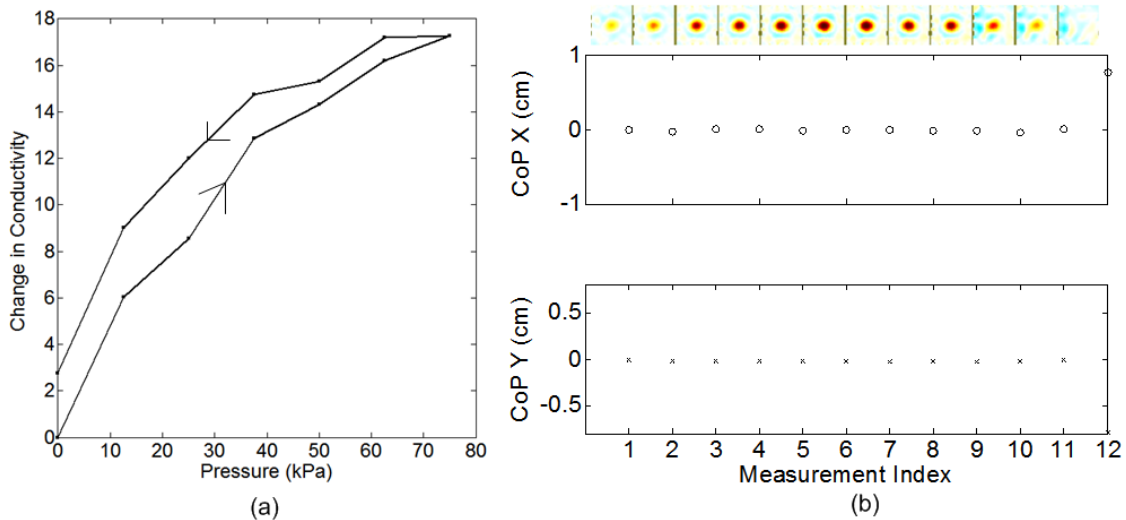


Figure 4.9: (a) Sample #2 sensor calibration and hysteresis curve. (b) Top, Sensor image for variable loading with fixated contact location. (b) Middle and bottom, the variations of the CoP in the x and y directions for constant location at the centre of the phantom and under variable normal load.

Table 4.2: Sample characteristic based on static loading trials.

	Range (kPa)	Hysteresis (Mean)	Normalized CoPx Error (25 Trials)		Normalized CoPy Error (25 Trials)	
			Mean	S.D	Mean	S.D
Sample 1	35	34.50	0.046	0.042	0.022	0.050
Sample 2	65	20.03	0.001	0.122	0.032	0.099

4.2.2.2 Pressure Map Experiment

To investigate the performance of the active sensing area, the location of a square shaped contact was varied over half the area. Due to the symmetric electrode pattern it is assumed that similar results would be acquired over the second half of the square sensing area, given the homogenous nature of the phantom. The stimulation was conducted via the pattern shown in Figure 4.11(a) starting from top to bottom then left to right.

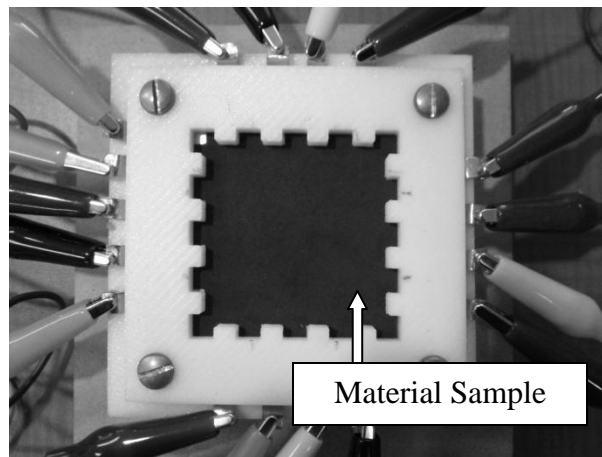


Figure 4.10: Sample #1 in fixture with connected electrodes.

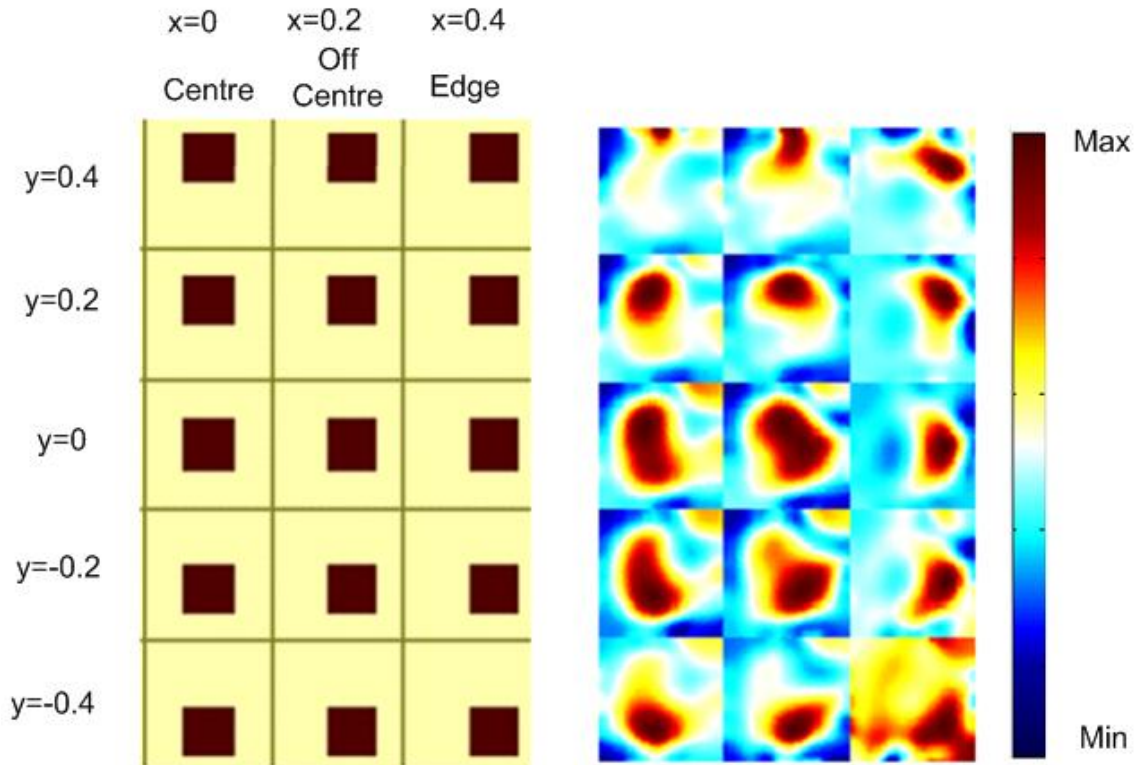


Figure 4.11: Position 1 to 15: from left to right, top to bottom (cm). Applied pressure at the specified location depicted on the left with square shaped contact scaled to size and the actual corresponding sensor image to the right for Sample #1.

The developed EIT pressure sensor based on Sample #1 (Figure 4.10) was successful in reconstructing images of the pressure profile over the active sensing area but with added distortion. According to Figure 4.11, a total of 15 positions show that the images had degraded resolution at the centre and off-centre lines of the phantom compared to the edge line, which is closest to the electrodes. Moreover, shape deformations were found to be more significant with increased proximity to the boundary electrodes. Prior stimulated locations are also present in consecutive images suggesting that the material has a memory (Figure 4.9). As such large CoP position errors were also

recorded when the stimulated area was at the centre as shown in positions Figure 4.10. Ringing is also present in the majority of the images.

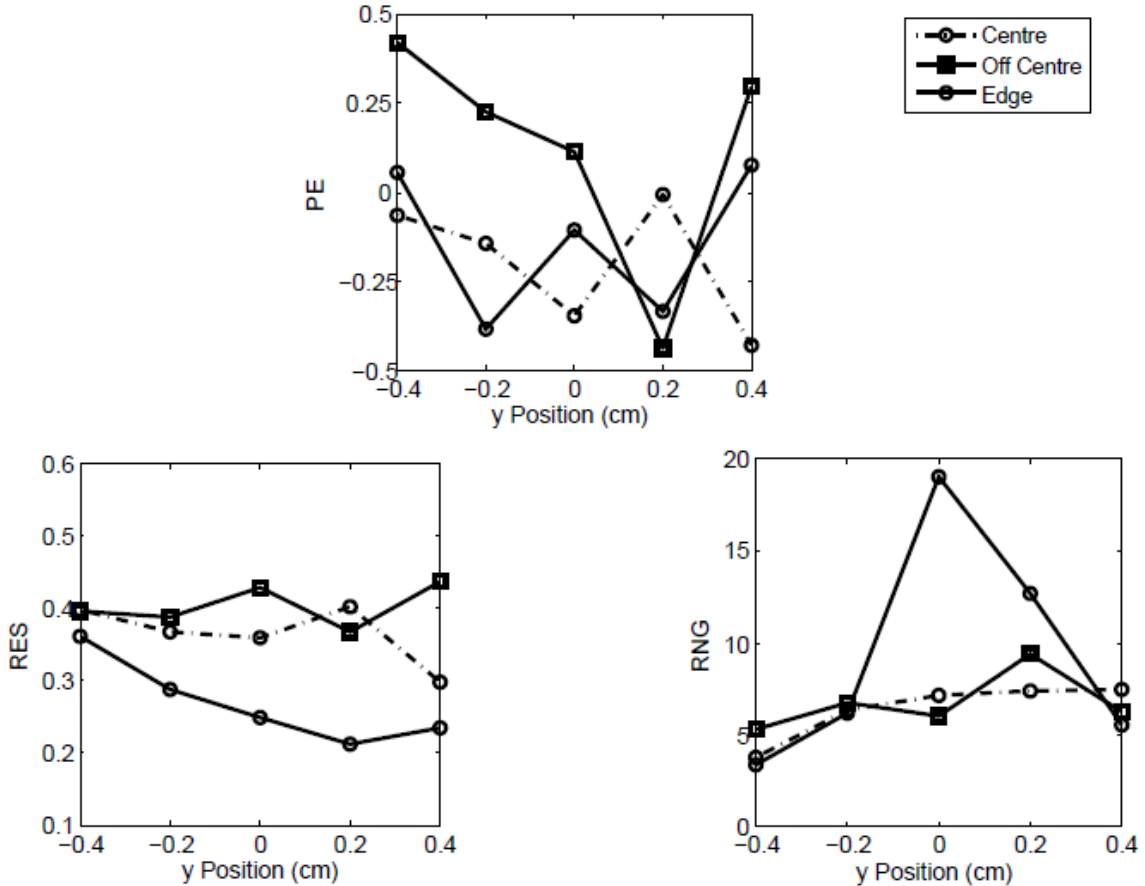


Figure 4.12: Performance metrics established for Sample #1.

Sample #2 as depicted in Figure 4.13, undergoing the same procedure, outperformed Sample #1 in terms of image quality. Based on visual inspection of the images, the stimulated area was tracked with reduced blurring and far less shape distortion. This is complemented by the overall low and more uniform RES values. However, added artifacts are also present in the majority of the images. This is most

pronounced in the first column of Figure 4.14, corresponding to the centre line, which may have been caused by an electrode disturbance during measurements. This is identified by the unusually high position error compared to the edge and offcentre lines, which exhibited very low position errors. Added shape deformation found at the points corresponding to the jumps in RES cause increased position errors as seen at $y=6$ of the edge line and $y=-3$ of the centre line in Figure 4.15. The off-centre line was found to have improved RES values at close proximity to the electrodes, similar to the relationship found using the saline setup, with its lowest values recorded at $y=6$ and $y=-6$ cm. Ringing was at its highest value along the off-centre line for the majority of the data points reaching a maximum of 7.98 and a minimum of 1.5 far lower than Sample #1. This is visually confirmed by the fact that negative conductivity changes are found to have far less contrast compared to Sample #1 (Figure 4.14).

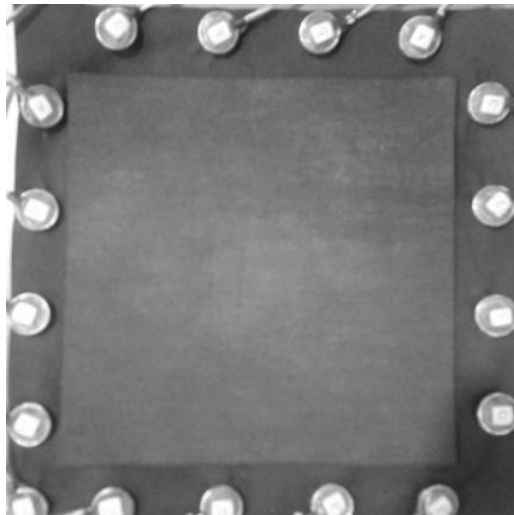


Figure 4.13: Sample #2 with both layers of non-woven fabric in stacked arrangement with circular pierced button electrodes mounted at the boundary.

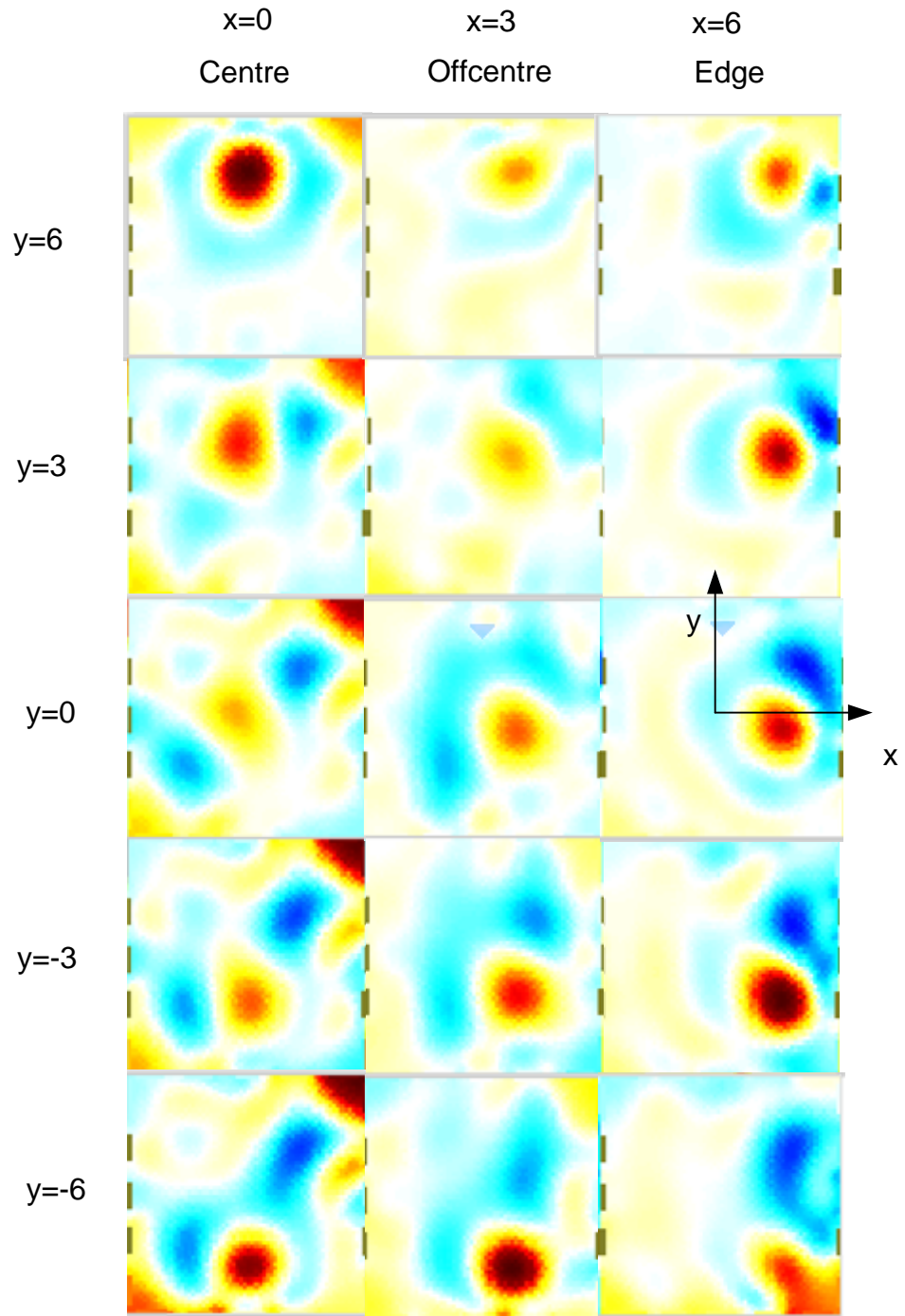


Figure 4.14: Pressure map for 15 stimulated locations conducted on Sample #2 where red regions depict positive increase in conductivity change and blue regions show a negative conductivity change .

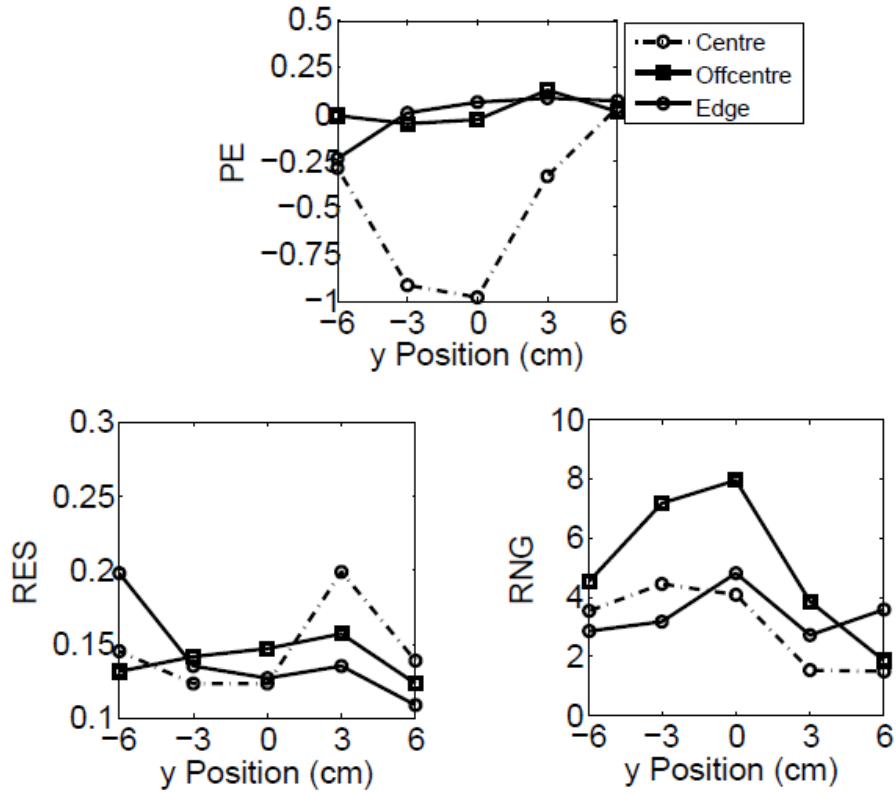


Figure 4.15: Performance metrics conducted on Sample #2.

4.2.3 Discussion and Summary

The implemented EIT pressure sensing scheme indicated potential in successfully depicting the pressure profile for both Sample #1 and #2. The sensor managed to reconstruct images that were repeatable based on the experimental trials.

4.2.3.1 Pressure Sensing Limitations

It was realized that the effective range of the transducer was much lower than anticipated. The preliminary experiments involving the voltage divider data acquisition method are found to be suitable for quick testing, but not as an accurate representation of the final

transducer. Given the larger phantom dimensions and boundary electrode setup, the EIT method managed to detect voltage changes for pressures up to 35 kPa and 65 kPa for Samples #1 and #2 respectively. These ranges are still considered effective for robotic applications. Sample #1 sensing limitation was impeded by its large hysteresis value (Figure 4.8(a)). Comparatively speaking, Sample #2 did present improved linearity and a lower but still significant level of hysteresis. This is mainly attributed to the material selection. The use of a tighter pre-specified ROI could limit the unwanted effect of the hysteresis and artifacts even further if the threshold is increased to a higher percentage.

4.2.3.2 Image Analysis

The performance metrics suggested certain relationships which were also present in the benchmarking experiment conducted using saline as the conductive medium. It was evident that given the current Finite Element Model without increased mesh density closer to the electrodes, greater shape deformations were found with closer proximity to the electrodes for both samples based on visual inspection of the images. This resulted in higher position errors due to the deformed shape of the stimulated area. This issue might be improved by having denser mesh areas closer to the electrodes to minimize this distortion effect. Negative conductivity changes, which can only be attributed to the reconstruction calculation, were also depicted for both samples. Despite their visual presence, they have no impact on the performance since they are filtered out when selecting the ROI.

A considerable cause of added position error in both samples, compared to the saline experiment, is probably due to the presence of image artifacts that have sufficient magnitude such that they are included within the ROI. This resulted in much more

amplified position error results. These artifacts are attributed to increased noise from the electrode-material interface as well as minor disturbances to the electrodes during data collection. Furthermore, in Sample #1, shape deformations were also experienced towards the centre as visualized in Figure 4.11. Here, previously stimulated areas remain present in consecutive measurements with lower amplitude. This caused the images to have a memory effect due to this sample's high hysteresis characteristic and resulted in added blurring, causing misinterpretation of the actual current pressure profile and making it harder for the actual stimulated area to be detected. This is confirmed by the higher and non-uniform RES values for both the centre and off-centre lines. Some of this position error may also be caused by the manual positioning method used for contact placement. In addition, different frequencies were used for each sample to improve the quality of raw voltage data, which was found to depend on the excitation frequency. However, this relationship was not investigated thoroughly, where the final frequency was selected based on experimental trials provided the three fixed available frequencies available through the SigmaTom II system. AC current was applied to avoid any electrolytic effect that would have degraded electrodes with time. Overall, the effect of image artifacts was found to be most dominant cause of image degradation, marginalizing the more minute correlation between resolution and electrode proximity that was highlighted in the saline experiment.

4.2.3.3 Sample Integration Considerations

The electrode mounting method is regarded as a critical factor to the quality of the acquired signals. Given the sensitivity of the EIT system to noise, the pressed mounting approach using the fixture, proved troublesome when acquiring data. This electrode

mounting method was found to be more susceptible to noise and relied on the extent the electrodes were preloaded using the fixture mounting screws as described in section 3.3. This is visually shown with the increased number of artifacts found in Sample #1. Therefore, it is suggested that piercing the electrodes as introduced in Sample #2 be the preferred method. This mounting method is also susceptible to minor electrode disturbances resulting in added artifacts but is found to produce improved images. Alternatively cold soldering techniques using silver epoxy can be used but may result in fragility and wear when used on such conformable surfaces.

Overall, the feasibility of using a conductive polymer and non-woven fabric as pressure sensing materials is demonstrated. The performance metrics used were capable of highlighting the effect image artifacts and shape distortion had on sensor output corresponding to position error and resolution. Additionally, hysteresis was found to be the dominant setback when using the stacked contact resistance approach as a transducer method.

Chapter 5

Stretchable EIT based Tactile Sensor

The aim here is to cover a complex geometric part such as a robotic joint using a single sensing element. Currently, tactile sensors lack high stretch capabilities due to the presence of wires within the sensing area for data acquisition purposes in typical taxel based designs. By including a stretchable piezoresistive element for the EIT phantom a single stretchable sensing solution is attempted. The following section will introduce the developed FEM formulation for complex surface EIT forward models. The approach is simulated in section 5.2. Subsequently, the stretchable woven fabric in Sample #3 is used to experimentally test the novel integration of EIT surface models and stretchable transducers for touch and pressure sensing applications. This is performed via stretching the sensor over a hemisphere shaped structure as described in section 5.3.

The integration of EIT based pressure sensing on complex geometric features is, theoretically speaking, achievable based on the fact that boundary electrodes are all that is needed for pressure profile depiction. The material selection and the implementation of a forward model, which will accurately represent the domain, are the two main challenges to this advancement in the sensors design. Therefore, to reconstruct images that accurately depict the pressure profile, it is vital that the EIT forward model be redefined to represent the geometry. There are typically two approaches to solving the EIT reconstruction problem via the EIDORS package. The first method is 2D EIT which restricts the discretized medium in a flat 2D plane with electrodes along the boundary.

Secondly, 3D EIT is implemented for volumetric applications where polyhedral elements are used with the possibility of multiple electrode layers in three dimensional space. Both approaches lack the necessary system matrix for solving the EIT problem for surface meshes in 3D space. It is therefore necessary to modify the system matrix to allow for surface modeling of complex geometries over which transducers can be stretched.

5.1 Surface Modeling and Linear Interpolator Derivation for Direct FEM Formulation

The Direct Method is the only FEM formulation method considered here. The addition of a third dimension to the vertices to account for surface modeling necessitates that the derivation of the linear interpolation function used for triangular elements be revised. Assuming that the electric potential varies linearly within the elements in the FEM, the formulation of FEM as described in [50] and [53] is presented. The piecewise linear and planar electric potential function within a triangle element defined by 3 nodes is given by

$$V(x, y) = c_1 + c_2x + c_3y. \quad (5.1)$$

Where c_1, c_2 and c_3 are the coefficients and x and y are nodal Cartesian coordinates. Assuming electric potential values V_1 , V_2 and V_3 at the three nodes, the potential function can be represented in matrix form by

$$\begin{bmatrix} V_1 \\ V_2 \\ V_3 \end{bmatrix} = \begin{bmatrix} 1 & x_1 & y_1 \\ 1 & x_2 & y_2 \\ 1 & x_3 & y_3 \end{bmatrix} \begin{bmatrix} c_1 \\ c_2 \\ c_3 \end{bmatrix}, \quad (5.2)$$

where the coefficient vector is calculated as follows:

$$\begin{bmatrix} c_1 \\ c_2 \\ c_3 \end{bmatrix} = \begin{bmatrix} 1 & x_1 & y_1 \\ 1 & x_2 & y_2 \\ 1 & x_3 & y_3 \end{bmatrix}^{-1} \begin{bmatrix} V_1 \\ V_2 \\ V_3 \end{bmatrix}. \quad (5.3)$$

The electric potential function can now be rewritten in the following form:

$$V(x, y) = [1 \quad x \quad y] \begin{bmatrix} 1 & x_1 & y_1 \\ 1 & x_2 & y_2 \\ 1 & x_3 & y_3 \end{bmatrix}^{-1} \begin{bmatrix} V_1 \\ V_2 \\ V_3 \end{bmatrix}. \quad (5.4)$$

The linear interpolation shape functions $f_i(x, y)$ for $(i=1, 2, 3)$ for the 2D mesh are denoted by

$$[f_1(x, y) \quad f_2(x, y) \quad f_3(x, y)] = [1 \quad x \quad y] \begin{bmatrix} 1 & x_1 & y_1 \\ 1 & x_2 & y_2 \\ 1 & x_3 & y_3 \end{bmatrix}^{-1}. \quad (5.5)$$

The elements of the local admittance matrix y_{ij} are calculated based on equation (2.3) as described in section 2.2.2 and is presented here via the partial derivatives of the shape functions as follows:

$$y_{ij} = \oint_{\Omega_e} \sigma_e \left(\frac{\partial f_i}{\partial x} \frac{\partial f_j}{\partial x} + \frac{\partial f_i}{\partial y} \frac{\partial f_j}{\partial y} \right) d\Omega_e, \quad (5.6)$$

where σ_e is the element conductivity and Ω_e is the domain of the conductive medium.

Given a constant conductivity within the triangular elements, the admittance matrix \mathbf{Y}_e and associated Electric Potential \mathbf{V}_e and Current \mathbf{I}_e vectors for the nodes are assembled in matrix form:

$$\begin{bmatrix} y_{11} & y_{12} & y_{13} \\ y_{21} & y_{22} & y_{23} \\ y_{31} & y_{32} & y_{33} \end{bmatrix} \begin{bmatrix} v_1 \\ v_2 \\ v_3 \end{bmatrix} = \begin{bmatrix} q_1 \\ q_2 \\ q_3 \end{bmatrix}, \quad \mathbf{Y}_e \mathbf{V}_e = \mathbf{I}_e. \quad (5.7)$$

To allow for non-planar surface modeling for our application, the shape functions introduced in (5.5) must be redefined to account for the third dimension. This is achieved by projecting the triangular elements, used for interpolation, from 3D space onto a normal plane while preserving their dimensions. This is graphically shown in Figure 5.1 and is performed on an element by element basis.

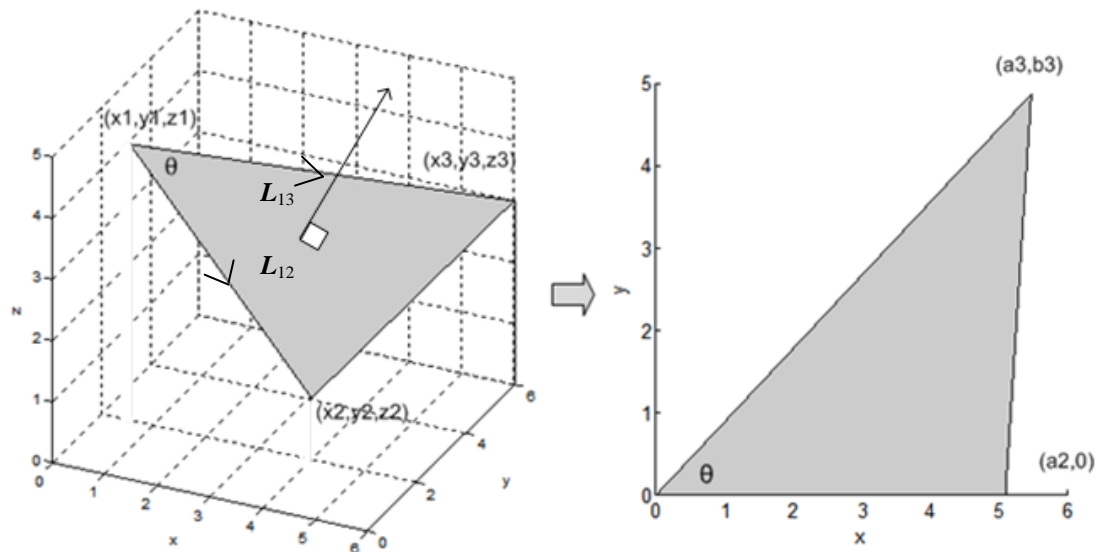


Figure 5.1: Projecting element from 3D to normal plane in 2D space.

Here, $\mathbf{L}_{ij} = \langle x_i - x_j, y_i - y_j, z_i - z_j \rangle$ is defined as a vector in three dimensional space found between the element vertices, with i, j giving the associated node number. It is used to establish the new coordinates of the triangular element such that the shape functions are given by

$$[f_1(x, y) \quad f_2(x, y) \quad f_3(x, y)] = [1 \quad x \quad y] \begin{bmatrix} 1 & 0 & 0 \\ 1 & a_2 & 0 \\ 1 & a_3 & b_3 \end{bmatrix}^{-1}, \quad (5.8)$$

where a_i and b_i for $(i=1,2,3)$ give the planar coordinates of the triangle after projection from 3D space onto a normal plane. They are denoted by

$$\begin{aligned} a_1 &= b_1 = b_2 = 0, \\ a_2 &= \|\mathbf{L}_{12}\|, \quad a_3 = \|\mathbf{L}_{13}\| \cos \theta, \quad b_3 = \|\mathbf{L}_{13}\| \sqrt{1 - (\cos \theta)^2}. \end{aligned} \quad (5.9)$$

The square matrix used in equation (5.8) is invertible, such that the shape functions are one at the specified vertex and zero at all other corresponding vertices as required to give the three assumed potentials V_i at the nodes. The partial derivatives of the linear shape functions are evaluated for substitution into equation (5.6) as follows:

$$\frac{\partial f_1}{\partial x} = \frac{1}{a_2}, \quad \frac{df_2}{\partial x} = \frac{1}{a_2}, \quad \frac{df_3}{\partial x} = 0. \quad (5.10)$$

$$\frac{\partial f_1}{\partial y} = \frac{a_3 - a_2}{a_2 b_3}, \quad \frac{df_2}{\partial y} = \frac{-a_3}{a_2 b_3}, \quad \frac{df_3}{\partial y} = \frac{1}{b_3}. \quad (5.11)$$

The local element admittance matrix in (5.7) is computed accordingly. The local matrices are then assembled into a global matrix through a transformation and the reconstruction problem is solved as described in Section 2.2.2.

The modified finite element linear interpolator, described above, will allow for the reconstruction of pressure profiles on complex surface models by taking into account the third dimension. This formulation is designed for the sole purpose of using triangular elements defined by 3 nodes for surface meshes. Once the surface mesh is acquired, point or complete electrode models are added which correspond to the constraints. With the

addition of the regularization method and stimulation pattern, the forward model can be effectively used for modeling complex geometric features that are typical in robotic applications. The implementation of the above was conducted in Matlab where the EIDORS ver.3.5 function (`aa_system_mat_fields`) was modified to establish a new system matrix as well as the (`show_fem`) graphics depiction function to incorporate the addition of surface mesh capabilities.

5.2 Simulated Pressure Distribution

To test the feasibility of the modified EIT algorithm, after the inclusion of the surface meshed discretization capability in EIDORS, a simulation of the pressure distribution is conducted. The purpose of the simulation is to check whether the reconstructed images of the conductivity distribution match the locations of stimulated regions. This simulation is performed to test the pressure distribution, not the pressure response over time, of the sensor. A discrete model, based on a surface mesh in three dimensions, is simulated for a hemispherical shape. No noise was added to the simulated data.

Implementation was performed by including a surface profile, which was created using a CAD program (Pro/E ver.4). The surface geometry was meshed using a FEM software package (ANSYS ICEM). The mesh was then read in Matlab where it was necessary to derive the connectivity matrix for the associated mesh. A Matlab function, integrated into the EIDORS platform, was created to read the standard Stereo Lithography (STL) file format and output a forward model as well as the node and connectivity matrices. Sixteen nodes were selected for point electrode placement along the boundary of the hemisphere in an equidistant manner without introducing additional

mesh refinement at the specified electrode locations. The forward model was composed with an adjacent stimulation and measurement pattern.

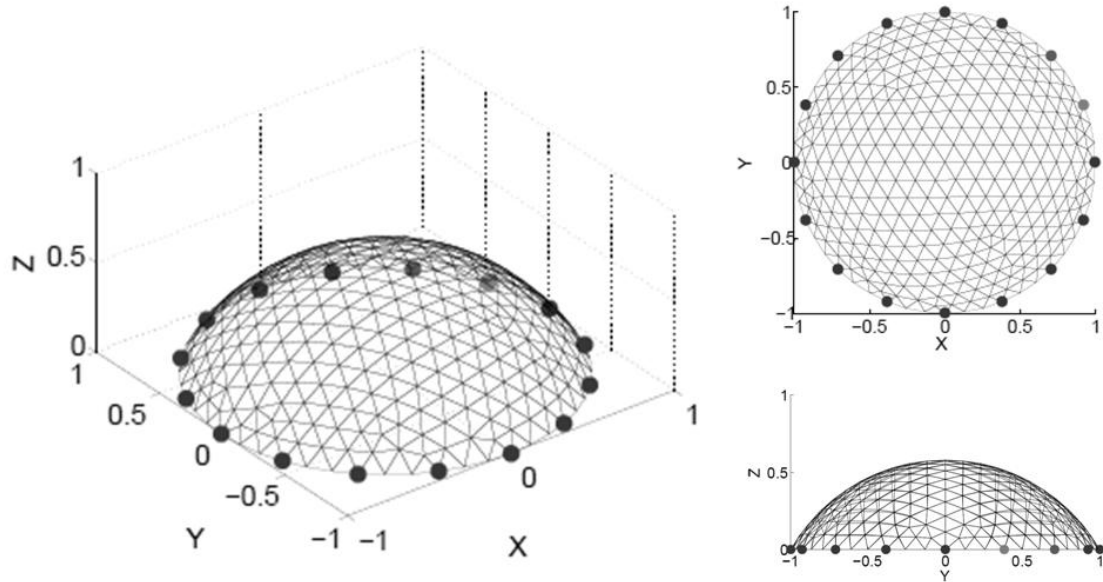


Figure 5.2: Mesh composed of 624 elements and 337 nodes used for complex geometry modelling with point electrodes equidistantly placed along the boundary.

The viability of the approach is achieved in simulation through the following steps:

1. A constant homogenous conductivity value is set for all the elements in the phantom. An adjacent current stimulation pattern is specified along with the conductivity distribution to solve the forward problem. This yields the electric potential at nodal points. The electric potential at the electrode nodes are then used to define the voltage vector for the homogenous phantom.
2. The conductivity values of elements at visually selected locations in the phantom are set to twice the surrounding element values. The remaining elements in the phantom are specified with a constant homogenous conductivity value. The

forward problem is then solved and the voltage vector for the non-homogenous phantom, which represents the sensors image after pressure is applied, is acquired.

3. Voltage vectors from Steps 1 and 2 are then used to solve the inverse problem via difference imaging. Given the simulated electric potential of the electrode nodes and the same adjacent stimulation pattern, the change in conductivity of the elements are calculated.
4. The simulated conductivity distribution is visualized on the hemisphere shaped surface mesh where red regions show positive changes in the conductivity.

Desired reconstructed images should show areas of increased conductivity at the pre-specified locations, establishing that solving the FEM yields the correct pressure profile. This is precisely what the model has demonstrated in the following cases:

- *Case 1:* The stimulated elements are selected for three different locations. The response to one point of contact, over the active area of the sensor, is being investigated here. Figure 5.3 (a-c) depict the reconstructed images for the three scenarios. It is shown that the reconstructed conductivity/pressure profile match that of the stimulated area for all three locations.

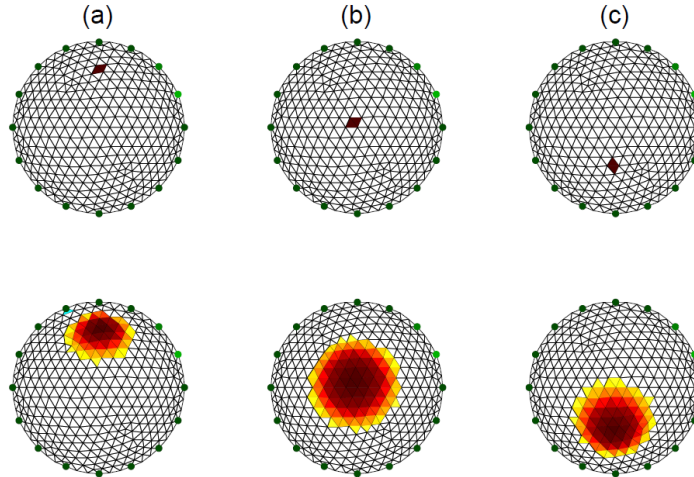


Figure 5.3: (Top) Stimulated elements, (Bottom) Reconstructed images where red regions depict an increase in conductivity corresponding to pressure.

- *Case 2*: Multipoint contact is investigated by altering the conductivity of two separate regions at arbitrary locations of the phantom. Two and three point contact is simulated and the associated reconstructed images are shown in Figure 5.4. There is a clear blurring of the stimulated region which is typical in EIT solver output given the nature of the problem. However, the FEM is successful in showing the conductivity profile of the phantom given the surface mesh model for the hemisphere shaped geometry.

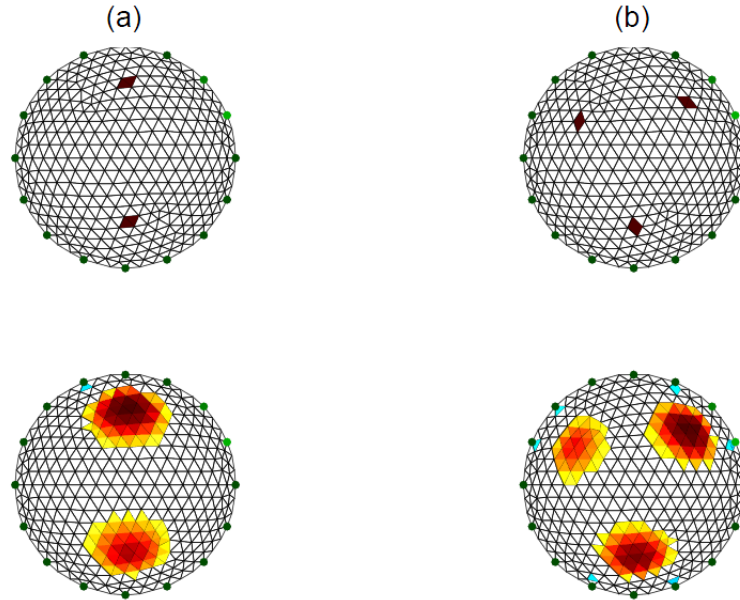


Figure 5.4. Two point and three point contact using surface mesh (top view) where red regions depict positive changes in conductivity.

To conclude, the aforementioned preliminary simulation studies of the surface modeling scheme for EIT based pressure sensing were successful. The change in conductivity, given voltage measurements from the boundary electrodes, was realized using the FEM presented in Section 5.1.

5.3 Stretchable EIT Sensor Development

5.3.1 Stretchable Transducer

The validation of the surface modeling approach introduced is complemented with experimental trials. To cover complex geometric features using conductive medium we require a stretchable piezoresistive transducer. The approach followed here uses both a single and dual stacked layer arrangement composed of two different stretchable fabrics

without the need of a wire mesh or isolated conductive fabric stitched in an array like arrangement. Contrary to the layers used in Sample #1 and #2, a single layer of the stretchable fabric used in Sample #3 is woven, demonstrating in itself piezoresistive properties. This was noted during preliminary EIT testing and is explained by the fact that contact resistance between the woven stretchable threads manages to successfully exhibit stress excited resistance change properties in a more compact arrangement.

Dual layer implementation is also considered as an attempt to have more pronounced conductivity changes for improved sensitivity. It has been realized experimentally that if the second layer has a resistance that is too low, the SigmaTom II EIT system fails to detect increases in conductivity, based on an initial reference frame, acquired at no load. The fabrics listed in Table 5.1 were tested during preliminary runs with Silver coated bus material used as the second layer. These combinations did not exhibit a resistance change that was detectable by the EIT system.

Table 5.1: Materials tested with SMP bus material.

	Mfg	Primary Element		
		Material	Surface Resistance (kΩ/sq) as provided by Mfg	Thickness (mm)
1	Eonyx	LTT-PI-A-250	0.200	0.3
2	Eonyx	LG-PI-A	0.17	0.3
3	Eonyx	LR-SL-PA	6-10	0.2

The stack is comprised of stitching the two fabric layers materials with electrodes mounted on the bottom layer to avoid creasing and added looseness which would have a negative impact on its pressure detection ability. A stretchable nonconductive thread is used to attach the two layers together. The materials in Sample #3 are selected based on their surface resistance. They are made of a nylon-spandex blend and are capable of 220% stretch in any direction (Table 5.2). Given the high flexibility of the fabric no minimum bend radius is identified by the manufacturer.

Table 5.2: Sample #3 properties.

	Mfg	Layer 1			Layer 2		
		Material	Surface Resistance kΩ/sq	Thickness (mm)	Material	Surface Resistance kΩ/sq	Thickness (mm)
Sample #3	Eeoynx	LG-PI-A Woven	0.17	0.3	LGSLPA Woven	1	0.3

5.3.2 Apparatus

The experimental apparatus is composed of the solid hemisphere part to be covered, the transducer element with mounted electrodes, and the EIT system. The surface used for mesh creation in the previous section is used to create a part in CAD software (ProE ver.4) which was then 3D printed on high density fiberboard. This allowed for an insulated base feature with the necessary degree of hardness to withstand the load range being applied of up to 100 kPA without deformation. The sensing element was cut to size with a $\phi = 210$ mm and boundary electrodes measuring $\phi = 11$ mm. The transducer was placed in a circular quilt fixture with additional nonconductive fabric stitched to the

boundary, which was used to hold the element in place without applying pressure to sensing area (Figure 5.5). A load cell (MLP-25) mounted between two plates was used to acquire load data based on which pressure readings were calculated.



Figure 5.5: (left) Sample 3 on a planar surface, (right) stretched over hemisphere shaped part matching the mesh found in the forward model.

5.3.3 Procedure and Configuration

5.3.3.1 Planar Case

The stretchable element is initially tested on a flat planar surface. The static loading and feature recognition experiments explained below are repeated for a single and dual layer transducer element design. While a single layer is used for the position tracking experiment as it is assumed that stacking will not have an impact on position error.

- *Static Loading Experiment* : The stretchable EIT sensor undergoes a loading trial where pressure is incremented until the resistance change saturates. Pressure is then decremented back to initial conditions. Contact is established using a square

insulated cube measuring 4 cm^2 placed at the centre where a load cell (MLP-25) is used for force measurement. The sensors calibration curve, effective span and hysteresis curves are all obtained from the results acquired. This procedure is repeated three times to identify whether the sensor readout is stable and sufficiently repeatable.

- *Feature Recognition Experiment:* A pressure map validation is conducted using two different shapes placed at the center of the conductive fabric. The aim of which is to demonstrate the ability of the sensing setup to identify sharp edges and gaps within the pressure profile.
- *Point Contact Tracking Experiment:* The ability to detect pressure single point contact is tested. A 4 cm^2 insulated cube is manually placed at 3 different locations across the diameter (x axis) of the phantom under a fixed 2 kg load in order to quantify the position error.

The general approach explained in Chapter 3 is followed here in regard to EIT Difference Imaging. However, the development of a new circular shaped phantom dictated that the forward model used in the design be revised. A circular 2D common model obtained from the EIDORS software package is implemented here with a 16 point electrode configuration to coincide with the planar setup (Figure 5.6). The mesh includes a total of 1201 nodes and 2304 elements.

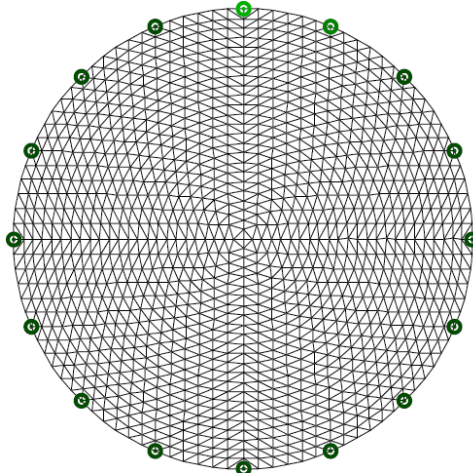


Figure 5.6: Forward model mesh composed of 2304 elements and 1201 nodes with electrode nodes highlighted in green for stretchable EIT sensor planar case.

5.3.3.2 *Complex Geometric Feature Case*

Sample # 3 is pinned via its fixture to cover the hemisphere shaped part to investigate its performance under stretch and to test the associated system matrix developed in section 5.1. The experiment involves applying pressure manually through touch to demonstrate the ability to detect multi-touch stimuli. Single point contact is initially conducted prior to multi-touch for up to 3 point contact at different locations. The image reconstruction is performed using the surface modeling method explained in Section 5.1. The z coordinate is then eliminated and image reconstruction is performed using a planar model to allow for a comparison of both methods.

5.4 Results

5.4.1 Planar Case: Static Loading Experiment

The hysteresis cycle plot is shown in Figure 5.7 for a single layer of stretchable fabric. The sensor is characterized with good linearity when undergoing loading. A maximum applicable range of 20 kPa is defined in preliminary trials. The absolute value of the voltage data acquired is used to calculate the relative change in conductivity and is displayed as raw data in Figure 5.7 as well. The single layer of conductive fabric does experience a reduction in corresponding admittance when the load is being decremented but with a significant hysteresis value of 41 % as a mean value for three trials. However, based on the three conducted trials the repeatability of the results in terms of pressure sensing ability is rather poor. The repeatability is calculated as the maximum difference for each recorded pressure reading when approached from the same direction. Both loading and unloading curves are considered in the repeatability calculation which is found to reach 26% of rated output.

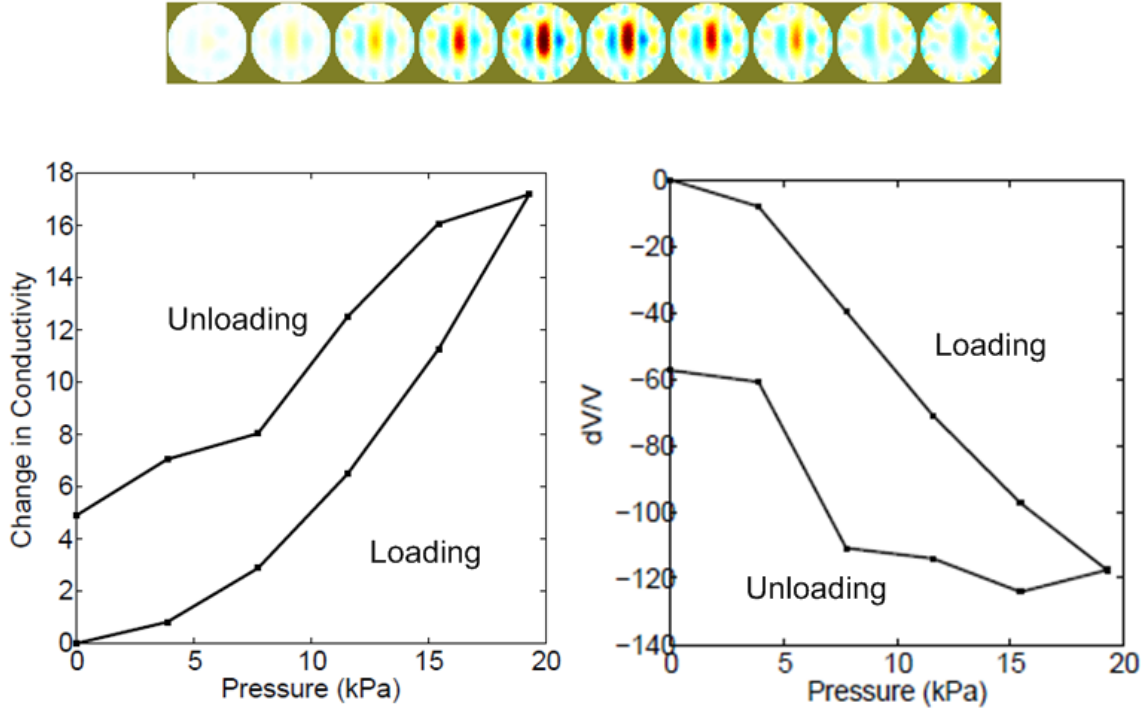


Figure 5.7: Hysteresis curve based on 25% ROI (left) and corresponding raw data (right) for single layer of conductive fabric.

Using a stacked setup with both layers enhanced the pressure sensing span to 65 kPa. During loading in the upward direction the sensor experienced a highly linear characteristic which is clear from both the raw data and the image based pressure readings. However, the sensor does not follow a similar return curve. The relative conductivity change remains steady at a value close to the maximum conductivity change with a reduction of only 16 % of the rated output until the no load initial condition is reached. Only then does the relative conductivity reading jump to a much lower value. The hysteresis is found to be higher than using the single layer setup by 6 %. However, the repeatability of the sensor is dramatically improved to 11.17% of the rated output.

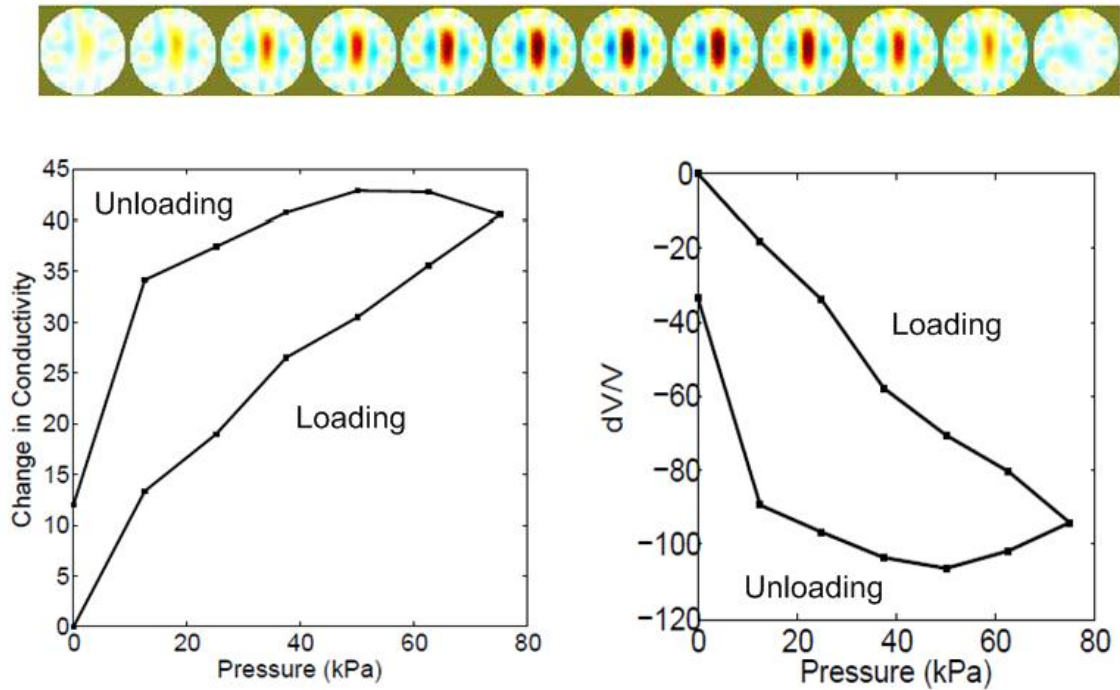


Figure 5.8: Hysteresis curve based on 25% ROI threshold (left) and corresponding raw data (right) for dual layer stacked setup of conductive fabric.

The position error for the dual layer setup is found to be comparable to the single layer arrangement with the y direction having a larger mean error value of 15% and 14% of sensor diameter respectively. The centroid position error readings were found to be almost negligible as shown in Table 5.1 in the x Cartesian direction for both cases with a slightly higher value of 3.8% for the single layer sensor. However, it is clear for the standard deviation metrics that the centroid is found with high precision for both cases in both the x and y directions.

Table 5.3: Sensor characterization parameters.

Sample3	Range (kPa)	Mean Hysteresis (% of R.O)	Normalized CoPx Error (33 Trials)		Normalized CoPy Error (33 Trials)		Repeatability (% of R.O)
			Mean	SD	Mean	SD	
Single layer	20	41.0	0.0379	0.0465	0.1574	0.0887	26.96
Dual layer	65	47.0	-0.0261	0.1025	0.1409	0.0638	11.17

5.4.2 Planar Case: Feature Recognition Experiment

Two shapes were used to test the effectiveness of the sensor in depicting an actual stimulated profile. A fixed 25 N load was used for both cases to compress the shape onto the active sensor area. With the ‘L’ shape providing sharp corners and the ‘O’ used to test whether gaps can be identified. The silhouette of both the ‘L’ and ‘O’ shapes can be identified under the single layer case but with limited clarity (Figure 5.9(b)). However, it is still possible to identify corners and the gap found in the ‘O’ shape, but with very low amplitude. The dual layered setup demonstrated a higher amplitude response in comparison, with the corners found in the ‘L’ shape clearly identifiable as shown in Figure 5.9(c). Furthermore, the donut shaped stimulus was not simply depicted as a single large blurred object but it is clear that the center of the object has not exhibited a positive increase in relative admittance.

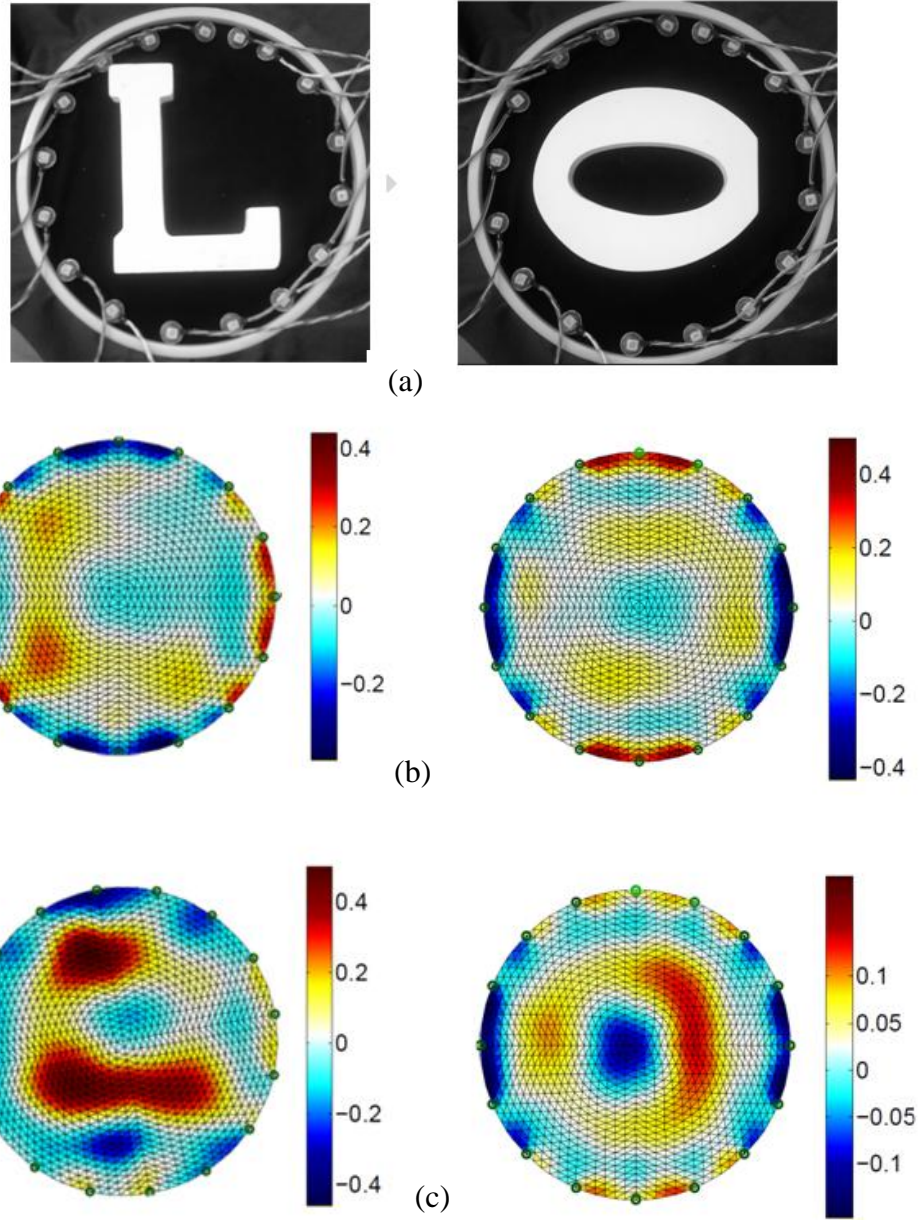


Figure 5.9: (a) Actual pressed shapes. (b) Pressure profile for single layer. (b) Dual layer setup for two different shapes in (mS/sq).

5.4.3 Planar Case: Point Contact Tracking Experiment

The position errors for four locations, at a constant radial distance of the circular shaped phantom, in addition to the centre were stimulated using a constant pressure as described

in section 5.3.3. Table 5.4 shows the normalized position error for the different locations. A maximum value of 19% is found towards the bottom of the phantom where a mean value of the position error of all the positions is found to be 9.3%. The standard deviation of the three trials for each individual location is found to be rather low with a maximum of 0.03.

Table 5.4: Position Error for woven fabric on planar surface at 4 different locations.

Coordinate (x,y) cm	Normalized Position Error (3 trials)	
	Mean	SD
(0,0) Centre	-0.05	0.015
(0,5) Top	0.07	0.004
(-5,0) Bottom	0.19	0.017
(5,0) Left	0.05	0.006
(0,5) Right	0.11	0.030

5.4.4 Complex Geometric Surface Case Experiment

The ability of the stretched sensor to identify single point contact at different location is shown in Figure 5.10. Contact is established by touching the surface using the index finger. The surface modeling method is used here where a top view of resulting images are depicted. Four different locations that are opposite to one another are stimulated by touching the stretched sample. The corresponding images exhibited a blurring effect and artifacts that are visible along the boundary. The presence of artifacts in the central active area is of lower amplitude compared to the stimulated regions introducing interference

that degrades performance but not to the extent that the actual stimulated regions are indecipherable. Thus the images provide sufficient functionality in identifying the point of contact based on visual inspection.

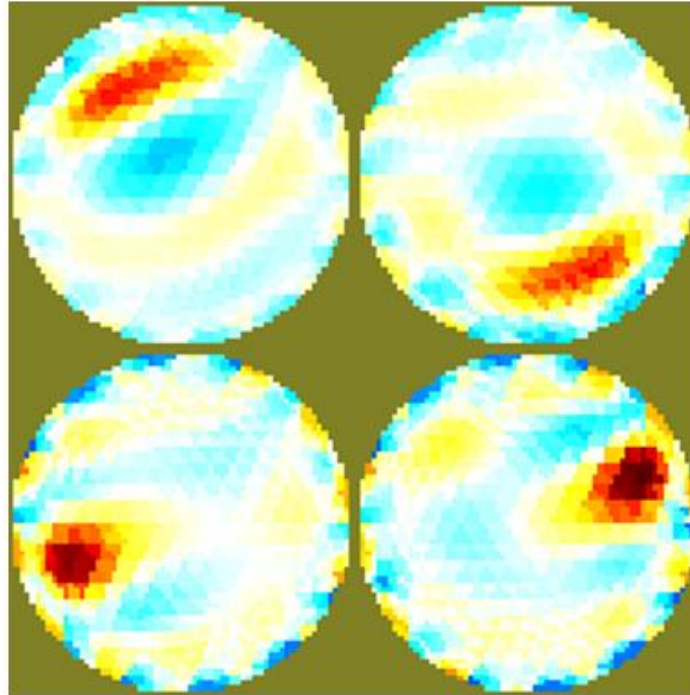


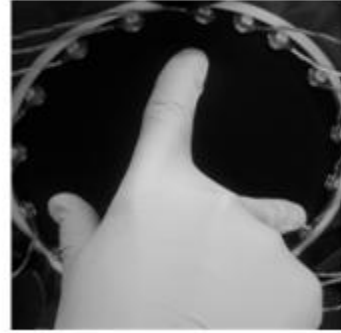
Figure 5.10: Single point contact with sensor stretched over hemisphere shaped part with red regions depicting positive increase in admittance.

The feasibility of multi-point contact is established, over curved surfaces, using a single layer of the stretchable conductive fabric for the surface meshed model. Two and three point contact is demonstrated in Figure 5.11. Ringing is present around the stimulated regions but there are minimal artifacts with positive admittance change included in the active area. However, there are artifacts with positive amplitude present along the boundary as found earlier in the planar case. The surface model used does not correspond identically to the planar model when projected on a flat plane. It is clear that

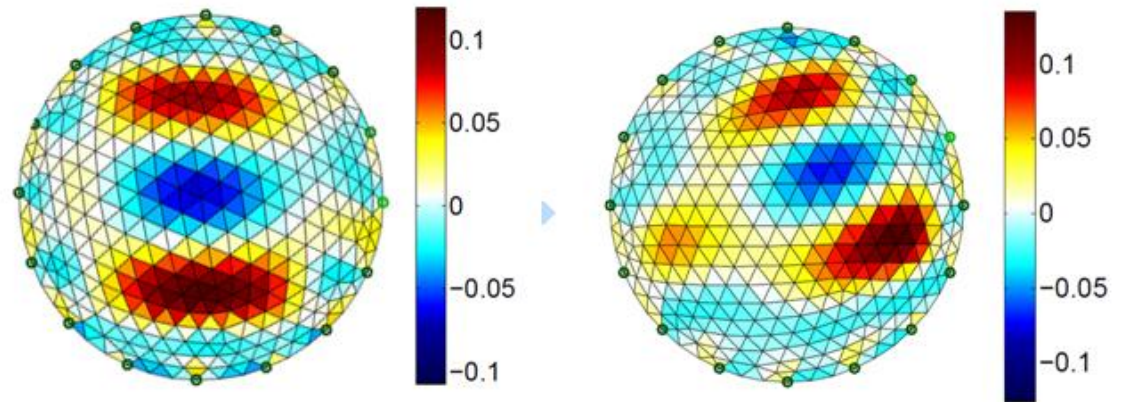
the size of the stimulated area is larger and the location has been altered. This indicates that by adhering to true surface model rather than a flat planar 2D model, image reconstruction provides a more realistic representation of the medium under investigation.

Table 5.5: EIT system parameters for stretchable fabric.

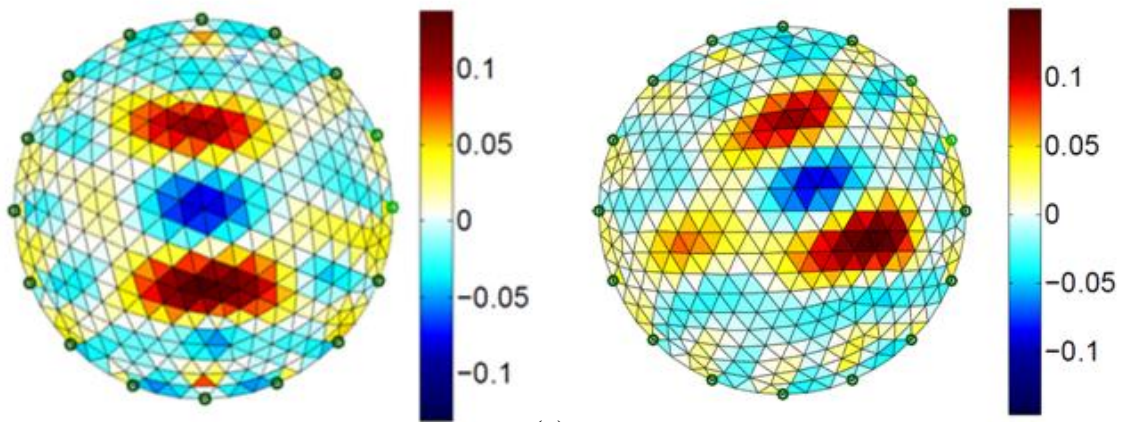
	Sample #3
Frequency (kHz)	50
Gain	4
Amplitude (%)	45-50
Attenuators	N/A
Frame Rate	4.73
Regularization Method	Laplacian
Data Type	Absolute
Hyperparameter	0.15



(a)



(b)



(c)

Figure 5.11: (a) Actual two and three point contact admittance change with sensor stretched over hemisphere (b) Reconstructed images using surface model in (mS/sq) (c) Reconstructed images using 2D planar model in (mS/sq).

5.5 Discussion

EIT sensing characteristics were investigated for stretchable fabric in a single and dual stacked setup for the planar case. The data highlights that the fabric is capable of admittance change when compressed and the EIT system and reconstruction model has demonstrated effectiveness in detecting the relative change in voltage and admittance through post-processing of the raw data.

5.5.1 Pressure Sensing Limitation

The materials used based on the contact resistance transducer, act as the bottleneck of the design. Pressure response is observed to have improved linearity when using woven fabric compared to the conductive polymer and non-woven fabric used in Samples #1 and #2. However, the unloading return curve demonstrated sporadic admittance change. This resulted in poor hysteresis and repeatability values for both single and dual layer setups. It is hypothesized that there are residual stresses in the fabric post loading, which are not released in a timely manner, hence causing the degraded performance. Furthermore, once a no load condition is reached the fabric does experience a significant return to an admittance value that is comparable to the initial acquired reference value but with an added value of 28% of the rated output span, for both material arrangements. Therefore, single and stacked dual layer woven fabric cannot technically be considered as pressure sensors without the addition of more complex fabrication methods. Alirezaei et al, [46] managed to implement such a sensor using a conductive yarn wire mesh and stretchable fabric base in a stacked 4-layer arrangement which claims stretch insensitivity

with a highly nonlinear response but with high repeatability and minimal hysteresis, despite the lack of a published quantifiable assessment.

5.5.2 Touch Sensing Capability

The established setup in our case does show potential as a touch sensor. This is validated by observing the repeatable position error. The 10% error in the y direction found in static loading experiment can be contributed to added shape deformation, but mostly due to the presence of artifacts with positive conductivity values and possibly due to mismatch between the model and the physical electrode positions. This is confirmed in the planar position tracking experiment where the mean position error value, based on 5 different locations was found to be 9.3%. More importantly, the position error data set had very low standard deviation values, demonstrating that the position of the stimulated area can be identified with a good degree of precision. In addition, the pressure profile is also demonstrated with sufficient clarity to identify complex shapes. This recognition ability, to our knowledge, has not been achieved in any prior publications. Blurring is present in the reconstructed images but the silhouette of the corners and gaps within the stimulated region are clearly identified and not depicted as single or multiple blurred regions. This indicates that EIT tactile sensing is capable of pressure profile depiction in addition to point contact location detection that can be used for complex feature recognition.

5.5.3 Complex Geometric Surface Coverage

The woven fabric under a constant amount of stretch is successful in maintaining its pressure profile capabilities for multi-touch sensing. It is emphasized that the reference

frame collected at no load is reacquired after the fabric is stretched over the hemisphere part. It is also recommended that once stretched the fabric is not to be used further under different conditions since the fabric will not return to its original form and will exhibit unpredictable degraded performance. Two and three point contact is verified for the sample used and the associated EIT setup. The smoothness of the amplitude decay around the stimulated area might require the addition of image processing algorithms using adaptive filtering techniques to isolate the regions of interest for an alternative ROI selection criterion.

The surface modeling method is practically validated using experimental data in the complex surface case. The comparison with an identical mesh that is projected onto a plane was shown in Figure 5.11. Visual inspection of both outputs shows a larger associated ROI for the more accurate surface modeling method. The 2D reconstruction found in the literature entails tainted positions and relative admittance change regions that are altered in terms of the stimulated areas size aspect ratio. To conclude, two and three point multipoint contact are validated using the surface meshed forward model. Images are found to be unequivocally different to the 2D planar model commonly found in the literature for EIT sensing.

Chapter 6

Conclusions and Future Work

Significant steps were achieved in realizing the goal of an EIT based tactile pressure sensor capable of high flexibility without the presence of wires in the active area of the sensor. The non-taxel based design was accomplished using 2D models. Furthermore, covering complex geometric parts using a single stretchable sensing element with electrodes limited to the boundary was implemented through the introduction of a novel surface meshed model for EIT image reconstruction.

6.1 Conclusion

A Difference Imaging reconstruction approach was implemented via a regularized one-step solver for sensor development. An ROI was then established based on the output images and the mean value of the selected ROI elements were used to calculate the pressure output reading. The data processing stage, along with the SigmaTom II hardware platform, was tested using a homogenous saline solution with electrodes submerged for consistent contact as an initial phantom to benchmark the algorithms performance. It was verified that the EIT system did not contribute to exaggerated hysteresis values and was found to give repeatable results. In addition, it was practically demonstrated that resolution was correlated to the proximity of the stimulated area to the boundary electrodes and position errors were mainly attributed to the presence of image artifacts.

The EIT pressure sensing was implemented via three different samples; conductive polymer and both woven and non-woven fabrics. The material selection was based on their use as a robotic artificial skin interface. The sensor setup and associated configuration parameters were presented. Sensor characterization was conducted through a series of static compression tests. The following was realized based on material testing:

- The PSCR used in Sample #1 only exhibited resistance change when in a stacked arrangement based on the contact resistance phenomena. The contact resistance based, stacked transducer approach, exhibited a nonlinear relationship between pressure and relative change in conductivity for all the samples.
- The non-woven fabric used in Sample #2 was found to be the most effective with the lowest recorded hysteresis and largest effective span.
- Despite the woven fabric used in Sample #3 having the most linear performance during loading, it did not provide sufficient repeatability due to unpredictable results acquired during unloading. This is attributed to the presence of residual stresses thus limiting its use only as a touch sensor.

Overall, large hysteresis values attributed to material selection and the stacked element fabrication method were found to be the main impediment to the design. In addition, image artifacts were identified as the dominant cause of reduced position accuracy. The electrode mounting scheme in itself was also found to have a large impact on acquired signals with press mount electrodes providing difficulties in reliable data collection. A summary of the static assessment of sensor performance is shown in Table 6.1.

Table 6.1: Summary of planar pressure sensor static assessment results.

Sample	Range (kPa)	Hysteresis (% of R.O)	P.E (Max of x,y)	Sensing Application	Material Characteristics
1	35	34.50	0.046	Pressure	Flexible
2	65	20.03	0.032	Pressure	Flexible
3-Single layer	20	41	0.157	Touch	4 way stretch up to 220%
3-Dual layer	65	47	0.141	Touch	4 way stretch up to 220%

A stretchable EIT sensor for covering complex geometric features was simulated and experimentally validated using the introduced surface modeling method. Results were different to the common 2D planar model used for EIT reconstruction approach which does not fully capture the actual geometry. Furthermore, multi-touch and effective pressure profile reconstruction that depicted edges and gaps within the profile was demonstrated using woven fabric which indicates effectiveness as a touch sensor

6.2 Recommendations and Future Works

EIT based pressure sensing has demonstrated considerable potential for integration as an artificial skin for robotic application. Depending on the material used for the sensing element pressure acquisition can be achieved or restriction to touch sensing might be necessary due to limited pressure sensing repeatability and effective span. Therefore, it is suggested that following material selection based on surface resistance compatibility, further research can be conducted on both the hardware and software aspects:

Hardware:

- i. Identifying fabrication techniques that can provide transducer elements with improved hysteresis. Possible use of the artificial-hollow-fiber structure fabricated via metal deposition during sputtering as described in [30] may enhance effective range, hysteresis and linearity in a woven transducer design.
- ii. The electrode mount interface is another topic that might require added investigation where different mounting schemes can be compared such as cold soldering and piercing using different conductors and their impact on data quality.

Software:

- i. There are several hyperparameter selection criteria introduced in the literature, the implementation of which might yield further improvements in reconstructing the pressure profile along with alternative stimulation and measurement patterns.
- ii. Once sufficient repeatability and robustness is achieved, the integration of a Preisach Neural Network based hysteresis compensator might overcome some of the limitations provided by the hardware. Such compensators have been found effective in real time actuators and so their adoption in the EIT pressure sensing scenario might prove as a rewarding research direction.

Appendix

Script used for sensor implementation and analysis:

```
%%%%%%%% Load data from pressure test and plot calibration curve%%%%%%%%  
%%%%%%%%%
```

```
function [h,m,R,copx,copy]=calibrate(P);  
% Frame naming convention use 'a' followed by number in consecutive order  
% P are the corresponding pressure readings for each frame  
% Function outputs:  
% m is fractional change in voltage data  
% R is mean value of ROI  
% center of pressure in x and y location  
% h hysteresis  
close all  
clear all  
clc  
run eidors3.5/eidors/startup.m  
vh=load('sample3p\|a0.mat');%select data frame numbering a0 being refernce  
vh=cell2mat(vh.Eit_Data);  
vh=vh(:,1:20);% 20 frames per measurement  
%R=size(50,1);  
%cop=size(50,2);  
P=linspace(1,3,3);  
[~,c]=size(P);%select data  
m=[];
```

```
%%%Input Model  
%imdl=sqmesh(2000);  
imdl=mk_common_model('f2c',16);  
% [imdl,e,n]=nodestl('mesh.stl');% surface model  
%imdl.fwd_model.nodes=imdl.fwd_model.nodes(:,1:2);  
%imdl.RtR_prior='noser_image_prior';
```

```
%% SigmaTom II data reorganization %%  
imdl = A_filter_protocol(imdl);
```

```
for k = 1:c;  
file = sprintf('sample3p\|a%d.mat',k);%select data  
data = load(file);  
vi=cell2mat(data.Eit_Data);  
vi=vi(:,1:20);
```

```

[imgav]=calc_inverse(vh,vi,imdl);
% main function that gives COP and Conductivity mean value
[qmi,img,R1,x,y,X,Y]=roi(imgav,0.25);
[vm]=calc_frac_volt(vi,vh,imdl);
m=[m,vm];
R(k)=R1;
imagav(k)=imgav;
copx(k)=x;
copy(k)=y;

%plot for testing
figure,show_fem(imgav,[1])
hold on
plot(X,Y,'+g')

end
%hysteresis calculation
h=max(fliplr(R(1,(numel(P)+1)/2:numel(P))))-R(1,1:(numel(P)+1)/2)...
/(max(R)-min(R))
%% Plotting figures and labelling%%
figure

for c=1:numel(P)
%imagav(c).fwd_model.nodes=imagav(c).fwd_model.nodes(:,1:2);
imagav(c).show_slices.img_cols = numel(P);
imagav(c).show_slices.sep = 2;
end
show_slices(imagav)

figure
plot(P,R,'-ks','LineWidth',2,...
'MarkerEdgeColor','k',...
'MarkerFaceColor','w',...
'MarkerSize',2);
xlabel('Pressure (kPa)')
ylabel('Change in Conductivity')
%set(gca,'XTick',0:2:22)
axis square
%set(gcf,'Paperposition',[.25 2.5 7 7])
%print -dpdf saline2hyst.pdf ; system('start saline2hyst.pdf')

figure
subplot(211), plot(copx,'o','MarkerEdgeColor','k'),
xlabel('Measurement Index'),set(gca,'XTick',1:1:20)
set(gca,'XTickLabel',[])
ylabel('CoP X (cm)')

```

```

%axis([0 20 -0.1 0.1])
subplot(212), plot(copy,'x','MarkerEdgeColor','k')...
    , xlabel('Measurement Index'),set(gca,'XTick',1:1:20)
ylabel('CoP Y (cm)')
%axis([0 20 -0.1 0.1])
%Plotting mean voltage
figure
plot(P,m,'-ks','LineWidth',2,...
    'MarkerEdgeColor','k',...
    'MarkerFaceColor','w',...
    'MarkerSize',2);
ylabel('dV/V');
xlabel('Pressure (kPa)');axis square
% animate_reconstructions('lg',imagav);

function imgav =calc_inverse(vh,vi,imdl)
% Set Parameters
imdl.hyperparameter.value =0.15;
%0.0326 for rubber sample;
imdl.fwd_model.normalize_measurements = 1;

% Obtain FILTERED JACOBIAN / Protocol
imdl = A_filter_protocol(imdl);
vh=mean(vh,2);
vi=mean(vi,2);
vh=abs(vh);
vi=abs(vi);
imgav = inv_solve(imdl, vh, vi);
%imgav(ii).elem_data(imgav(ii).elem_data>0)=0;
end

function [vm] = calc_frac_volt(vi,vh,imdl )
% Voltage measurment fractional change performance metric
% vi and vh are data acquired from SigmaTom II
IDX = [18:2:416,2:2:16];
vh=abs(vh);vi=abs(vi);
vh= vh(IDX,:);
vi= vi(IDX,:);
dv=calc_difference_data( mean(vh,2), mean(vi,2), imdl.fwd_model);
vm=mean(dv);

end

```

```

function [v,img,R,copx,copy,X,Y]=roi(imgs,amp_set);
%% Mostly referenced from eval_Greit_figofmerit function%%
%% Gives the roi centroid locations and mean value%%
imgs.fwd_model.nodes=imgs.fwd_model.nodes(:,1:2);
mdl=imgs.fwd_model;
elem=imgs.elem_data;
% [i,j] = find(elem==min(elem(elem>0)));
% m=elem(i,j);
% imgs.elem_data=(imgs.elem_data-min(elem))/(mean(elem));%normalizing image
imgs = calc_slices(imgs);
map = ~isnan(imgs); %assume all imgs are the same shape
imgs(isnan(imgs)) = 0;%64*64 image with actual values
sz=size(imgs,1);
qmi = calc_hm_set( imgs, amp_set );%64*64 ones where value is 1/4 or above
% remove negative from imgs for conductive changes
%qmi = qmi.*map;
img = imgs.*qmi;%selected set given actual values
[r,c,v]=find(img);%v is vector of conductivity values
bnd = unique(mdl.boundary);
bb_min = min(mdl.nodes(bnd,:));
bb_max = max(mdl.nodes(bnd,:));

[x,y]=meshgrid(linspace(bb_min(1),bb_max(1),sz),...
    linspace(bb_max(2),bb_min(2),sz));
%max and min switched for y
ss_qmi = sum(img(:));
[x1,x2,X]=find((qmi.*x));
[y1,y2,Y]=find((qmi.*y));
copx = sum(sum( img.*(qmi.*x) ))/ss_qmi; % centre of gravity
copy= sum(sum( img.*(qmi.*y) ))/ss_qmi;
R=mean(v);
vsnr=log10(abs(mean(elem)/std(elem)))*20; % distinguishability criteria
end

```

Surface Modeling Integration:

```

function [imdl,e1,n1]=mdl_stl(filename,elec);
% Script to find vertices and elements of a binary stl file generated
% from meshing software such as ICEM Ansys for surface meshed inverse model
% generation
% 29/5/2012 Ahmed Elsanadedy
% stlread function provided by Doron Harlev available through
% Matlab File Exchange

```

```

% elec: a matrix with [x,y,z] cartesian coordinates of point
%     electrode positions

%%%%%%%%%%%%%%%%%%%%%%%%%%%%%%%%%%%%%%%%%%%%%%%%%%%%%%%%%%%%%%%%%%%%%%%%% Acquire STL
Data%%%%%%%%%%%%%%%%%%%%%%%%%%%%%%%%%%%%%%%%%%%%%%%%%%%%%%%%%%%%%%%%%%%%%%%%%
[x,y,z,~]=stlread(filename);
% patch(x,y,z,v); % show mesh
% axis equal

%%%%%%%%%%%%%%%%%%%%%%%%%%%%%%%%%%%%%%%%%%%%%%%%%%%%%%%%%%%%%%%%%%%%%%%%% Process STL
Data%%%%%%%%%%%%%%%%%%%%%%%%%%%%%%%%%%%%%%%%%%%%%%%%%%%%%%%%%%%%%%%%%%%%%%%%%

% reshape and round to 4 significant figure
xx = round(reshape(x,[],1)*1000)/1000;
yy = round(reshape(y,[],1)*1000)/1000;
zz = round(reshape(z,[],1)*1000)/1000;
n=[xx,yy,zz]; % reshape input mesh data into eiders format

ind=0;
for i=1:(length(n)/3)
    for j=1:3
        ind=ind+1;
        e(i,j)=ind;
    end
end
e1=e;

% Translate to origin
mm=[mean(n(:,1)),mean(n(:,2))]; % ,mean(n(:,3))];
n(:,1)=n(:,1)-mm(1,1);
n(:,2)=n(:,2)-mm(1,2);
% n(:,3)=n(:,3)-mm(1,3);

% Scale to unit length
l=max(max(n));
n=n/l;

%%%%%%%%%%%%%%%%%%%%%%%%%%%%%%%%%%%%%%%%%%%%%%%%%%%%%%%%%%%%%%%%%%%%%%%%%
%% Create Connectivity Matrix
for t=1:length(e)
    for g=1:3
        q=e(t,g);
        nv=n(q,:);
    end
end

```

```

    [indx]=ismember(n,nv,'rows');%duplicate node values
    [rr,~,~]=find(indx);
    for jj=1:numel(rr)
        [r,c,~]=find(e==rr(jj));
        e1(r,c)=e(t,g);
    end
end
end

%Eliminate duplicate nodes
ns = sort(unique(reshape(e1,[],1)));
n1=n(ns,:);% create new node matrix without duplicates
for gg=1:length(ns)% renumber connectivity matrix to match node matrix
    nm=min(ns);
    e1(e1==nm)=gg;
    ns(ns==nm)=[];
end

%e1 element matrix
%n node matrix

% patch(n(:,1),n(:,2),n(:,3));
% axis equal
% hold on
% plot(x,y,'or')
% axis equal
% view(0,90)
%%%%%%%%%%%%%%%%%%%%%%%%%%%%%%%%%%%%%%%%%%%%%%%%%%%%%%%%%%%%%%%%%%%%%%%%
%%%%%%%%%%%%%%%%%%%%%%%%%%%%%%%%%%%%%%%%%%%%%%%%%%%%%%%%%%%%%%%%%%%%%%%%
%% Forward and Inverse model

%Electrode Selection
elec_n=distelecpts(elec,n1);%given electrode coordinates finds closest nodes

%Forward Model
fmdl1=fwd_model_from_v2(1,n1,[],e1,0.001,1);%create forward model

%Place electrodes in model
for h=1:length(elec_n)
    fmdl1.electrode(h).nodes=elec_n(h);
    %fmdl1.electrode(h).z_contact=0.001;
end

```

```

% Create inverse model
[stim,meas_sel] = mk_stim_patterns(16,1,[0,1],[0,1],{'no_meas_current'},1);
fmdl1.stimulation = stim;
fmdl1.meas_select = meas_sel;
fmdl1.system_mat='aa_calc_system_mat';
fmdl1.jacobian='aa_calc_jacobian';
fmdl1.solve='aa_fwd_solve';
imdl.name= 'Surface';
imdl.solve= 'aa_inv_solve';
imdl.hyperparameter.value = 1e-3;
imdl.RtR_prior= 'laplace_image_prior';
imdl.jacobian_bkgnd.value= 1;
imdl.reconst_type= 'difference';
imdl.fwd_model= fmdl1;
imdl= eidors_obj('inv_model', imdl);
imdl.fwd_model.normalize_measurements = 1;

% figure
%show_fem(fmdl1,[1,1,2])
end

function elec_n=distelec(elec,n)
% finds closest nodes for specified electrode Cartesian coordinates
% elec specified matrix [x,y,z]
% n is node matrix of mesh

for j=1:length(elec)
    for i=1:length(n)
        v=elec(j,:)-n(i,:);
        d(i)=norm(v);

    end
    % distance between points
    [~,nodI]=min(d);% find closest node index
    % elec_n{j}=n(nodI,:);
    elec_n(j)=nodI;
end
end

function FC= aa_system_mat_fields( fwd_model )
% AA_SYSTEM_MAT_FIELDS: fields (elem to nodes) fraction of system mat
% FC= aa_system_mat_fields( fwd_model )

```

```

% input:
% fwd_model = forward model
% output:
% FC:      s_mat= C' * S * conduct * C = FC' * conduct * FC;

% (C) 2008 Andy Adler. License: GPL version 2 or version 3
% $Id: aa_system_mat_fields.m 2408 2010-12-11 22:27:46Z aadler $

% 2012-5-20 Ahmed Elsanadedy integrated surface 3d linear interpolator
% to be used with EIT tactile sensor surface forward model
% lines 48-55

cache_obj = mk_cache_obj(fwd_model);
FC = eidders_obj('get-cache', cache_obj, 'aa_system_mat_fields');
if ~isempty(FC)
    eidders_msg('aa_system_mat_fields: using cached value', 4);
    return
end

FC= calc_system_mat_fields( fwd_model );

eidders_cache('boost_priority',1); % Moderate Priority boost
eidders_obj('set-cache', cache_obj, 'aa_system_mat_fields', FC);
eidders_msg('aa_system_mat_fields: setting cached value', 4);
eidders_cache('boost_priority',-1);

% only cache stuff which is really relevant here
function cache_obj = mk_cache_obj(fwd_model);
    cache_obj.elems    = fwd_model.elems;
    cache_obj.nodes    = fwd_model.nodes;
    try
        cache_obj.electrode = fwd_model.electrode; % if we have it
    end
    cache_obj.type      = 'fwd_model';
    cache_obj.name      = ''; % it has to have one

function FC= calc_system_mat_fields( fwd_model );
    p= aa_fwd_parameters( fwd_model );
    d0= p.n_dims+0;
    d1= p.n_dims+1;
    e= p.n_elem;
    n= p.n_node;
    nr=size(p.NODE,1);

    FFjidx= floor([0:d0*e-1]/d0)*d1*ones(1,d1) + ones(d0*e,1)*(1:d1);

```

```

FFiidx= [1:d0*e]*ones(1,d1);
FFdata= zeros(d0*e,d1);
dfact = (d0-1)*d0;
if nr~=d0 %surface mesh z coordinate for nodes
    for j=1:e
        nn=p.NODE(:,p.ELEM(:,j));
        l13=(nn(3,:)-nn(1,:));% vector 1
        l12=(nn(2,:)-nn(1,:));% vector 2
        c=dot(l13,l12)/(norm(l13)*norm(l12));% cos(theta)
        a=inv([1,zeros(1,2);1,norm(l12),0;1,norm(l13)*c,norm(l13)*...
            sqrt(1-c^2)]);
        %a= inv([ ones(d1,1), p.NODE( :, p.ELEM(:,j) )' ]);
        idx= d0*(j-1)+1 : d0*j;
        FFdata(idx,1:d1)= a(2:d1,:)/ sqrt(dfact*abs(det(a)));
    end %for j=1:ELEMs
else % 2d or 3d
    for j=1:e
        a= inv([ ones(d1,1), p.NODE( :, p.ELEM(:,j) )' ]);
        idx= d0*(j-1)+1 : d0*j;
        FFdata(idx,1:d1)= a(2:d1,:)/ sqrt(dfact*abs(det(a)));
    end
end
if 0 % Not complete electrode model
    FF= sparse(FFiidx,FFjidx,FFdata);
    CC= sparse((1:d1*e),p.ELEM(:,ones(d1*e,1), d1*e, n);
else
    [F2data,F2iidx,F2jidx, C2data,C2iidx,C2jidx] = ...
        compl_elec_mdl(fwd_model,p);
    FF= sparse([FFiidx(:); F2iidx(:)],...
        [FFjidx(:); F2jidx(:)],...
        [FFdata(:); F2data(:)]);

    CC= sparse([(1:d1*e)'; C2iidx(:)], ...
        [p.ELEM(:); C2jidx(:)], ...
        [ones(d1*e,1); C2data(:)]);
end

FC= FF*CC;

% Add parts for complete electrode model
function [FFdata,FFiidx,FFjidx, CCdata,CCiidx,CCjidx] = ...
    compl_elec_mdl(fwd_model,pp);
d0= pp.n_dims;
FFdata= zeros(0,d0);
FFd_block= sqrtm( ( ones(d0) + eye(d0) )/6/(d0-1) ); % 6 in 2D, 12 in 3D
FFiidx= zeros(0,d0);

```

```

FFjidx= zeros(0,d0);
FFi_block= ones(d0,1)*(1:d0);
CCdata= zeros(0,d0);
CCiidx= zeros(0,d0);
CCjidx= zeros(0,d0);

sidx= d0*pp.n_elem;
cidx= (d0+1)*pp.n_elem;
for i= 1:pp.n_elec
    eleci = fwd_model.electrode(i);
    zc= eleci.z_contact;
%   ffb = find_bdy_idx( bdy, fwd_model.electrode(i).nodes);
    [bdy_idx, bdy_area] = find_electrode_bdy( ...
        pp.boundary, fwd_model.nodes, eleci.nodes );

    for j= 1:length(bdy_idx);
        bdy_nds= pp.boundary(bdy_idx(j,:));

        FFdata= [FFdata; FFd_block * sqrt(bdy_area(j)/zc)];
        FFiidx= [FFiidx; FFi_block' + sidx];
        FFjidx= [FFjidx; FFi_block + cidx];

        CCiidx= [CCiidx; FFi_block(1:2,:) + cidx];
        CCjidx= [CCjidx; bdy_nds ; (pp.n_node+i)*ones(1,d0)];
        CCdata= [CCdata; [1;-1]*ones(1,d0)];
        sidx = sidx + d0;
        cidx = cidx + d0;
    end
end

end

function hh=show_fem( mdl, options)
% SHOW_FEM: show the EIDORS3D finite element model
% hh=show_fem( mdl, options )
% mdl is a EIDORS3D 'model' or 'image' structure
% hh= handle to the plotted model
%
% to change colours, try hh=show_fem(...); set(hh,'EdgeColor',[0,0,1]);

% (C) 2005-2011 Andy Adler. License: GPL version 2 or version 3
% $Id: show_fem.m 2718 2011-07-13 15:51:46Z aadler $
% line 251 modified ee to mdl.elems by Ahmed Elsanadedy

```

Bibliography

- [1] D. S. Holder, *Electrical Impedance Tomography Methods, History and Applications*. 2005, pp. 1-103.
- [2] A. Elsanadedy, Y. Mamatjan, M. Ahmadi, and A. Adler, "Characterisation of Conductive Polymer for EIT based Sensor," in *ASET ICECS*, 2012.
- [3] A. Adler and W. R. B. Lionheart, "Uses and abuses of EIDORS: an extensible software base for EIT," *Physiological measurement*, vol. 27, no. 5, p. S25, 2006.
- [4] R. S. Dahiya, G. Metta, M. Valle, and G. Sandini, "Tactile Sensing — From Humans to Humanoids," *IEEE Transactions on Robotics*, vol. 26, no. 1, pp. 1-20, 2010.
- [5] H. Yousef, M. Boukallel, and K. Althoefer, "Sensors and Actuators A : Physical Tactile sensing for dexterous in-hand manipulation in robotics — A review," *Sensors & Actuators: A. Physical*, vol. 167, no. 2, pp. 171-187, 2011.
- [6] S. Lang, "Review of some lesser-known applications of piezoelectric and pyroelectric polymers," *Applied Physics A: Materials Science and Processing*, vol. 134, no. A 85, pp. 125-134, 2006.
- [7] D. D. Rossi and F. Carpi, "Polymer based interfaces as bioinspired 'smart skins'," *Advances in colloid and interface*, vol. 116, pp. 165-178, 2005.
- [8] H. Aikawa, K. Shimomura, H. Kondo, A. Morishima, and A. Takanishi, "Development of a new humanoid robot WABIAN-2," *IEEE International Conference on Robotics and Automation, ICRA.*, no. May, pp. 76-81, 2006.
- [9] Y. Ogura et al., "Human-like walking with knee stretched, heel-contact and toe-off motion by a humanoid robot," in *IEEE/RSJ International Conference on Intelligent Robots and Systems*, 2006, pp. 3976-3981.
- [10] S. Lohmeier, T. Buschmann, and H. Ulbrich, "Humanoid robot LOLA," in *IEEE International Conference on Robotics and Automation*, 2009, pp. 775-780.
- [11] F. Pfeiffer and K. Loffler, "The concept of jogging johnnie," in *Robotics and Automation, IEEE*, 2002, no. May, pp. 3129- 3135.
- [12] S. Au, H. Herr, and J. Weber, "Powered ankle-foot prosthesis for the improvement of amputee ambulation," in *IEEE EMBS*, 2007, pp. 3020-3026.

- [13] R. D. Bellman, M. a. Holgate, and T. G. Sugar, "SPARKy 3: Design of an active robotic ankle prosthesis with two actuated degrees of freedom using regenerative kinetics," in *2nd IEEE RAS & EMBS International Conference on Biomedical Robotics and Biomechatronics*, 2008, pp. 511-516.
- [14] W. F. Plate, "A Small and Low-Cost 3-D Tactile Sensor for a," *IEEE Sensors Journal*, vol. 9, no. 9, pp. 1103-1110, 2009.
- [15] M. Ueda, K. Sekiguchi, H. Takemura, and H. Mizoguchi, "Plantar 3-axis distributed forces sensor based on measurement of silicone rubber deformation for walking analysis," *IEEE Sensors*, vol. 3, pp. 945-948, Oct. 2008.
- [16] Y. Huang, X. Ming, and T.-dimension Force, "Two Types of flexible tactile sensor arrays of robot for three-dimension force based on piezoresistive effects," in *IEEE International Conference on Robotics and Biomimetics*, 2009, pp. 1032-1037.
- [17] E. Hwang and J.-hoon Seo, "A polymer-based flexible tactile sensor for both normal and shear load detections and its application for robotics," *Microelectromechanical Systems, Journal of*, vol. 16, no. 3, pp. 556-563, 2007.
- [18] K. Shimoga, "Soft materials for robotic fingers," in *Robotics and Automation, IEEE*, 1992, no. May, pp. 4-9.
- [19] R. Katragadda, "A Novel Intelligent Textile Technology Based on Silicon Flexible Skins," *Sensors and Actuators A: Physical*, vol. 143, no. 1, pp. 1-4, 2008.
- [20] Y. Xu, Y. Tai, and A. Huang, "IC-Integrated Flexible Shear-Stress Sensor Skin," *Microelectromechanical Systems, Journal of*, vol. 12, no. 5, pp. 354-357, 2003.
- [21] K. Noda, Y. Hashimoto, Y. Tanaka, and I. Shimoyama, "MEMS ON ROBOT APPLICATIONS," in *Solid-State Sensors, Actuators and Microsystems Conference, IEEE*, 2009, pp. 2176-2181.
- [22] "The working principle of resistive tactile sensor cells," in *Mechatronics and Automation, 2005 IEEE*, 2005, no. July, pp. 471-476.
- [23] W. Thongruang, C. Ritthichaiwong, P. Bunnaul, P. Smithmaitrie, and K. Chetpattananondh, "Electrical and mechanical properties of ternary composites from natural rubber and conductive fillers," *Songklanakarin Journal of Science and Technology*, vol. 30, no. 3, pp. 361-366, 2008.
- [24] Y. Yang, M. Cheng, W. Chang, and L. Tsao, "An integrated flexible temperature and tactile sensing array using PI-copper films," *Sensors and Actuators A*, vol. 143, pp. 143-153, 2008.

- [25] M. Shimojo, A. Namiki, M. Ishikawa, R. Makino, and K. Mabuchi, "Rubber With Electrical-Wires Stitched Method," *IEEE Sensors*, vol. 4, no. 5, pp. 589-596, 2004.
- [26] F. Lorussi, W. Rocchia, and E. Scilingo, "Wearable, redundant fabric-based sensor arrays for reconstruction of body segment posture," *Sensors Journal, IEEE*, vol. 4, no. 6, pp. 807-818, 2004.
- [27] D. De Rossi, F. Carpi, F. Lorussi, A. Mazzoldi, E. P. Scilingo, and A. Tognetti, "Electroactive fabrics for distributed, conformable and interactive systems," in *Proceedings of IEEE Sensors*, 2002, vol. 2, pp. 1608-1613.
- [28] E. Pritchard, M. Mahfouz, B. Evans, and S. Eliza, "Flexible capacitive sensors for high resolution pressure measurement," in *IEEE Sensors*, 2008, pp. 1484-1487.
- [29] G. Cannata, M. Maggiali, and G. Metta, "An embedded artificial skin for humanoid robots," in *IEEE International Conference on Multisensor Fusion and Integration for Intelligent Systems*, 2008, pp. 2-6.
- [30] Y. Hasegawa, M. Shikida, and D. Ogura, "Fabrication of a wearable fabric tactile sensor produced by artificial hollow fiber," *Journal of Micromechanics and Microengineering*, vol. 085014, no. 18, 2008.
- [31] R. Dahiya, M. Valle, and G. Metta, "Tactile sensing arrays for humanoid robots," in *Research in Microelectronics and Electronics, IEEE*, 2007, pp. 201-204.
- [32] J. Heo and J. Kim, "Tactile Sensors using the Distributed Optical Fiber Sensors," in *Sensing Technology, ICST*, 2008, pp. 486-490.
- [33] Y. Ohmura and Y. Kuniyoshi, "Conformable and scalable tactile sensor skin for curved surfaces," in *IEEE Robotics and Automation*, 2006, no. May, pp. 1348-1353.
- [34] L. Ascari, P. Corradi, and L. Beccai, "A miniaturized and flexible optoelectronic sensing system for tactile skin," *Journal of Micromechanics and Microengineering*, vol. 17, no. 11, pp. 1-22, 2007.
- [35] O. Kerpa, K. Weiss, H. Wörn, and D.- Karlsruhe, "Development of a Flexible Tactile Sensor System for a Humanoid Robot," in *IEEE International Conference on Intelligent Robots and Systems*, 2003, no. October, pp. 1-6.
- [36] A. Ni, X. Dong, G. Yang, and F. Fu, "Using a priori information to improve on localization of conductivity changes in brain in electrical impedance tomography," *World Congress on Medical Physics*, vol. 14, no. 1, pp. 3960-3963, 2007.

- [37] T. F. Schuessler and J. H. Bates, "Current patterns and electrode types for single-source electrical impedance tomography of the thorax.," *Annals of biomedical engineering*, vol. 26, no. 2, pp. 253-9, 1998.
- [38] M. Pessel, "Multiscale electrical impedance tomography," *Journal of Geophysical Research*, vol. 108, no. B1, pp. 1-12, 2003.
- [39] P. Nick and W. R. B. Lionheart, "A Matlab toolkit for three-dimensional electrical impedance tomography: a contribution to the Electrical Impedance and Diffuse Optical Reconstruction Software project," *Measurement science and*, vol. 1871, no. 13, pp. 1871-1883, 2002.
- [40] A. Plaskowski, R. M.S. Beck, and T. Dyakowski, *Imaging Industrial Flows*. 1995.
- [41] T. York, "Status of electrical tomography in industrial applications," *Journal of Electronic Imaging*, vol. 10, no. 3, p. 608, 2001.
- [42] R. Knight and R.T.Kipezynski, "The Use of EIT Techniques to Measure Interface Pressure," in *International Conference of the IEEE*, 1990, vol. 1, no. 5, pp. 2307-2308.
- [43] "Distributed Pressure Measurement using Electrical Impedance Tomography: Initial Results," in *IET*, 1996, pp. 1-5.
- [44] M. J. Booth and I.Basarab-Horwath, "A Comparison of Three Electrode Configurations for Electrical Impedance Tomography," in *IET*, 1995, pp. 1-3.
- [45] W. S. Fulton and R. T. Lipczynski, "BODY-SUPPORT PRESSURE MEASUREMENT USING ELECTRICAL IMPEDANCE TOMOGRAPHY," in *Engineering in Medicine and Biology Society, IEEE*, 1993, pp. 98-99.
- [46] H. Alirezaei, A. Nagakubo, and Y. Kuniyoshi, "A highly stretchable tactile distribution sensor for smooth surfaced humanoids," in *7th IEEE-RAS International Conference on Humanoid Robots*, 2007, pp. 167-173.
- [47] A. Nagakubo and H. Alirezaei, "A deformable and deformation sensitive tactile distribution sensor," in *Robotics and Biomimetics, IEEE*, 2007, pp. 1301-1308.
- [48] D. S. Tawil, S. Member, D. Rye, and M. Velonaki, "Improved Image Reconstruction for an EIT-Based Sensitive Skin With Multiple Internal Electrodes," *IEEE Transactions on Robotics*, vol. 27, no. 3, pp. 425-435, 2011.
- [49] C. M., I. D., N. JC., S. S., and G. JC., "NOSER: an algorithm for solving the inverse conductivity problem," *International Journal on Imaging System Technology*, vol. 2, pp. 66-75, 1991.

- [50] H. Gagnon, M. Cousineau, and A. Adler, "A resistive mesh phantom for assessing the performance of EIT systems," *IEEE Transactions on Biomedical Engineering*, vol. 57, no. 9, pp. 2257-2266, 2010.
- [51] D. S. Tawil and D. Rye, "Touch modality interpretation for an EIT-based sensitive skin," in *International Conference on Robotics and Automation ,IEEE*, 2011, pp. 3770-3776.
- [52] P. Silvester and R. Ferrari, *Finite Elements for Electrical Engineers, 3rd ed Cambridge University Press*. 1996.
- [53] B. M. Graham, "Enhancements in Electrical Impedance Tomography (EIT) Image Reconstruction for 3D Lung Imaging," Carleton University, 2007.
- [54] T. Murai and Y. Kagawa, "Electrical Impedance computed tomography based on finite element model," *IEEE Transactions on Biomedical Engineering*, vol. 32, pp. 177-184, 1985.
- [55] A. J. S. Boyle, "The Effect of Boundary Shape Deformation on Two-Dimensional Electrical Impedance Tomography," Carleton University, 2010.
- [56] B. M. Graham and a Adler, "Objective selection of hyperparameter for EIT," *Physiological Measurement*, vol. 27, no. 5, p. S65-S79, May 2006.
- [57] A. Adler et al., "GREIT: a unified approach to 2D linear EIT reconstruction of lung images," *Physiological Measurement*, vol. 30, no. 6, p. S35-S55, Jun. 2009.
- [58] L. WRB, "Developments in EIT reconstruction algorithms: pitfalls, challenges and recent developments," *Journal of Physiological Measurment*, vol. 25, pp. 125-142, 2004.
- [59] Y. Maimaitijiang and P. Gaggero, "Evaluation of EIT System Performance," *Physiological Measurement*, vol. 32, no. 7, p. 851, 2011.